Summer 7-2019

Electropolymerization and Characterization of Thin Film Dielectrics

Christopher White II
University of Nebraska - Lincoln, christopher.white-ii@huskers.unl.edu

ELECTROPOLYMERIZATION AND CHARACTERIZATION OF THIN FILM DIELECTRICS

by

Christopher Joseph White II

A THESIS

Presented to the Faculty of

The Graduate College at the University of Nebraska

In Partial Fulfillment of Requirements

For the Degree of Master of Science

Major: Chemistry

Under the Supervision of Professor Jody Redepenning

Lincoln, Nebraska

July, 2019

ELECTROPOLYMERIZATION AND CHARACTERIZATION OF THIN FILM DIELECTRICS

Christopher J. White II, M. S.

University of Nebraska, 2019

Advisor: Jody G. Redepenning

Graphene is a two-dimensional allotrope of carbon, with several superlative properties, including high electron and hole conductivities, high tensile strength, and chemical robustness. Its chemical and physical properties make it attractive for in use in a myriad of applications, including transistors. However, graphene's chemical inertness and its physical and electrical properties' dependency on its conjugated structure make building composite materials with graphene difficult. In 2015, Lipatov, et. al. demonstrated that a film derived from electropolymerized phenol could be used as a dielectric layer on transistor devices fabricated from exfoliated graphene. This thesis extends that research, by detailing experiments of phenol and phenol derivative electropolymerization. Several derivatives, such as 4-vinylphenol, 4-chlorophenol, and phloroglucinol, solution conditions, and electropolymerization conditions were investigated. Most derivatives were found to be more porous than the phenol film, as determined by pinhole measurements using electroactive compounds. Interestingly, electropolymerizing phloroglucinol in potassium chloride solution resulted in a cation exchange film. Phloroglucinol films of various thicknesses were successfully electropolymerized onto devices fabricated from exfoliated, then chemical vapor deposited, graphene. Aluminum oxide atomic layer deposition was then performed successfully, followed by metal or PEDOT:PSS top gates. Unfortunately, all top-gated devices had high leakage currents and were not gateable. A brief investigation into the cause of the high leakage currents was inconclusive.

Lipatov, A., Wymore, B. B., Fursina, A., Vo, T. H., Sinitskii, A., Redepenning, J. G. *Chem. Mater.* **2015** *2*7 157

The author wants to thank Dr. Jody Redepenning and Dr. Sinitskii for their guidance in completing this project. The author wants to thank Dr. Rebecca Lai for being on the author's committee.

The author also wants to thank Dr. Benjamin Wymore, Dr. Alexey Lipatov, David Deibert, and Ufuk Kilic for their help and contribution.

Lastly, the author wants to thank Minrong Jiang (江玟容) for her support while pursuing this degree.

Table of Contents

List of Figures

List of Tables

CHAPTER 1: INTRODUCTION

Two-dimensional materials were initially though impossible, due to their perceived thermodynamic instability[6, 7], though such materials were of considerable theoretical interest. Even graphene, in the form of graphite, originally received theoretical treatment.[8] Graphene was first derived via mechanical exfoliation from graphite in 2004.[9] Since then, an explosion of research into it, and other two dimensional materials, happened. A cursory search of "graphene review" yields over 1.42 million results. Its chemistry and physics are rich. A detailed review of graphene's chemistry and physics will not be discussed, but can be found by reading the bibliographies of the papers contained within this thesis, as well as references 1, 2, 3, 4, and 5. Instead, this thesis will highlight some basic chemical and electronic properties of graphene and synthesis chemistry of graphene. Then, this thesis will discuss the uses of graphene, particularly using graphene in transistors. Finally, this thesis will discuss the motivation of the research contained within it.

Basic Chemical and Electronic Properties of Graphene

Graphene's structure is a two-dimensional hexagonal lattice, often described analogously as chicken wire fence. The carbon atoms in pristine graphene are all sp^2-hybridized. The remaining p_z orbital is delocalized across the sheet in an extensive π conjugated system. These delocalized π electrons are responsible for most of the amazing electronic properties of graphene, while the sp^2-hybridized bonds are responsible for most of the amazing mechanical properties of graphene.

Graphene is a zero-band gap material, meaning the energy between its highest occupied molecular orbital (HOMO) and its lowest unoccupied molecular orbital (LUMO) is zero at room temperature. Few two-dimensional materials have this property. For comparison, metals have overlapping HOMO and LUMO levels, while insulators have large

HOMO and LUMO gaps. If the energy gap between the HOMO and LUMO is a few electron volts, the material is a semiconductor. (For example, silicon, which is widely used in electronics, has a band gap of 1.12 eV.[10]) The conjugated π orbitals allow charge carriers to travel ballistically; in fact, the charge carriers travel as if they are massless.[9] This property can be useful for electronic devices, because charges can be sent quickly, allowing for fast switching. However, the zero bandgap in graphene may not be useful for other electronic devices, such as transistors. Band gaps in graphene can be introduced by applying a voltage bias.[9, 10, 12, 13]

Fabrication Techniques of Graphene

Graphene was first isolated from graphite by mechanical exfoliation[9, 10], although scientists have studied graphene theoretically since the 1960s.[12] Since then, various methods for synthesizing it have been developed. These include both top-down, such as sonication and mechanical exfoliation, and bottom-up, such as chemical vapor deposition and decomposition of SiC, approaches. Of all the approaches, mechanical exfoliation of highly oriented pyrolytic graphene provides the best quality of graphene, as measured by number of defects.[1] This technique is usually referred to as the "Scotch tape method," because it involves pressing flakes of graphite from Scotch tape onto substrates. The adhesion forces between the substrate and graphite eventually cleave graphene from the graphite. This method is useful for producing graphene for the study of its properties; however, this method is tedious and inefficient. Most cleavage of graphite results in multi-layer graphite.

Currently, the most popular method of producing graphene is chemical vapor deposition (CVD).[14] This technique is now quite well established.[12, 13, 14] A source of carbon, typically methane, is flowed into a furnace around 1000 ^{o}C or higher. Inside the furnace is a metal foil or sheet, commonly copper. Over time, graphene then deposits onto the surface

of the metal foil through a complex set of chemical reactions that depends on the pressure of methane, the pressure of hydrogen and other gasses, the temperature of the furnace, and the metal foil or sheet.[15, 16, 17] The main mechanism of CVD growth is the dissolution and "precipitation" of carbon into and out of the metal foil. Metals in which carbon is highly soluble, such as nickel, tend to produce multi-layer graphite. Conversely, metals in which carbon is not highly soluble, such as copper, tend to produce graphene.

The pressure of methane controls the rate of deposition of carbon. Too low a pressure and deposition will not start. Too high, and multi-layer graphite will grow on the surface of the metal foil. Hydrogen maintains a reducing environment, where as other gasses, such as argon, help maintain pressure within the furnace.[18]

The lattice structure of the metal must also be compatible. Graphene has a closely packed hexagonal structure; mismatch between the metal's and graphene's crystal lattice will result in graphene with many defects (i.e., missing atoms, irregular pentagonal, hexagonal, and heptagonal formation, etc.). Monocrystal formation is important for obtaining the superlative properties of graphene. Grain boundaries between graphene crystals occur whenever two graphene crystals of different orientation encounter one another.[18] This can be prevented by either controlling the nucleation and crystal growth of graphene, and by matching the metal's and graphene's crystal lattices.

Building a Graphene Transistor

Graphene's innate stability protects graphene from degradation and chemical alteration. This can be a problem for fabricating heterostructures. As mentioned earlier, graphene is a zero-band gap material. Voltage biasing and chemical modification are two ways one can introduce a band gap.[12, 21]

Voltage biasing is achieved through the fabrication of a transistor.[19] In a transistor, a conductive material is connected to two electrodes, called a source and drain. The source electrode is from where charge carriers enter the conductive material: the drain electrode is from where charge carriers exit the conductive material. On top of the conductive material is a third electrode: the top gate. An isolating dielectric material separates the top gate from the conductive material. Application of a voltage at the top gate controls the current through the conductive material.

Unfortunately, it is difficult to deposit an insulating dielectric layer to graphene, because of graphene's lack of surface "dangling bonds" and general inertness. Atomic layer deposition (ALD), which is commonly used in electronics to deposit an insulating dielectric layer, is nearly impossible on defect-free graphene.[20] Thus, modification of graphene is necessary.

Chemical modification of graphene influences the band structure and introduces defects by distorting graphene's conjugated π system. These defects hinder the ballistic travel of charge carriers, degrading the charge mobility. Because of graphene's extensive π orbital conjugation, $\pi - \pi$ interactions and van der Waals forces are the only viable intermolecular forces that graphene has for noncovalent interaction.

Research into noncovalent functionalization of graphene is extensive.[22] Many of the techniques involve small molecules self-assembling onto the surface of graphene.[22, 23] Others saturate the surface of graphene with gasses, and then react those gasses with metal oxide precursors.[24, 25, 26] Finally, polymers can be grown either *in situ* or layered onto graphene.

Good candidate for such polymers are those with structures similar to graphene. One can imagine derivatives of benzene known to form polymers, such as phenol, styrene, and aniline. Polymerization of these monomers typically occur in a homogeneous solution.

If graphene were added to these solutions, it would inevitably become encapsulated in the polymer matrix, which may not be useful for electronic devices. Thus, a more useful approach is heterogeneous polymerization. Recall the structure of a transistor with a conductive material like graphene. If the polymer could be formed directly on the surface of the graphene, that polymer could not only serve as the dielectric, but also as a seed or adhesion layer for further steps, such as metal oxide ALD. A convenient method of forming this polymer is to electropolymerize it.

Polymers with phenyl groups present noncovalently interact with graphene. In addition, electropolymerization of phenol[27, 28, 29], styrene[30], and aniline[31, 32] are known to occur at an electrode. Electropolymerization has the advantage that deposition occurs only at exposed electrically conductive surfaces, such as graphene. In addition, electropolymerization of certain compounds, such as phenol, is self-limiting. It was shown in 2015 by Redepenning, Sinitskii, and others[33] and Vereecken and others[34] that electropolymerization of phenol can be used as an insulating dielectric for graphene transistors.

This thesis discusses my work expanding the research of electropolymerizing phenol derivatives for noncovalently depositing an insulating dielectric onto the surface of graphene. In Chapter 2, I will discuss the plethora of molecules and conditions I used. All derivatives and conditions produced insulating polymer films. A polymer film derived from phloroglucinol exhibited cation-exchange properties. In Chapter 3, I will fabricated transistor devices out of CVD graphene. I then show the successful electropolymerization of phloroglucinol onto these devices, followed by successful aluminum oxide ALD. However, these devices exhibit high leakage current between the top gate and drain electrodes. After a brief investigate, I inconclusively determine the cause of the high leakage

currents. I speculate either inherent pinholes and/or changes in the polymer during heating are responsible.

CHAPTER 2: ELECTROPOLYMERIZATION OF PHENOL DERIVATIVES

Gileadi, et. al.[46] investigated phenol's electrochemistry in 1970. They observed the oxidation of phenol was irreversible, and the resulting polymer film passivated their platinum electrode against the oxidation of bromide and other compounds. Then, in 1993, Barlett, et. al.[28] proposed a mechanism for the oxidative electropolymerization of phenol, which is reproduced in Figure 2.1. In the first step, phenol is deprotonated. Next, the phenolate ion is oxidized at the electrode's surface. Because of the benzene substructure, the lone electron can move into the 2, 4, and 6 position, as well as remain on the oxygen, which is its preferred location. Phenol radicals can react with phenol molecules through head-to-tail coupling. After rearrangement, chained radical reactions, and oxidation at the electrode, poly(phenylene oxide) is formed, and adhered to the electrode's surface.

I used cyclic voltammetry to screen nineteen phenol derivatives and usually five conditions for their abilities to a) passivate an electrode during electropolymerization, and b) block a series of electroactive species after electropolymerization, namely hexamineruthenium (III), ferrocyanide, and ferrocene. Cyclic voltammetry allowed me to actively monitor the passivation of the electrode during and after electropolymerization. Another test was whether the passivation cyclic voltammogram for each of the phenol derivatives was improved over that of phenol as judged by the magnitude of the current. Most of the phenol derivatives were chosen because prior literature suggested they could form polymers in solution at other electrodes.

Experimental

4-Chlorophenol, 4-fluorophenol, 1-naphthol, 8-hydroxyquinoline, tris(8-hydroxyquinoline) aluminum, 2,6-diphenylphenol, furfural, pyrogallol, 4-vinylaniline, salicylic acid, 4-vinylphenol, benzyl alcohol, 4-cyanophenol, benzonitrile, 3-nitrophenol,

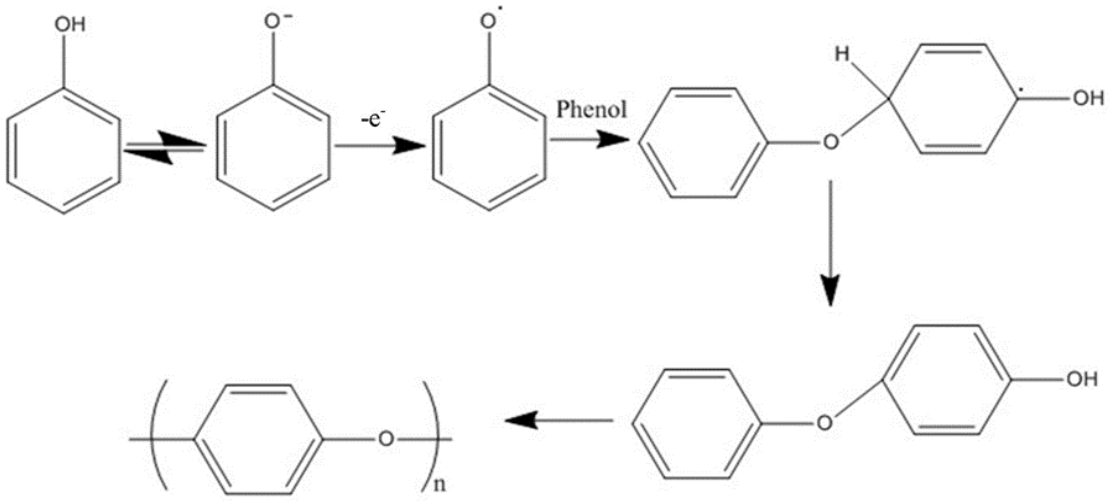

Figure 2.1: A mechanism for electropolymerization of phenol. It is assumed that all derivatives of phenol follow a similar mechanism. Of course, due to resonance, the phenol can electropolymerize in other ways. Adapted from Barlett, P. N.; Cooper, J. M. J. Electroanal. Chem. 362 (1993) 1-12.

4-nitrophenol, 2-aminophenol, and phloroglucinol were used as received without further purification.

Solutions included preparations of 0.05 M of each phenol derivative in 1 M potassium chloride (KCl), 0.5 M sulfuric acid (H_2SO_4), 0.1 M sodium hydroxide (NaOH), 0.1 M tetrabutylammonium hexafluorophosphate ($TBAPF_6$) in acetonitrile (ACN), and 0.05 M tetramethylammonium hydroxide (TMAOH) and 0.1 M $TBAPF_6$ in ACN, among others. Table 2.2, located at the end of the chapter, lists all the various solutions prepared for each chemical. The water used was at least 17 MΩ·cm.

Pinhole measurements were performed in solutions of 0.005 M hexaminеruthenium (III) chloride ($Ru(NH_3)_6^{3+/2+}$) in 1 M KCl, 0.005 M potassium ferrocyanide tetrahydrate ($Fe(CN)_6^{4-/3-}$) in 1 M KCl, and 0.005 M ferrocene ($Fc^{0/+}$) with 0.1 M $TBAPF_6$ in ACN. All solids were used as received without further purification. The general parameters for each experiment are given in Table 2.1. The measurements were performed on a CH Instrument Electrochemical Workstation 760C with CHI software. The working electrodes used were 2 mm gold (Au) electrode in polyether ether ketone (PEEK), 2 mm platinum (Pt) electrode in PEEK, 3 mm glassy carbon (GC) electrode in PEEK, and 1.5 mm GC in PEEK. The electrodes were polished in a 0.3 μm aluminum oxide slurry before any experiment to remove any residue, and then rinsed in water and dried with a lint-free tissue. The reference electrode was usually a homemade silver/silver chloride (Ag/AgCl) reference electrode prepared according to reference 35. Use of other reference electrodes are indicated in the results and figures.

Typical electropolymerization experiments involved the following steps:

1. Obtain cyclic voltammograms of $Ru(NH_3)_6^{3+/2+}$, $Fe(CN)_6^{4-/3-}$, and $Fc^{0/+}$ at a polished electrode.

2. Oxidize the monomer in a solution for a predetermined number of cycles (usually 90). The initial and most negative potentials (or, in the case reductive electropolymerization, most positive potential) were always the solution's open circuit potential[1]. The most positive potential was determined experimentally, and was chosen where the anodic (or, in some cases, cathodic) peak was at least 100 mV before the switching potential.
3. Check for pinholes by obtaining cyclic voltammograms of $Ru(NH_3)_6^{3+/2+}$, $Fe(CN)_6^{4-/3-}$, and $Fc^{0/+}$ after electropolymerization.

Table 2.1: Electrochemical Conditions for Pinhole Measurements			
	$Ru(NH_3)_6^{3+/2+}$	$Fe(CN)_6^{4-/3-}$	$Fc^{0/+}$
Initial Potential	0.0 V	0.0 V	0.0 V
High Potential	0.0 V	0.6 V	0.6 V
Low Potential	-0.35 V	0.0 V	0.0 V
Initial Polarity	Negative	Positive	Positive
Scan Rate	0.100 V/s	0.100 V/s	0.100 V/s
Sweep Segments	2	2	2
Sample Interval	0.001	0.001	0.001
Quiet Time	10 s	10 s	10 s

Results

Phenol

As an example, the oxidation of 50 mM phenol in 0.5 M Na_2SO_4, pH 2.0 is given in Figure 2.2. Phenol oxidation is irreversible, passivating the surface of the gold electrode with a thin film. The current of the second oxidation cycle of phenol is drastically lower than the first. Hence, the phenol film produced after the first cycle blocks continued oxidation of phenol. As can also be seen, subsequent cycles of oxidation yield less and less absolute current, indicating less oxidation of phenol. Furthermore, this implies the electropolymerization of phenol is self-limiting.

[1] In a number of cyclic voltammograms shown, the initial and most negative potential was assumed to be zero, partly because the open circuit potential was frequently close to zero relative to the reference electrode

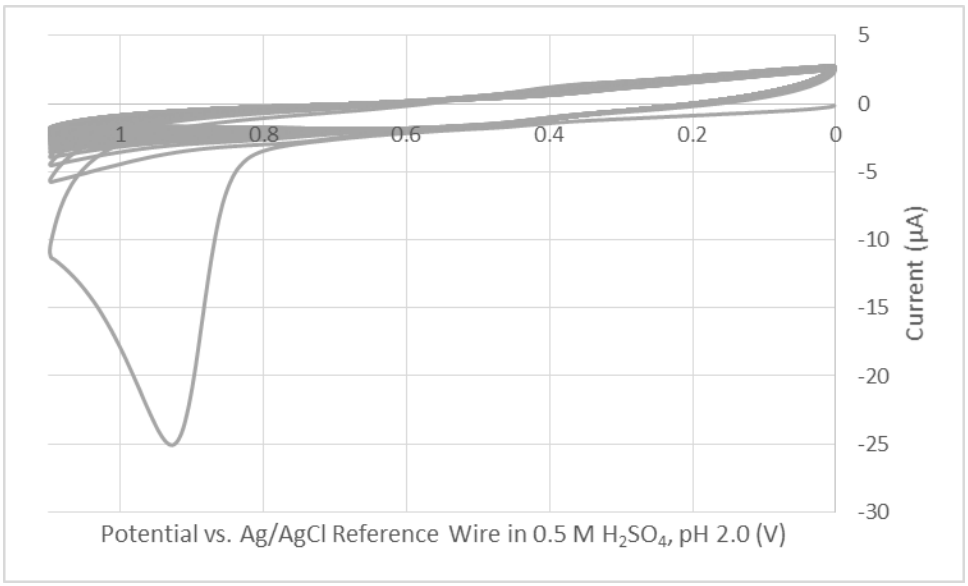

Figure 2.2: Cyclic voltammogram of phenol in 0.5 M H_2SO_4 solution adjusted to pH 2.0. Note how the subsequent cycles have smaller anodic peak current due to passivation of the electrode surface by phenol electropolymerization. The electropolymerization was performed for 180 cycles.

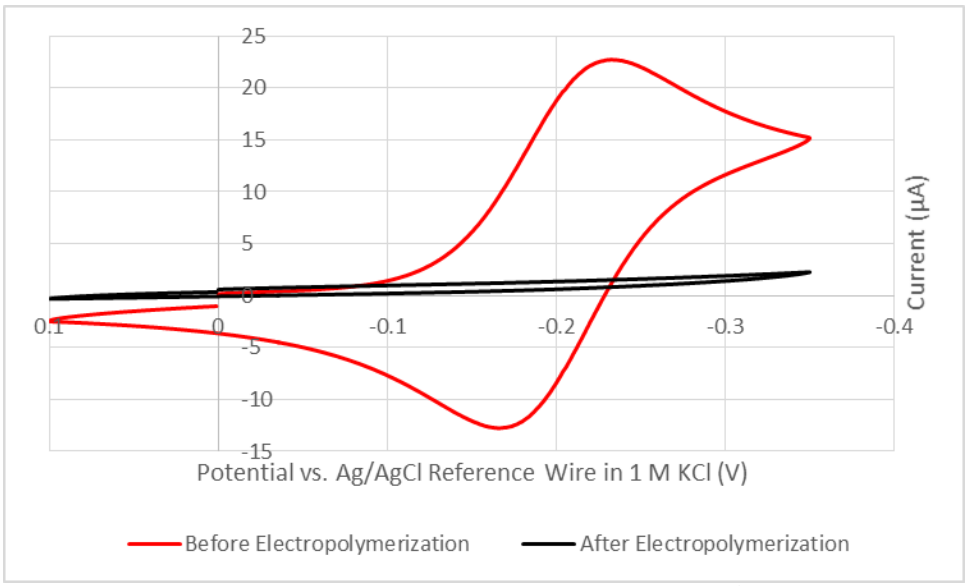

Figure 2.3: Overlay of cyclic voltammogram of $Ru(NH_3)_6^{3+/2+}$ at a 1.5 mm glassy carbon electrode after electropolymerization. The cyclic voltammogram suggests complete coverage of the electrode by the electropolymerized phenol.

Before and after the electropolymerization, I obtained cyclic voltammograms of $Ru(NH_3)_6^{3+/2+}$, shown in Figure 2.3 Before electropolymerization, $Ru(NH_3)_6^{3+/2+}$ shows reversible reduction and oxidation. After electropolymerization, only nonfaradaic current is visible. The film completely passivates the electrode, preventing $Ru(NH_3)_6^{3+/2+}$ reduction. Furthermore, this showed the film is free of pinholes.

Based on the mechanism in Figure 2.1, the pH should affect the electropolymerization. In fact, in experiments not shown here, the oxidation peak shifts negative with increasing pH.

4-Chlorophenol

Figure 2.4 illustrates the cyclic voltammogram of the electropolymerization of 4-chlorophenol in 0.5 M Na_2SO_4, pH 2.0. The oxidation of 4-chlorophenol is irreversible, like phenol. The specific mechanism of 4-chlorophenol electropolymerization was not investigated nor will be discussed in this thesis. Rather, the resulting film's behavior will be presented.

Figure 2.5 illustrates the cyclic voltammogram of $Ru(NH_3)_6^{3+/2+}$ before and after electropolymerization of 4-chlorophenol in 0.5 M Na_2SO_4, pH 2.0. Before electropolymerization, the cathodic and anodic peaks are clearly visible. After electropolymerization, the cathodic and anodic peaks are no longer visible.

The passivation of the electrode can be controlled by varying the conditions of electropolymerization. Figure 2.6 illustrates this. Three different electropolymerization conditions passivate the electrode towards $Ru(NH_3)_6^{3+/2+}$ differently. Table 2.2 contained the three conditions. More cycles increase the passivation of the electrode. In addition, the switching potential used in the electropolymerization influences the passivation of the electrode. More positive potentials can cause more phenol molecules to oxidize. However,

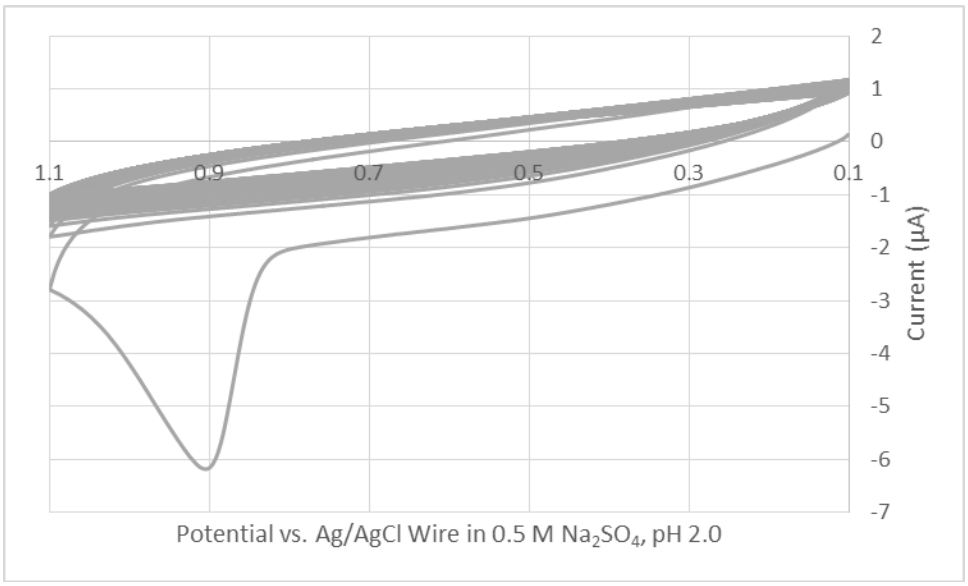

Figure 2.4: Cyclic voltammogram of 5mM 4-chlorophenol in 0.5 M Na_2SO_4, adjusted to pH 2.0. Like the phenol cyclic voltammogram, subsequent cycles have smaller peak anodic currents. The cyclic voltammogram shows all 200 cycles.

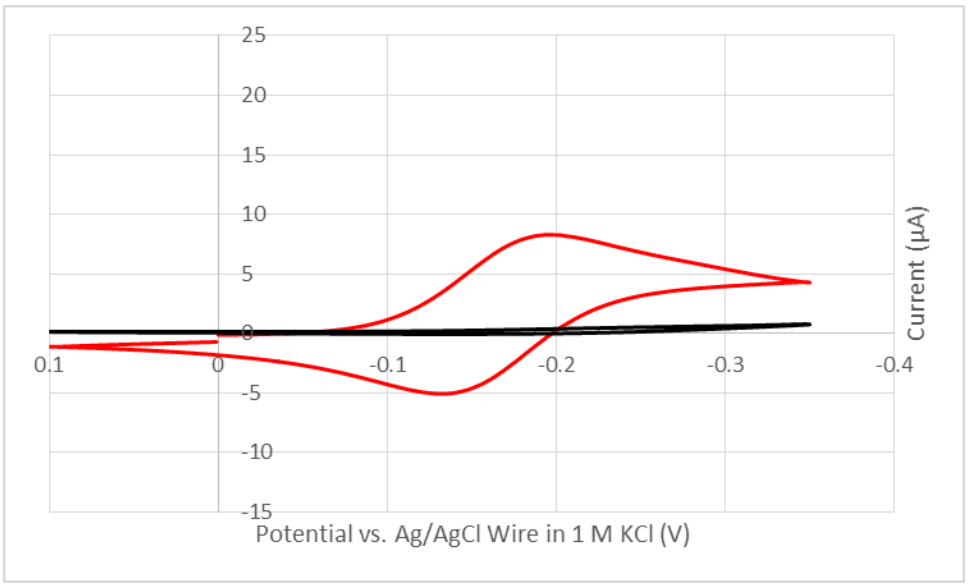

Figure 2.5: Cyclic voltammogram of $Ru(NH_3)_6^{3+/2+}$ before and after electropolymerization of .5 mM 4-chlorophenol in 0.5 M Na_2SO_4, pH 2.0.

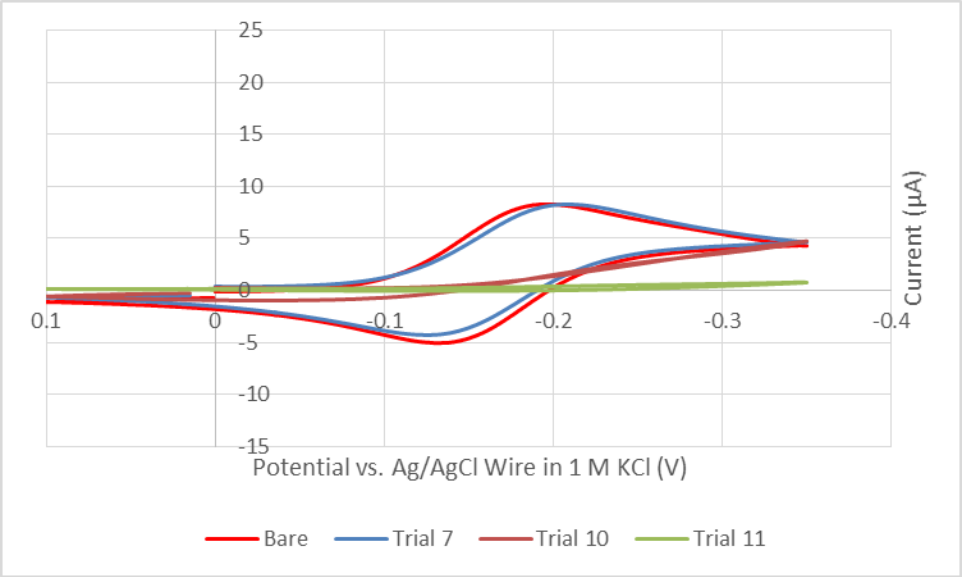

Figure 2.6: Cyclic voltammograms of $Ru(NH_3)_6^{3+/2+}$ under different conditions of electropolymerization. For comparison, the cyclic voltammogram of $Ru(NH_3)_6^{3+/2+}$ at a bare glassy carbon electrode is shown

a limit does exist, as the polymer can break down at very positive potentials. Figure 2.7 illustrates an electropolymerization cyclic voltammogram of 4-chlorophenol in 1 M NaOH. After the first cycle, the electrode is passivated, like in the acidic solution. However, note the location of the peak potential. In basic solutions, phenols tend to oxidize at low positive potentials. Recall the scheme in Figure 2.1. The first step of phenol oxidation is the deprotonation of the phenol. In basic solution, phenol oxidation kinetically faster. Pinhole measurements with $Ru(NH_3)_6^{3+/2+}$ are shown in Figure 2.8. Compared to the cyclic voltammogram of $Ru(NH_3)_6^{3+/2+}$ after electropolymerization of 4-chlorophenol in acid, this cyclic voltammogram has a high magnitude of current, indicating a film that is more porous. While high pH solutions make oxidation of 4-chlorophenol easier than that in low pH solutions, the films produced may have worse quality.

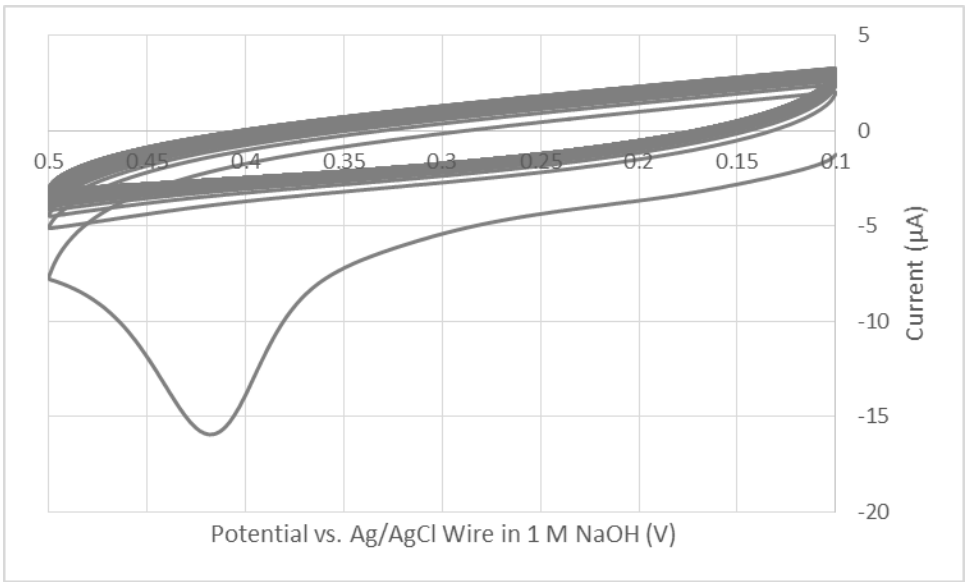

Figure 2.7: Cyclic voltammogram of 0.1 M 4-chlorophenol in 1 M NaOH. The cyclic voltammogram shows all 50 cycles.

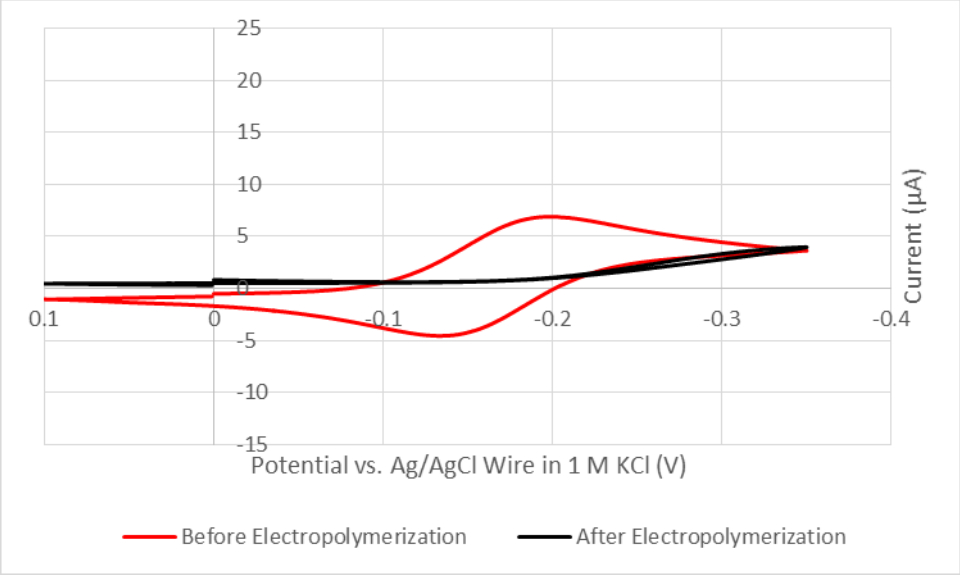

Figure 2.8: Cyclic voltammogram of $Ru(NH_3)_6^{3+/2+}$ before and after electropolymerization of 0.1 M 4-chlorophenol in 1 M NaOH.

1-Naphthol

Figure 2.9 illustrates the electropolymerization cyclic voltammogram of 10 mM 1-naphthol in 0.1 M NaOH at a glassy carbon electrode. The mechanism for 1-naphthol oxidation and subsequent polymerization is complex: the reader is referred to Reference 9 for more detail. The average anodic peak was determined to be 0.246 ± 0.058 V vs. Ag/AgCl reference electrode. As expected, electropolymerizaion of 1-naphthol passivates the glassy carbon electrode. However, the passivation, as measured via pinhole measurements with $Ru(NH_3)_6^{3+/2+}$, is not better than that with phenol.

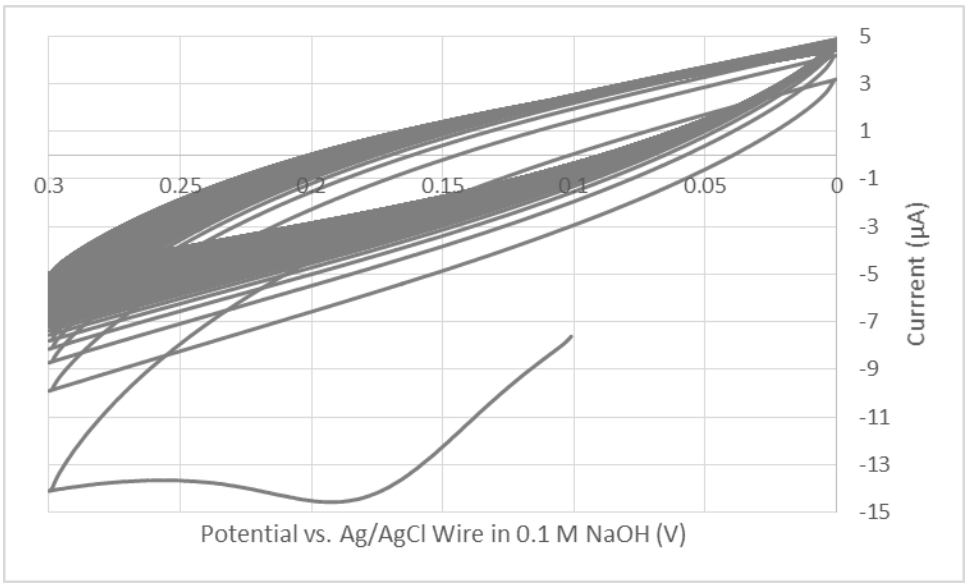

Figure 2.9: Cyclic voltammogram of 10 mM 1-naphthol in 0.1 M NaOH. The cyclic voltammogram shows all 200 cycles.

8-Hydroxyquinoline

The electropolymerization of 8-hydroxyquinoline was repeated using a higher concentration of 8-hydroxyquinoline than described in Reference 45. The solution was prepared by dissolving 0.0105 g 8-hydroxyquinoline into a solution prepared by mixing 2 mL 2 mM 8-hydroxyquinoline in 50 v/v % ethanol with 8 mL 0.1 M NaCl. The resulting concentration, neglecting volume change, is 3.79 mM. The added 8-hydroxyquinoline did not dissolve completely; thus, the resulting concentration is less than that recorded. The electropolymerization cyclic voltammogram of this solution is found in Figure 2.10. It has a broad oxidation peak, which is almost indistinguishable from the background current.

The sharp oxidation peak at about 0.1 V vs. Ag/AgCl wire is likely due to some impurity at the surface of the electrode. The film passivated the electrode towards both 8-hydroxyquinoline and $Ru(NH_3)_6^{3+/2+}$. A small broad reductive peak is visible in the $Ru(NH_3)_6^{3+/2+}$ cyclic voltammogram after electropolymerization, which can be seen in Figure 2.11.

8-Hydroxyquinoline is soluble low pH solutions. Hence, I expected the electropolymerized polymer to be as well. After just 10 minutes of soaking in 0.1 M HCl, the electrode showed no passivation towards $Ru(NH_3)_6^{3+/2+}$, as shown in Figure 2.12, suggesting dissolution of the polymer film.

A 1 mM aluminum tris(8-hydroxyquinoline) with 0.1 M tetrabutylammonium hexafluorophosphate in acetonitrile solution was electropolymerized onto a glassy carbon electrode. The electropolymerization cyclic voltammogram is shown in Figure 2.13. Two oxidation peaks are prominent: one at 1.112 V and another at 1.403 V vs. Ag/AgCl reference wire. A yellow film was visible on the surface of the electrode after electropolymerization. The yellow film was not visible after soaking in 0.1 M HCl.

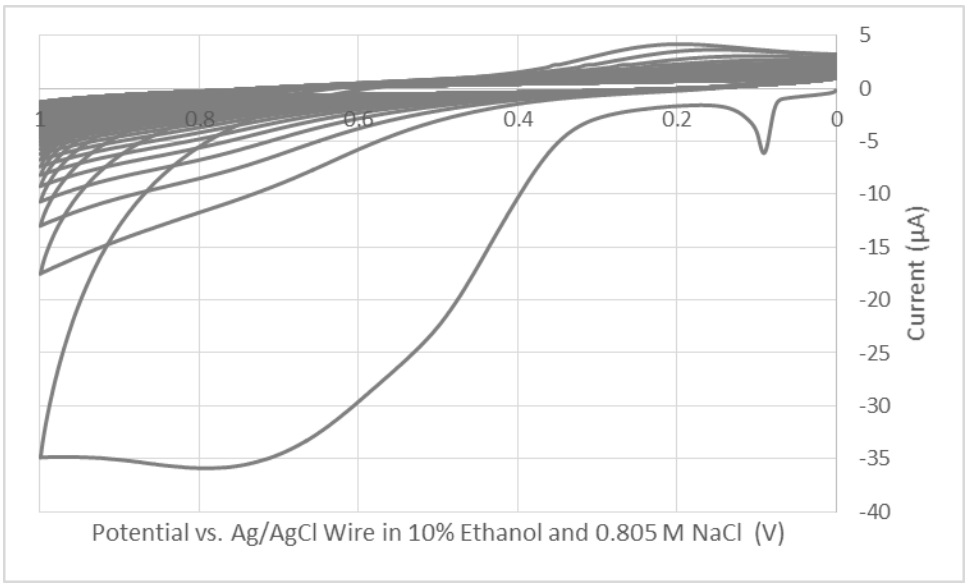

Figure 2.10: Cyclic voltammogram of 8-hydroxyquinoline in NaCl and ethanol. A broad peak is visible near 0.8 V. This cyclic voltammograms shows all 107.5 cycles. This first peak is due to an impurity on the surface of the electrode.

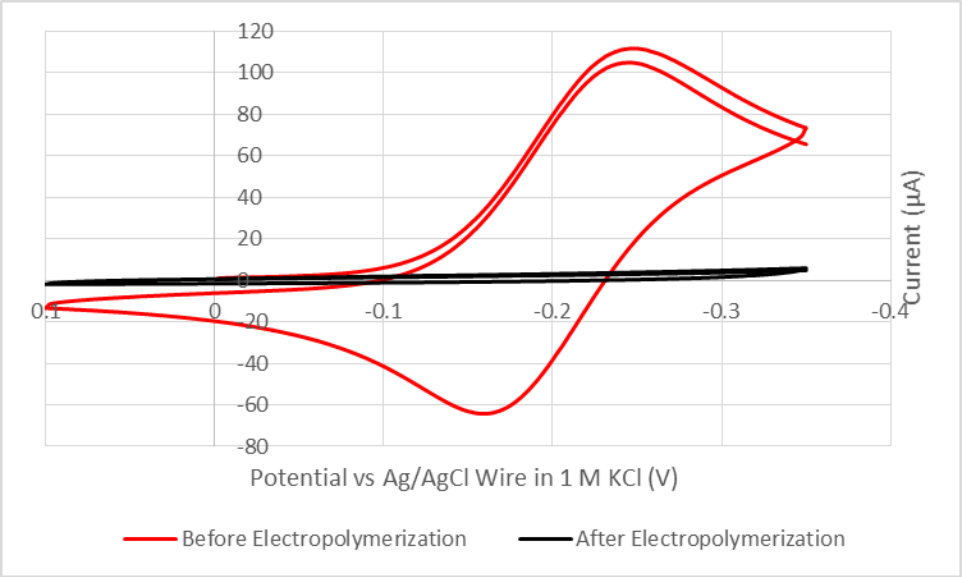

Figure 2.11: Cyclic voltammogram of $Ru(NH_3)_6^{3+/2+}$ before and after electropolymerization of 8-hydroxyquinoline in 10% ethanol and 0.805 M NaCl.

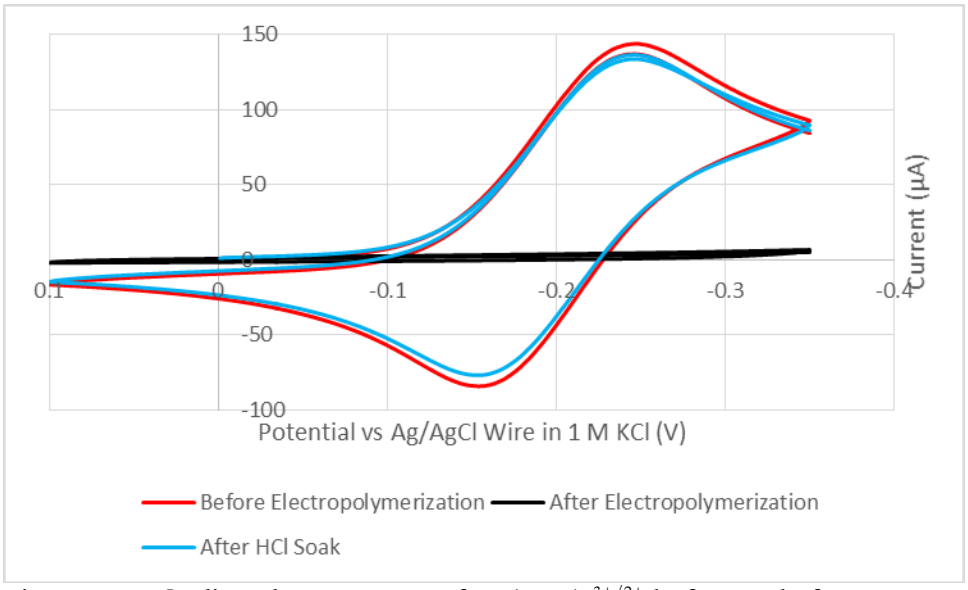

Figure 2.12: Cyclic voltammogram of $Ru(NH_3)_6^{3+/2+}$ before and after electropolymerization of 8-hydroxyquinoline in 10% ethanol and 0.805 M NaCl, and after soaking in 0.1 M HCl.

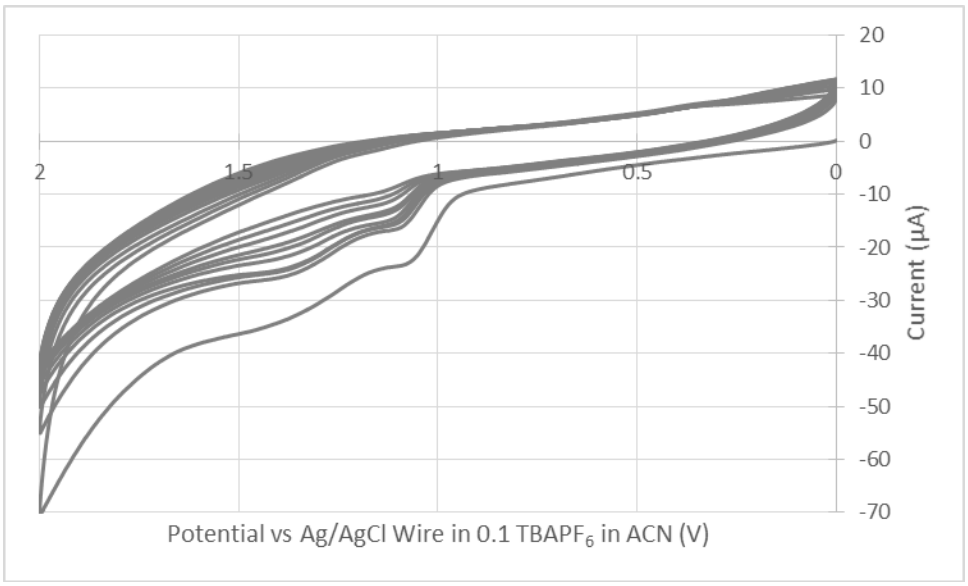

Figure 2.13: Cyclic voltammogram of the electropolymerization of 0.1 M aluminum tris(8-hydroxyquinoline) in 0.1 M tetrabutylammonium hexafluorophosphate ($TBAPF_6$) in acetonitrile. The cyclic voltammagram shows all 20 cycles.

Passivation of the electrode was tested by electropolymerizing the aluminum tris(8-hydroxyquinoline) solution at two different switching potentials and checking for pinholes. Electropolymerizing to 1.2 V yielded a passivating film[2]. Electropolymerizing to 1.7 V also yielded a passivating film, although the film became less passivating as time went on. Figure 2.14 illustrates this: The cyclic voltammograms of $Ru(NH_3)_6^{3+/2+}$ after electropolymerization were taken within two minutes of each other. Over that time, the peak currents return to about the height of those seen of $Ru(NH_3)_6^{3+/2+}$ at a base glassy carbon electrode. Drying in air caused to the film to crack and to change color from yellow to white. Pinhole measurements revealed that this cracked film was better at passivating against $Ru(NH_3)_3^{3+/2+}$ than the "wet" film; this is shown in Figure 2.15. However, the film, under any condition, did not passivate better than electropolymerized phenol.

[2] The cyclic voltammograms are not shown since the only ones available are background subtracted. The background subtraction was performed improperly, leading to distorted cyclic voltammograms.

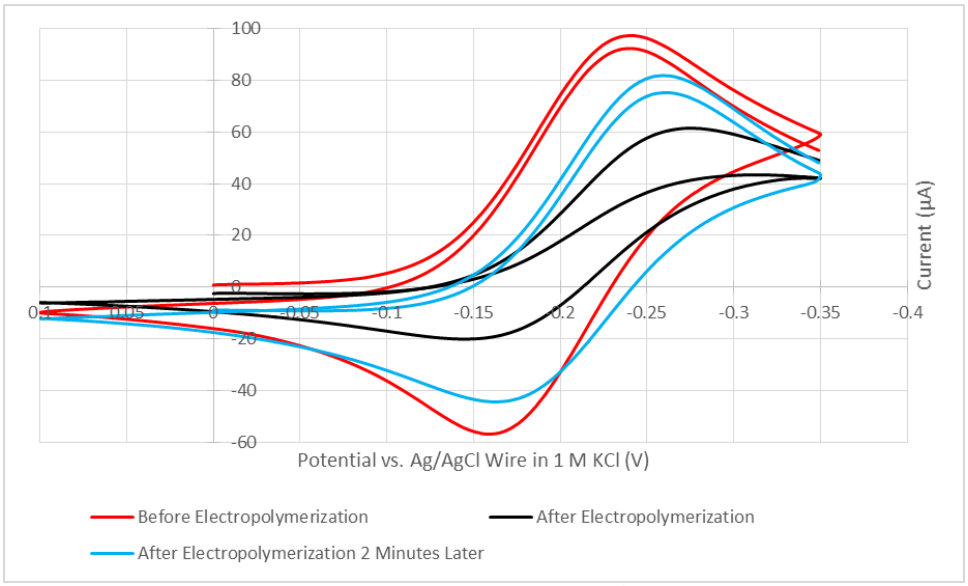

Figure 2.14: Cyclic voltammogram of $Ru(NH_3)_6^{3+/2+}$ before and after electropolymerization of aluminum tris(8-hydroxyquinoline) in 0.1 M $TBAPF_6$ in ACN. Notice how the film does not completely passivate the electrode. Two minutes after the previous cyclic voltammogram, $Ru(NH_3)_6^{3+/2+}$ has permeated the film more.

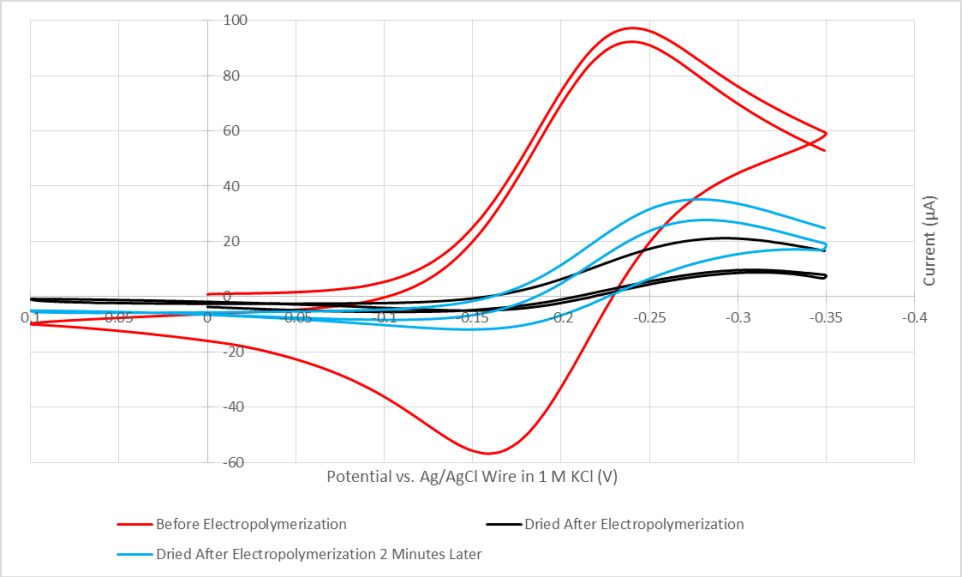

Figure 2.15: Cyclic voltammogram of $Ru(NH_3)_6^{3+/2+}$ before and after electropolymerization of aluminum tris(8-hydroxyquinoline) in 0.1 M $TBAPF_6$ in ACN and after subsequent drying of the film in air. Notice how the dried film does not completely passivate the electrode, but does passivate better than the wet film. Two minutes after the previous cyclic voltammogram, $Ru(NH_3)_6^{3+/2+}$ has permeated the film more.

Phenol in the Presence of Ferrocene

Reference 56 suggested that electropolymerization of phenol in the presence of ferrocene would produce a denser, possibly more crosslinked, thin film. A 50 mM phenol with 100 mM tetrabutylammonium perchlorate, 50 mM tetramethylammonium hydroxide, and 5 mM ferrocene in acetonitrile was prepared. A similar solution without the ferrocene was prepared as a blank. The electropolymerization of both solutions are shown in Figure 2.16. As can be seen, the electropolymerization cyclic voltammogram of the former solution shows a single anodic peak at 0.812 V vs. Ag/AgCl wire. The cyclic voltammogram continues to show passivation of the electrode towards phenol oxidation. The electropolymerization cyclic voltammogram of the phenol with ferrocene solution shows two prominent peaks at 0.4995 V and 0.603 V, and side peak at approximately 0.75 V. The oxidation of ferrocene typically occurs around 0.5 V vs. Ag/AgCl reference wire. The second and third peaks do not have an explanation, although passing through them causes passivation of the electrode, as the cathodic peak for ferrocene is absent. The reduction in peak anodic current in the subsequent cycles appear to be similar to that during the electropolymerization of phenol in the absence of ferrocene. Pinhole measurements in $Ru(NH_3)_6^{3+/2+}$ indicate that electropolymerization of phenol in the presence of ferrocene passivates the glassy carbon electrode better than electropolymerization of phenol in the absence of ferrocene. This data is not shown.

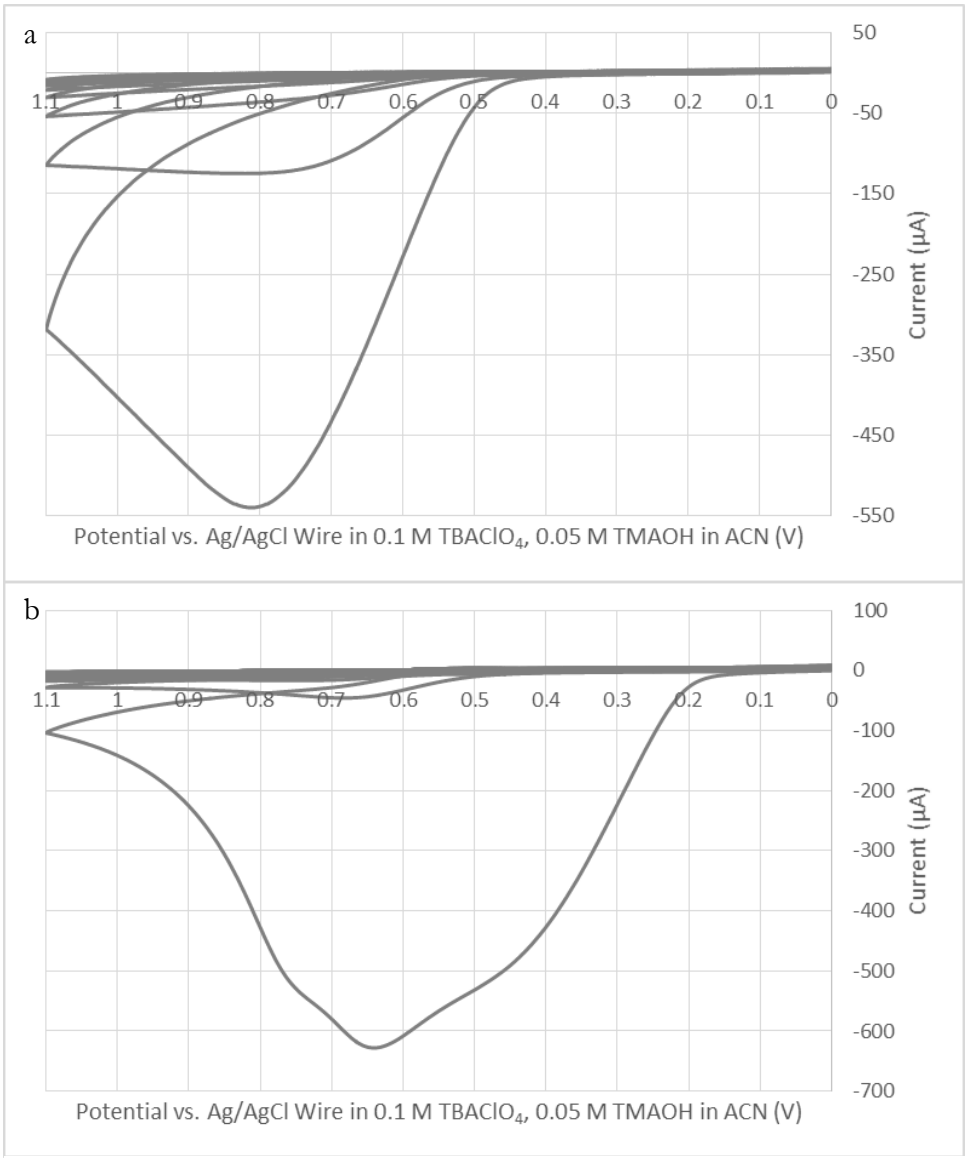

Figure 2.16: (a) Cyclcic voltammogram of the electropolymerization of phenol in 0.1 M $TBAClO_4$ and 0.05 M TMAOH in ACN. Note the oxidation potential is similar to that of phenol in acidic conditions. The cyclic voltammogram shows all 20 cycles. (b) Cyclic voltammogram of phenol in 0.1 M $TBAClO_4$ and 0.05 M TMAOH in ACN in the presence of 0.005 M ferrocene. Ferrocene typically oxidizes near 0.5 V. The cyclic voltammogram shows all 50 cycles.

4-Vinylphenol

4-Vinylphenol was of interest because of its two functional groups: It possesses a hydroxyl functional group and a vinyl functional group. References 51 and 51 suggested that reductive electropolymerization of the vinyl group was possible. Reductive electropolymerization would leave the hydroxyl groups available for metal oxide deposition. A 50 mM 4-vinylphenol with 0.1 M $TBAPF_6$ in acetonitrile solution was prepared in the glovebox to eliminate interference from oxygen and water (Recall that at potentials more negative than ~ –0.7 V vs Ag/AgCl reference wire, oxygen reduces to water). A typical reductive electropolymerization cyclic voltammogram is shown in Figure 2.17. The peak potential occurs at about –2.6 V vs. Ag/AgCl reference wire. Note how the cyclic voltammogram does not show the same drastic reduction in current during the second cycle as was seen for the oxidative electropolymerization of previous compounds. Nonetheless, the current decreases with each cycle. Complete passivation of the electrode is never attained.

The resulting film displayed passivation toward $Ru(NH_3)_6^{3+/2+}$, although not the extent seen for previous films; anodic and cathodic peaks are visible in the cyclic voltammogram shown in Figure 2.18. Two other pinhole solutions were tested, $Fe(CN)_6^{4-/3-}$ and $Fc^{0/+}$. The resulting film also displayed almost insignificant passivation towards $Fc^{0/+}$, yet passivation towards $Fe(CN)_6^{4-/3-}$ resembled that of $Ru(NH_3)_6^{3+/2+}$. This may be due to different polarities of the solvents. The $Fc^{0/+}$ solution is prepared in acetonitrile, whereas the $Fe(CN)_6^{4-/3-}$ and $Ru(NH_3)_6^{3+/2+}$ are prepared in water. The film may be slightly hydrophobic, which helps it block against the electron transfer of $Fe(CN)_6^{4-/3-}$ and $Ru(NH_3)_6^{3+/2+}$, while in a less polar solvent, such as acetonitrile, the film is slightly solubilized, allowing for electron

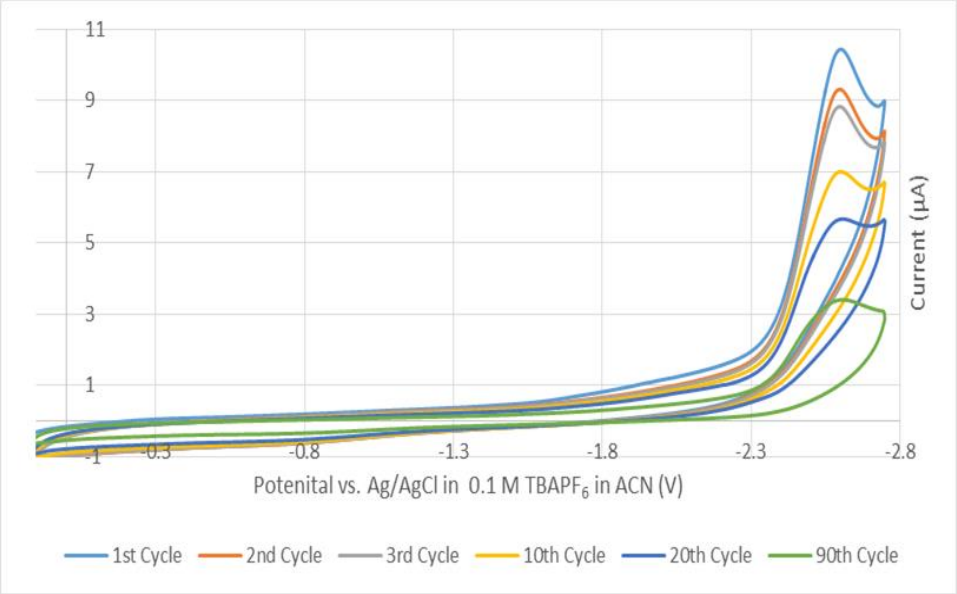

Figure 2.17: Stepwise cyclic voltammogram of the electropolymerization of 4-vinylphenol in 0.1 $TBAPF_6$ in ACN. The cyclic voltammogram shows the first, second, third, tenth, twentieth and ninetieth cycle for clarity.

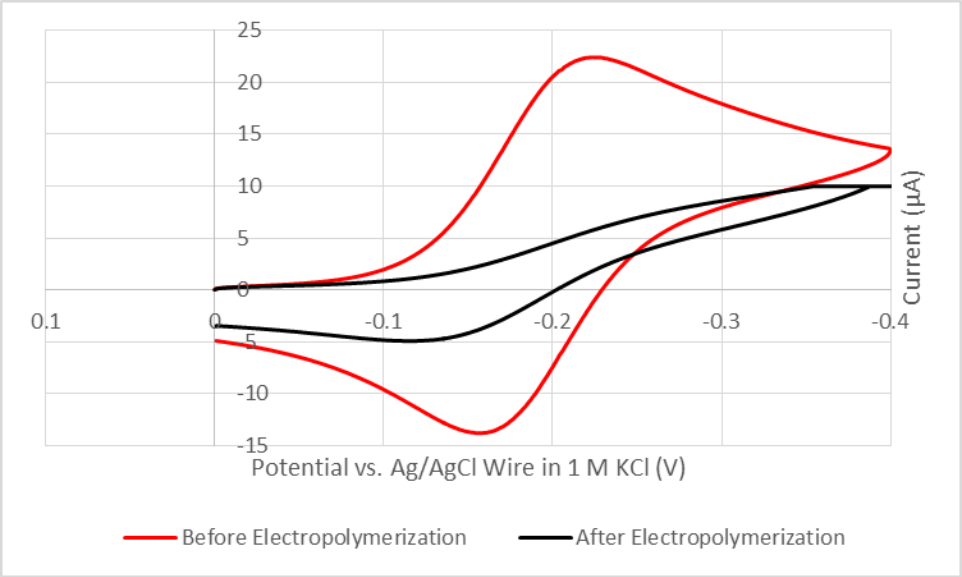

Figure 2.18: Cyclic voltammogram of $Ru(NH_3)_6^{3+/2+}$ before and after reductive electropolymerization of 4-vinylphenol in 0.1 M $TBAPF_6$ in ACN.

transfer for $Fc^{0/+}$. Cyclic voltammograms of these pinhole reagents before and after electropolymerization of the electrode are shown in Figure 2.19.

Oxidation of 4-vinylphenol in acetonitrile was also investigated. The electropolymerization cyclic voltammogram at a gold electrode is shown in Figure 2.20. Three identifiable peaks are present. The behavior of passivation is similar to that of other compounds: as the cycles continue, the film becomes more passivating towards itself. The film did not completely block the electron transfer of $Ru(NH_3)_6^{3+/2+}$; illustrated in Figure 2.21, small, yet distinguishable peaks are visible. The film completely blocked electron transfer to and from $Fe(CN)_6^{4-/3-}$ and $Fe^{0/+}$. These cyclic voltammograms are shown in Figure 2.22. Because of this behavior, the 4-vinylphenol solution was electropolymerized onto a gold finger, whose fabrication is detailed in Chapter 3. Atomic force microscopy was performed to determine the height of the film: 11.9 ± 4.6 nm.

Experiments investigating reductive electropolymerization followed by oxidative electropolymerization and vice versa were performed. Both techniques passivated the electrode against the pinhole reagents about as well as the oxidative electropolymerization procedure alone.

50 mM 4-vinylphenol and 0.1 M $TBAPF_6$ in N, N-dimethylformamide was prepared. This solution was reductive electropolymerized, having a peak potential in the first cycle around –2.85 V vs. Ag/AgCl. As seen with the 4-vinylphenol solution in acetonitrile, the electropolymerization does not passivate the electrode towards 4-vinylphenol reduction even after 90 cycles. Passivation towards $Ru(NH_3)_6^{3+/2+}$ is about the same as that measured with the film electropolymerized in acetonitrile. The film prepared in DMF shows slightly more passivation against $Fe(CN)_6^{4-/3-}$, and better passivation against $Fc^{0/+}$, though still not

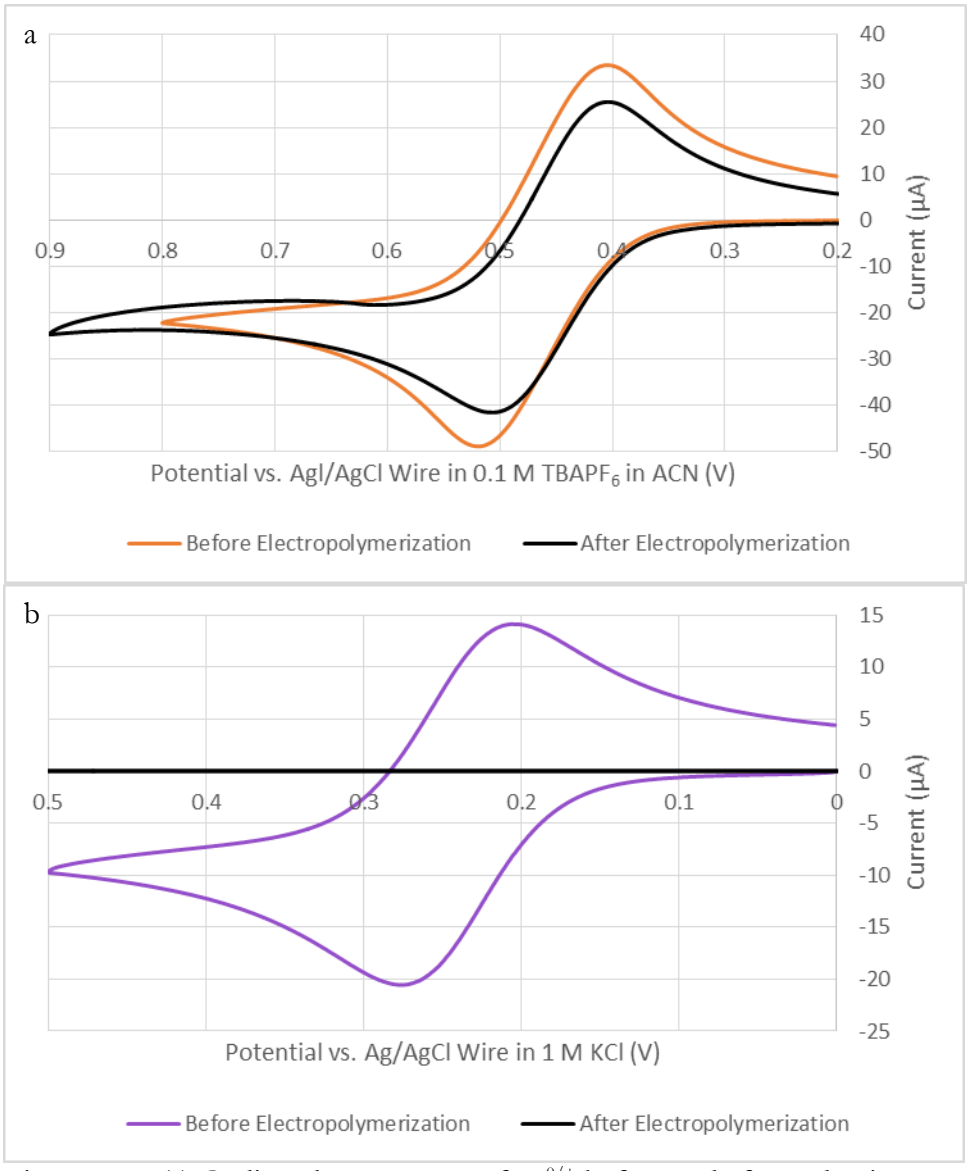

Figure 2.19: (a) Cyclic voltammogram of $Fc^{0/+}$ before and after reductive electropolymerization of 4-vinylphenol in 0.1 M $TBAPF_6$ in ACN. (b) Cyclic voltammogram of $Fe(CN)_6^{4-/3-}$ before and after reductive electropolymerization of 4-vinylphenol in 0.1 M $TBAPF_6$ in ACN.

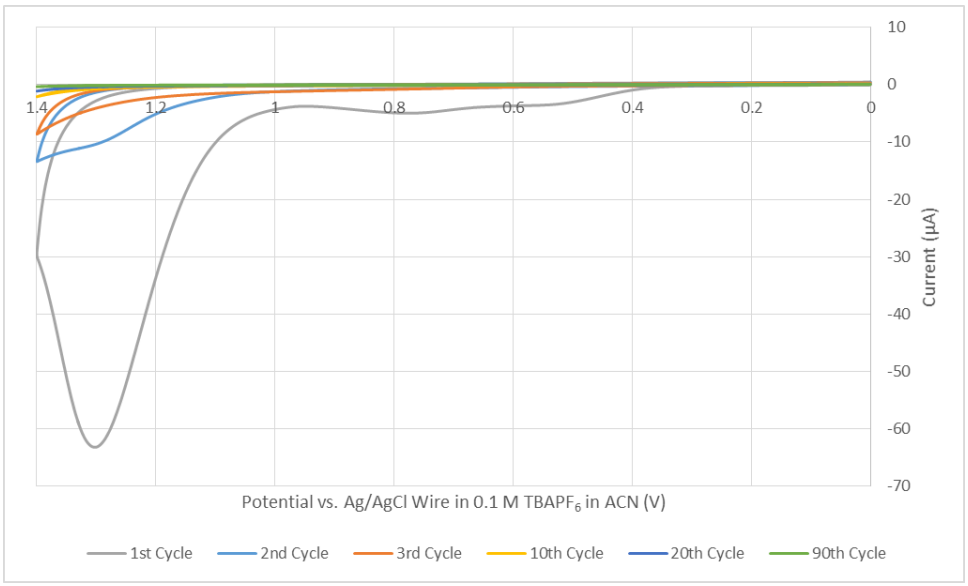

Figure 2.20: Stepwise cyclic voltammogram of the electropolymerization of 4-vinylphenol in 0.1 M $TBAPF_6$ in ACN. What causes the two minor peaks is unknown.

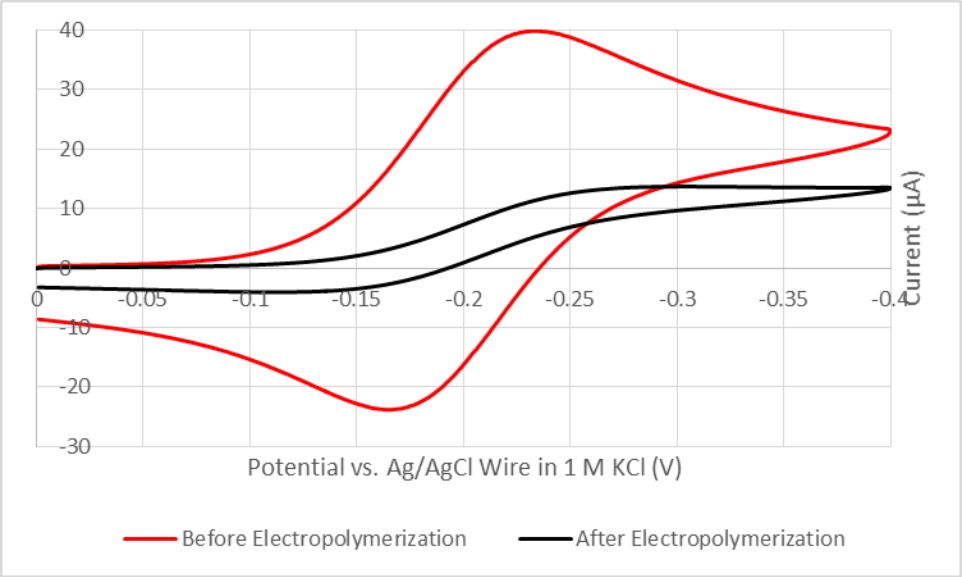

Figure 2.21: Cyclic voltammogram of $Ru(NH_3)_6^{3+/2+}$ before and after oxidative electropolymerization of 4-vinylphenol in 0.1 M $TBAPF_6$ in ACN.

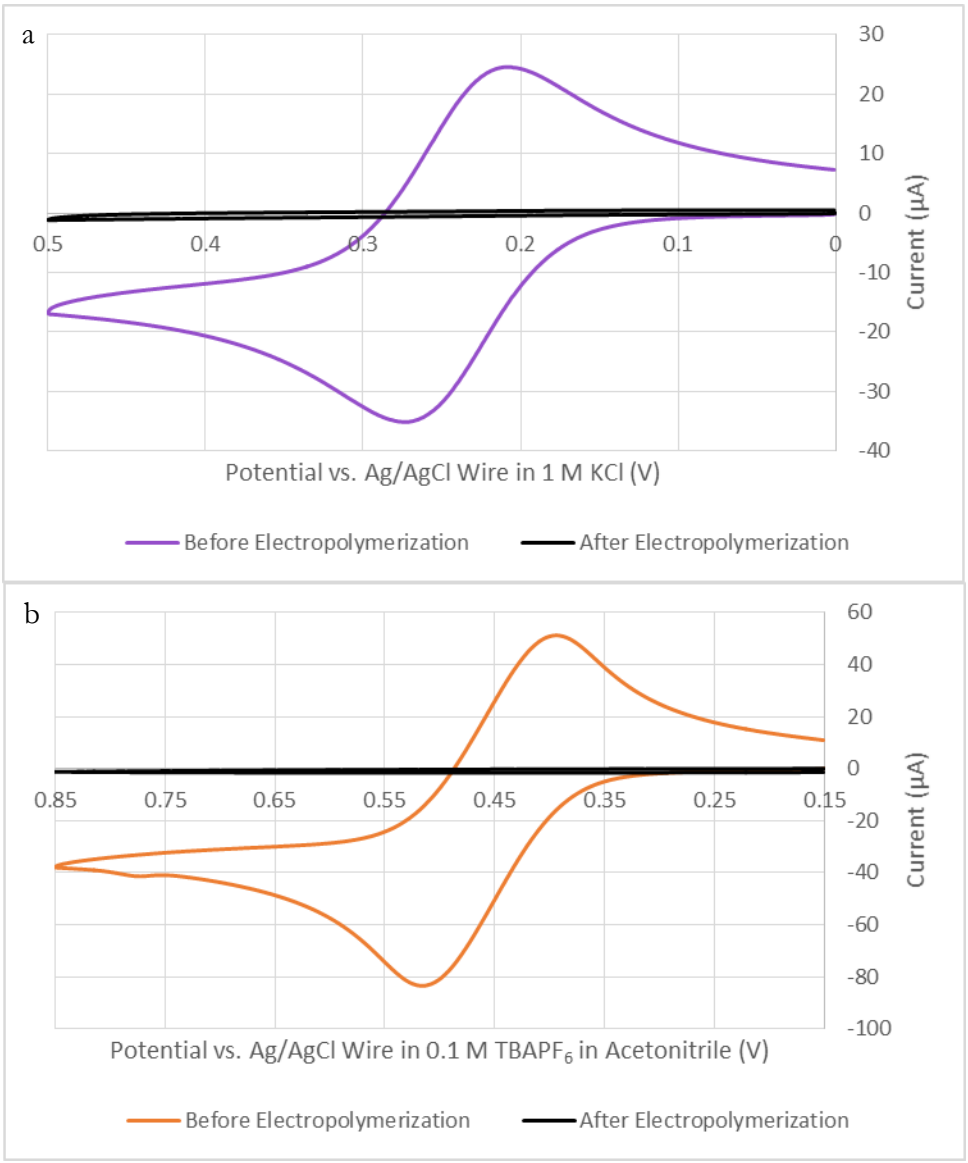

Figure 2.22: (a) Cyclic voltammogram of $Fe(CN)_6^{4-/3-}$ before and after oxidative electropolymerization of 4-vinylphenol in 0.1 M $TBAPF_6$ in ACN. (b) Cyclic voltammogram of $Fc^{0/+}$ before and after oxidative electropolymerization of 4-vinylphenol in 0.1 M $TBAPF_6$ in ACN.

completely blocking electron transfer completely. Figure 2.23 illustrates the reductive electropolymerization and $Ru(NH_3)_6^{3+/2+}$, and Figure 2.24 contains the cyclic voltammograms for $Fe(CN)_6^{4-/3-}$ and $Fc^{0/+}$.

The 4-vinylphenol in DMF was also oxidatively electropolymerized. The results are similar to those obtained from the oxidative electropolymerization of 4 vinylphenol in acetonitrile.

Experiments investigating oxidative electropolymerization followed by radical chain polymerization were also conducted. For the most part, radical chain polymerization did not affect the passivation of the electrode towards $Ru(NH_3)_3^{3+/2+}$, $Fc^{0/+}$, and $Fe(CN)_6^{4-/3-}$, as seen in Figures 1.25 and 1.26; radical chain polymerization passivates the electrode almost identically as oxidative polymerization, as seen in Figure 2.26b. Thus, I determined oxidative electropolymerization to be the best method of passivating the electrode.

50 mM 4-vinylphenol in 1 M KCl was oxidatively electropolymerized on gold outside of the glovebox. Figure 2.27 illustrates the cyclic voltammogram of a typical electropolymerization on a 2 mm gold electrode. The peak occurs at 0.719 V vs. Ag/AgCl reference wire. Like many other cyclic voltammograms involving oxidative electropolymerization, the subsequent cycles show passivation of the electrode. The electropolymerization did not completely block $Ru(NH_3)_6^{3+/2+}$; it did completely block $Fe(CN)_6^{4-/3-}$. These cyclic voltammograms are shown in Figure 2.28. Interestingly, on a glassy carbon electrode, the film completely blocked $Ru(NH_3)_6^{3+/2+}$ and $Fe(CN)_6^{4-/3-}$; the film did not block against $Fc^{0/+}$.

The film was exposed to two radical initiators: 2,2'-azobis(2-methylpropionitrile)-2-(azo(1-cyano-1-methylethyl))-2-methylpropanenitrile (AIBN) and dibenzoyl peroxide. Both radical initiators were dissolved in DMF; the beaker containing DMF was placed in a water

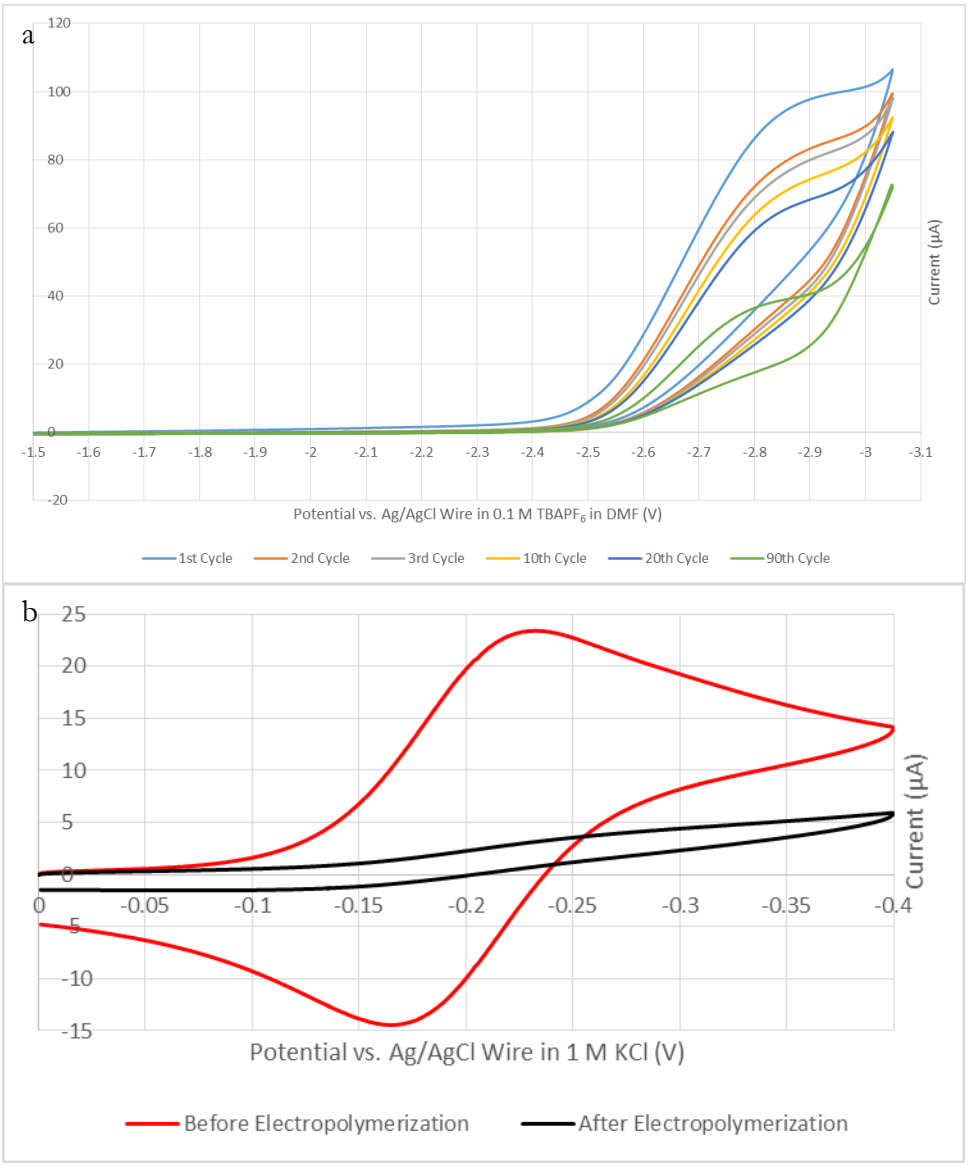

Figure 2.23: (a) Stepwise cyclic voltammogram of the reductive electropolymerization of 4-vinylphenol in 0.1 M $TBAPF_6$ in DMF. (b) Cyclic voltammogram of $Ru(NH_3)_6^{3+/2+}$ before and after reductive electropolymerization of 4-vinylphenol in 0.1 M $TBAPF_6$ in DMF.

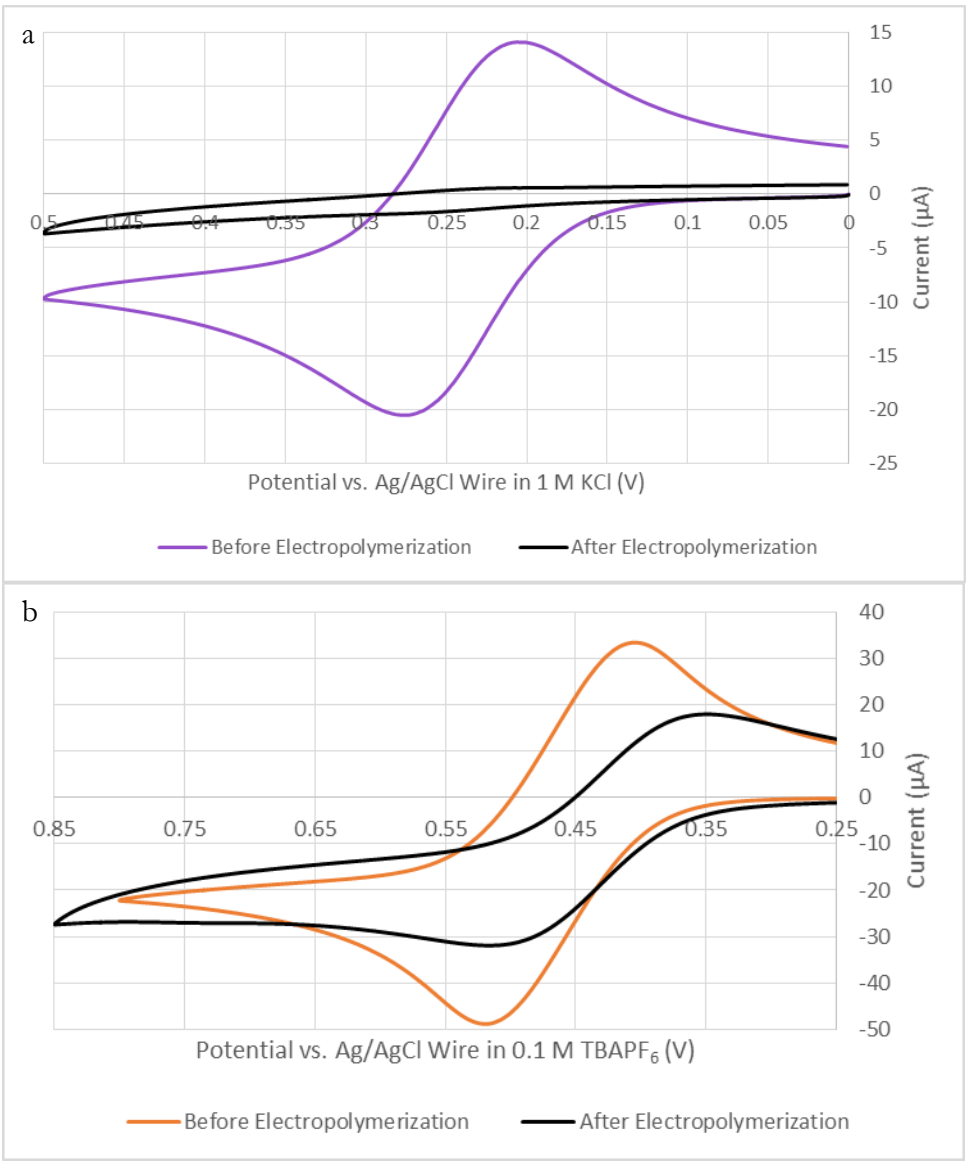

Figure 2.24: (a) Cyclic voltammogram of $Fe(CN)_6^{4-/3-}$ before and after reductive electropolymerization of 4-vinylphenol in 0.1 M $TBAPF_6$ in DMF. Notice the presence of small peaks near 0.26 V and 0.21 V. (b) Cyclic voltammogram of $Fc^{0/+}$ before and after reductive electropolymerization of 4-vinylphenol in 0.1 M $TBAPF_6$ in DMF.

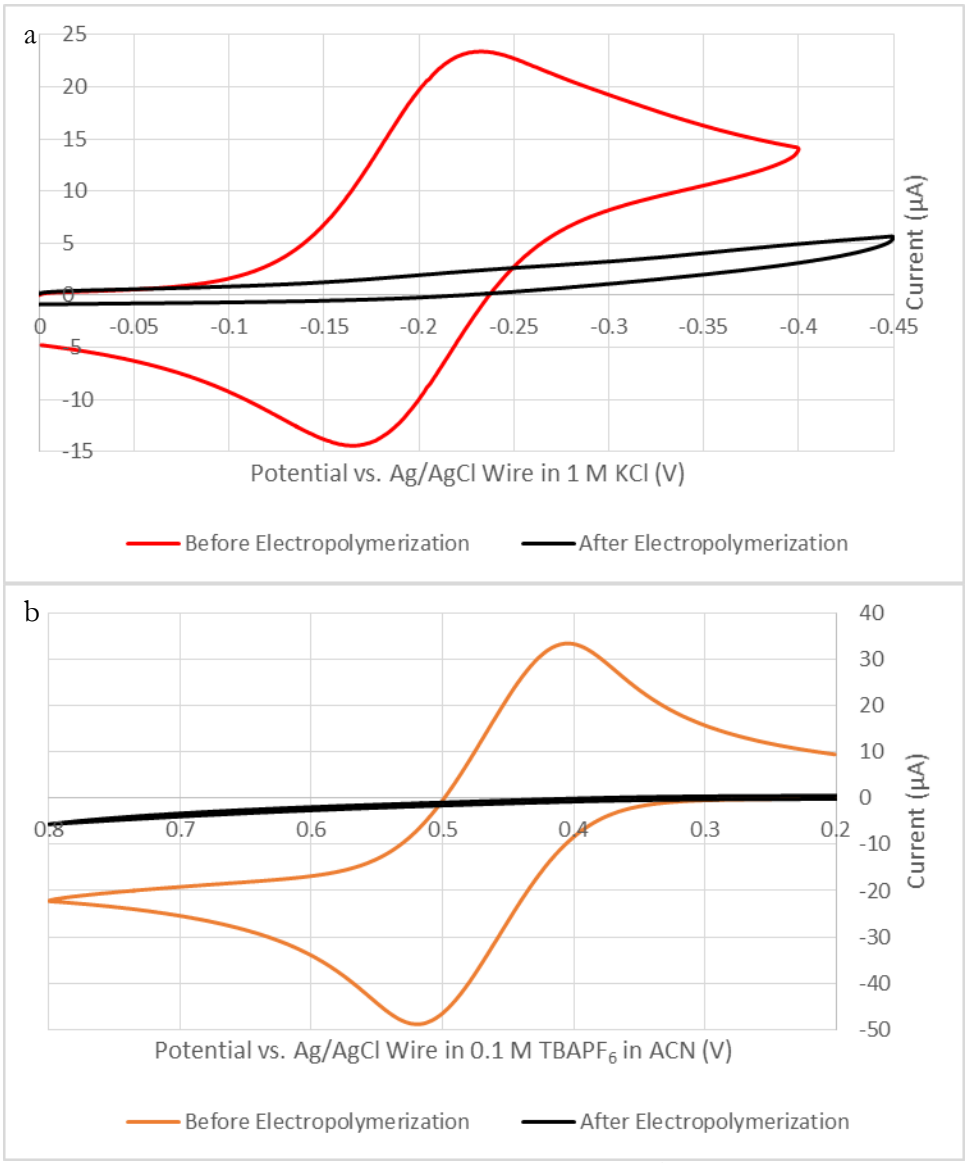

Figure 2.25: (a) Cyclic voltammogram of $Ru(NH_3)_6^{3+/2+}$ before and after oxidative electropolymerization of 4-vinylphenol in 0.1 M $TBAPF_6$ in DMF. (b) Cyclic voltammogram of $Fc^{0/+}$ before and after oxidative electropolymerization of 4-vinylphenol in 0.1 M $TBAPF_6$ in DMF.

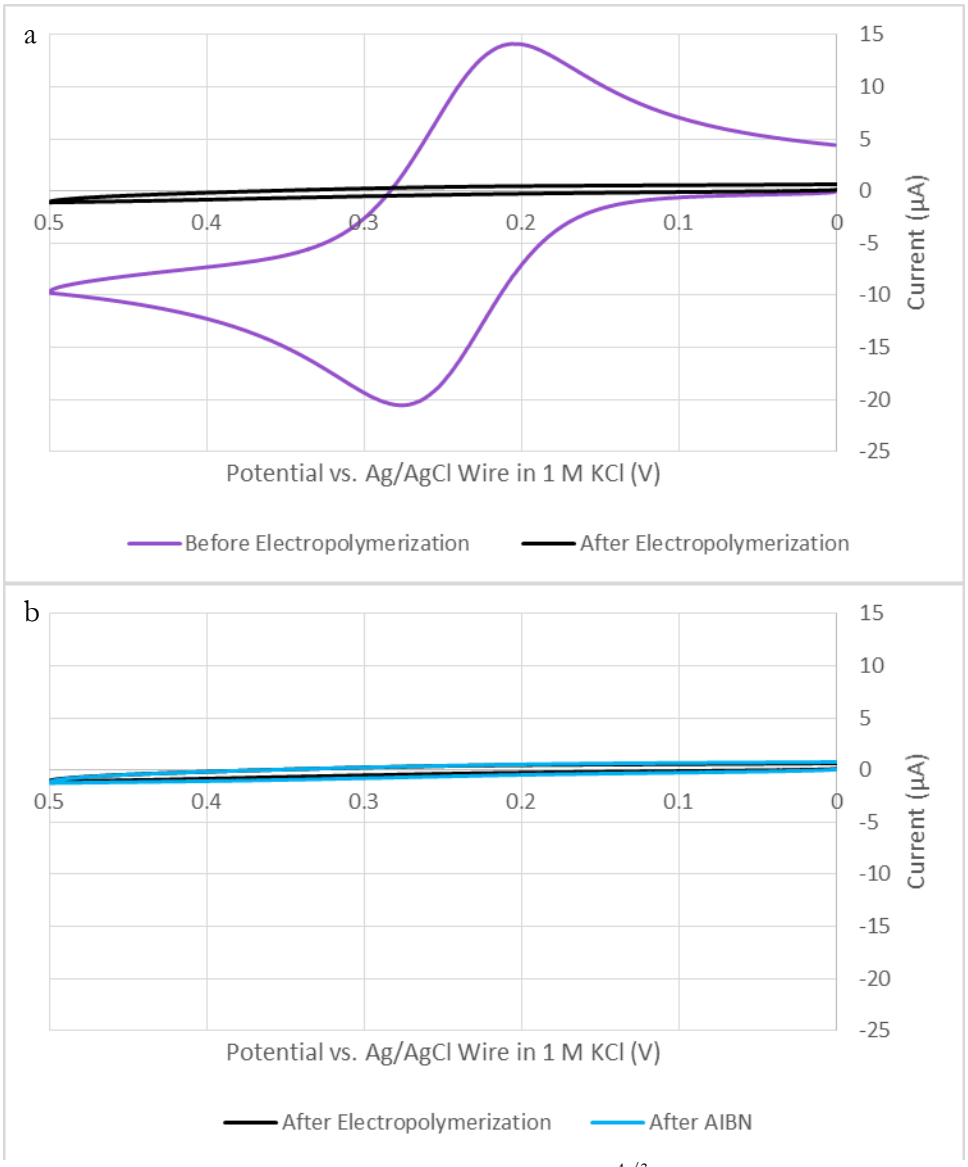

Figure 2.26: (a) Cyclic voltammogram of $Fe(CN)_6^{4-/3-}$ before and after oxidative electropolymerization of 4-vinylphenol in 0.1 M $TBAPF_6$ in DMF. (b) Cyclic voltammogram of $Fe(CN)_6^{4-/3-}$ before and after exposure of the 4-vinylphneol film to AIBN. Notice that the voltammograms before and after exposure are nearly identical.

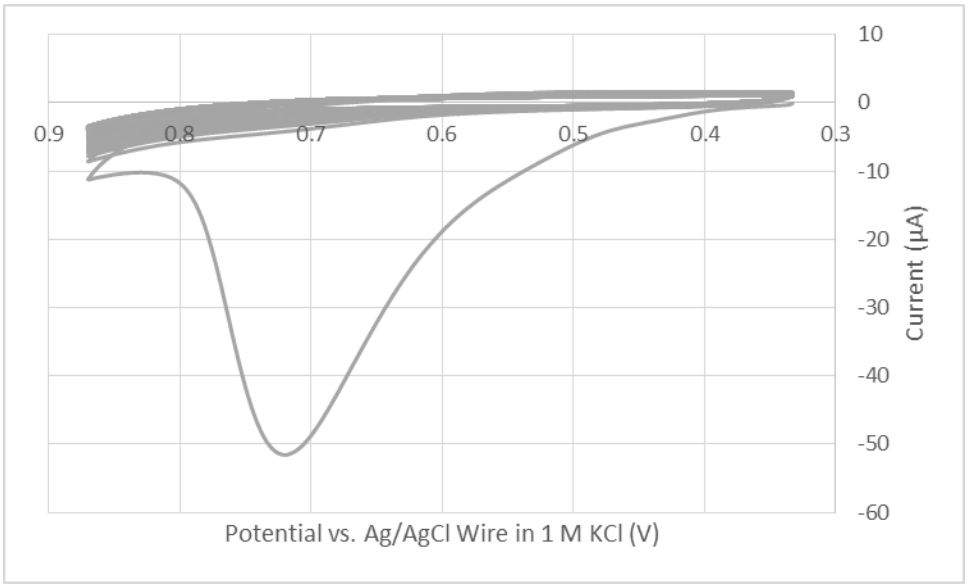

Figure 2.27: Cyclic voltammogram of 4-vinylphenol in 1 M KCl at a 2 mm Au electrode. This figure shows all 90 cycles.

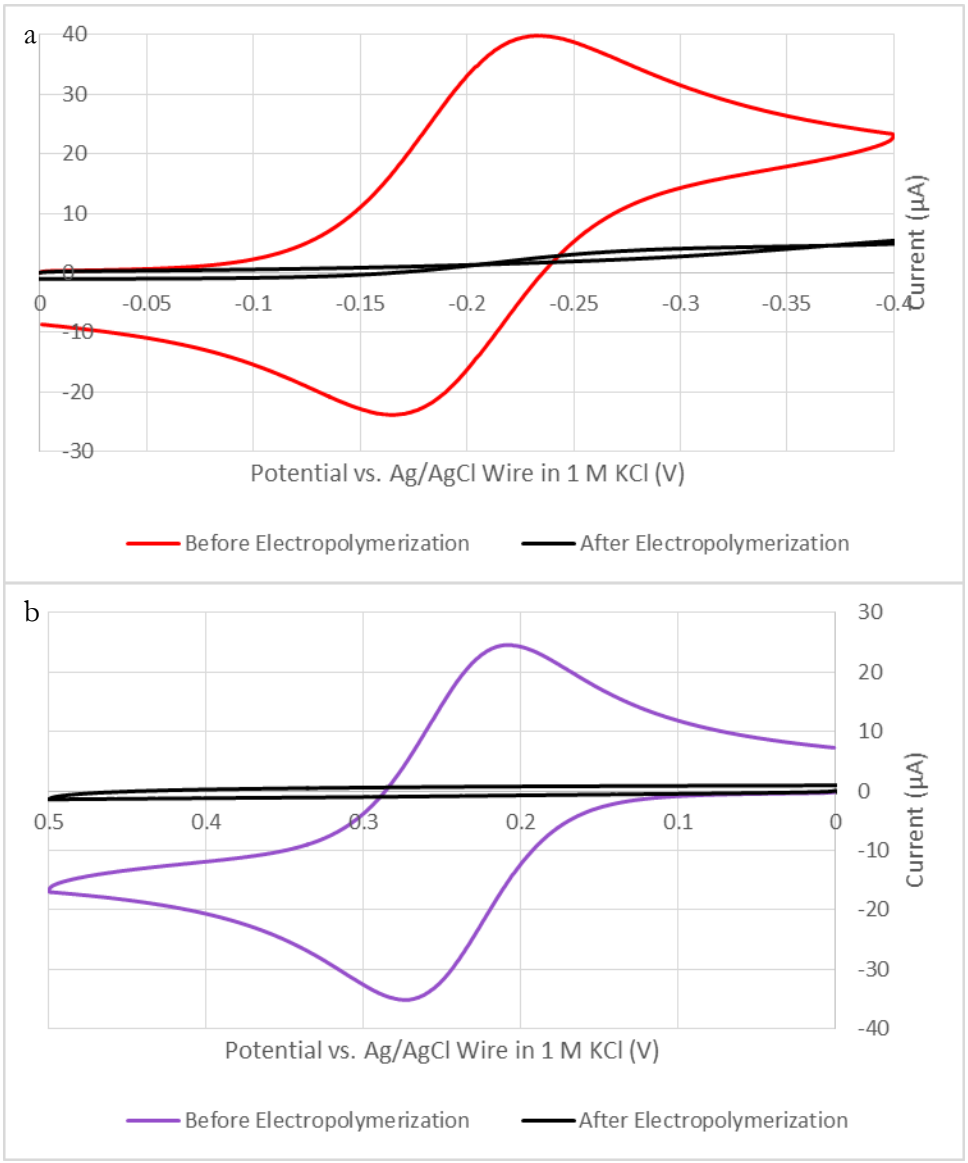

Figure 2.28: (a) Cyclic voltammogram of $Ru(NH_3)_6^{3+/2+}$ before and after oxidative electropolymerization of 4-vinylphenol in 1M KCl at a 2 mm Au electrode. (b) Cyclic voltammogram of $Fe(CN)_6^{4-/3-}$ before and after oxidative electropolymerization of 4-vinylphenol in 1 M KCl at a 2 mm Au electrode.

bath of 67 °C; the oxidatively electropolymerized film was then placed into the DMF for about five minutes. Afterwards, pinhole measurements were performed on the film. After exposure to AIBN, the film actually blocked less $Ru(NH_3)_6^{3+/2+}$ than before AIBN exposure, while performing about the same in the $Fe(CN)_6^{4-/3-}$ as compared to before AIBN exposure. The opposite occurred after exposure to dibenzoyl peroxide: the dibenzoyl peroxide exposed film performed the same in $Ru(NH_3)_6^{3+/2+}$ as compared to the before exposed electropolymerized film, while the resultant film performed worse in $Fe(CN)_6^{4-/3-}$ than the electropolymerized film. Both dibenzoyl peroxide exposed films were impermeable to $Fc^{0/+}$. Voltammograms of the pinhole measurements are shown in Figures 1.29 and 1.30. Subsequent experiments showed that the film was soluble in acetonitrile.

50 mM 4-vinylphenol in 0.1 M NaOH was oxidatively electropolymerized outside the glovebox. Figure 2.31a shows a typical electropolymerization cyclic voltammogram at a 1.5 mm glassy carbon electrode. The peak potential occurs at 0.155 V vs. Ag/AgCl reference wire. As is typical of oxidative electropolymerization of phenols, subsequent cycles show passivation of the electrode. The film shows good passivation towards $Ru(NH_3)_6^{3+/2+}$, excellent passivation towards $Fe(CN)_6^{4-/3-}$, and poor passivation towards $Fc^{0/+}$. Interestingly, the film allowed the oxidation of $Fc^{0/+}$, but did not allow the reduction to occur, which implies some selectivity of the film. The film was not placed into solutions containing AIBN or dibenzoyl peroxide. Figure 2.31b and 1.32 illustrates the pinhole measurements. Interestingly, after rinsing the electropolymerized film with acetonitrile, the film was not removed from the electrode; this was shown in Figure 2.32a, in which the cyclic voltammograms of $Fe(CN)_6^{4-/3-}$ after electropolymerization and after rinsing in acetonitrile are similar.

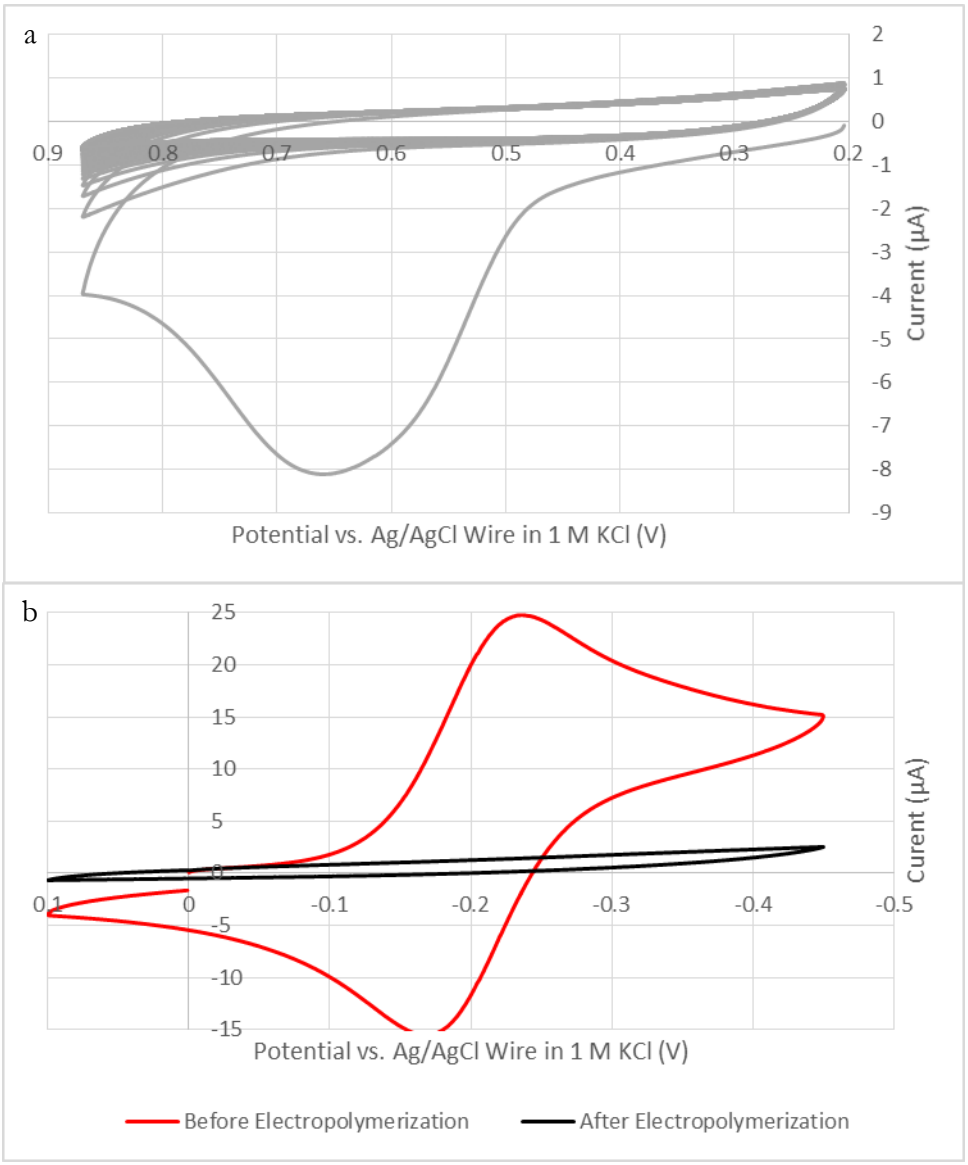

Figure 2.29: (a) Cyclic voltammogram of 4-vinylphenol in 1 M KCl at a 1.5 mm glassy carbon electrode. This figure shows all 90 cycles. (b) Cyclic voltammogram of $Ru(NH_3)_6^{3+/2+}$ before and after oxidative electropolymerization of 4-vinylphenol in 1M KCl at a 1.5mm glassy carbon electrode.

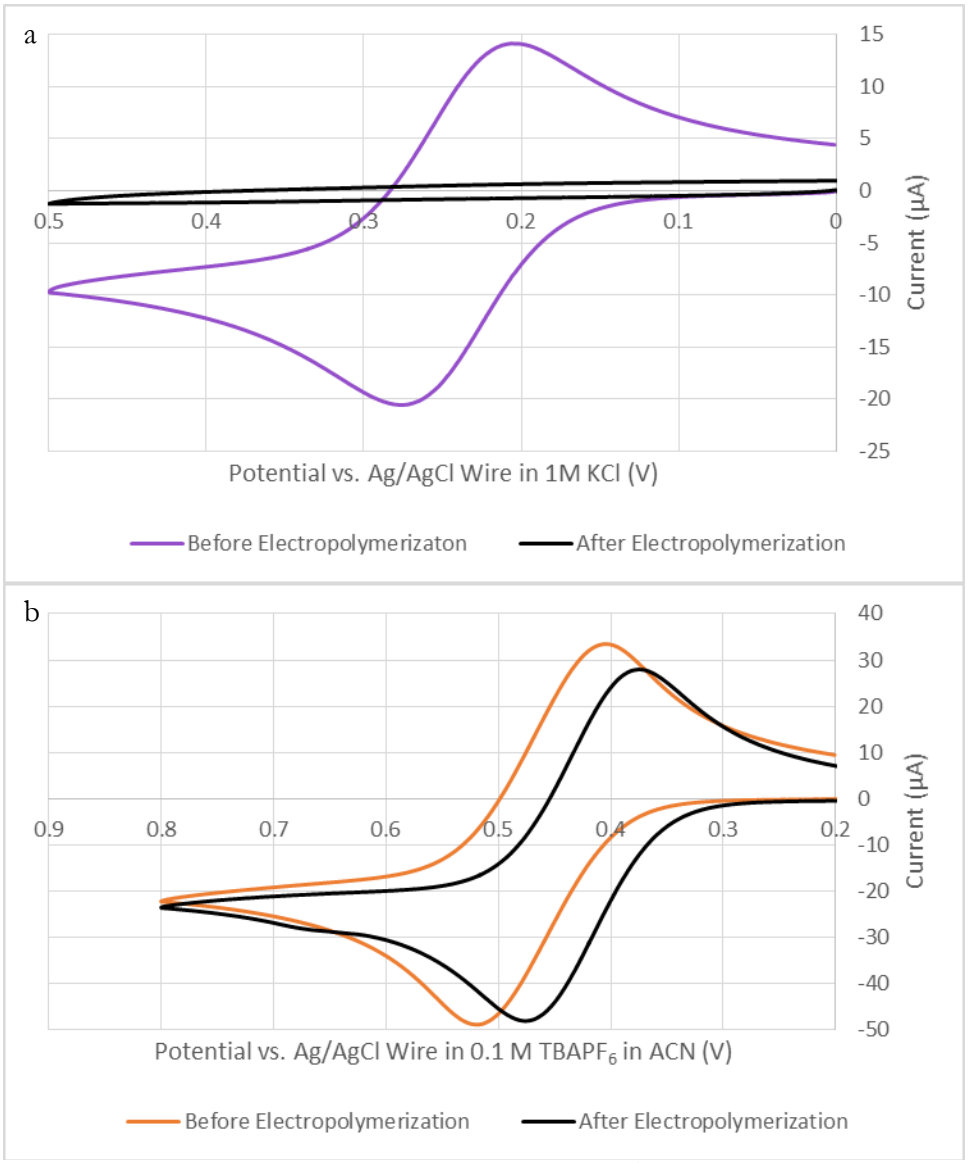

Figure 2.30: (a) Cyclic voltammogram of $Fe(CN)_6^{4-/3-}$ before and after oxidative electropolymerization of 4-vinylphenol in 1 M KCl at a 1.5 mm glassy carbon electrode. (b) Cyclic voltammogram of $Fc^{0/+}$ before and after oxidative electropolymerization of 4-vinylphenol in 1 M KCl at a 1.5 mm glassy carbon electrode.

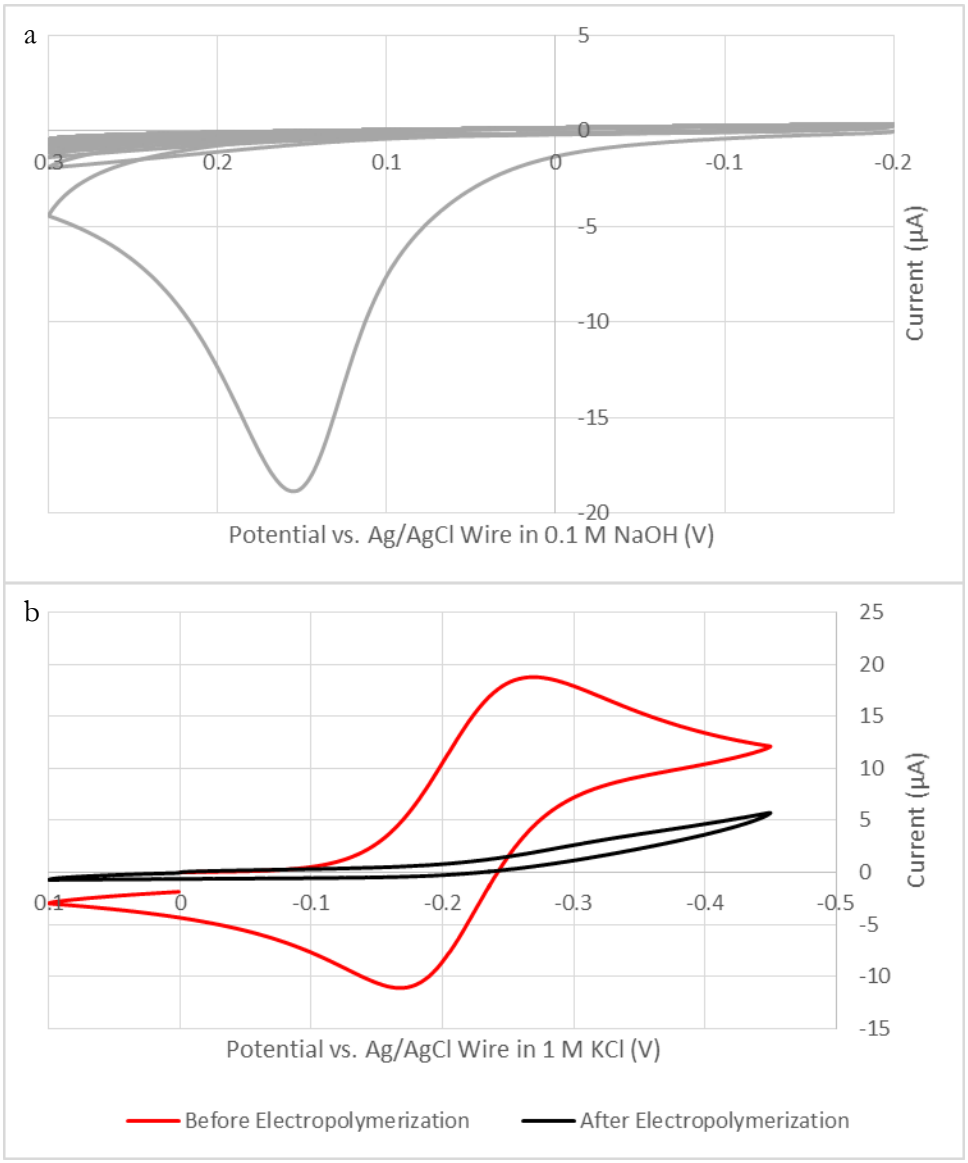

Figure 2.31: (a) Cyclic voltammogram of 4-vinylphenol in 0.1 M NaOH at a 1.5 mm glassy carbon electrode. This figure shows all 90 cycles. (b) Cyclic voltammogram of $Ru(NH_3)_6^{3+/2+}$ before and after oxidative electropolymerization of 4-vinylphenol in 0.1 M NaOH at a 1.5 mm glassy carbon electrode.

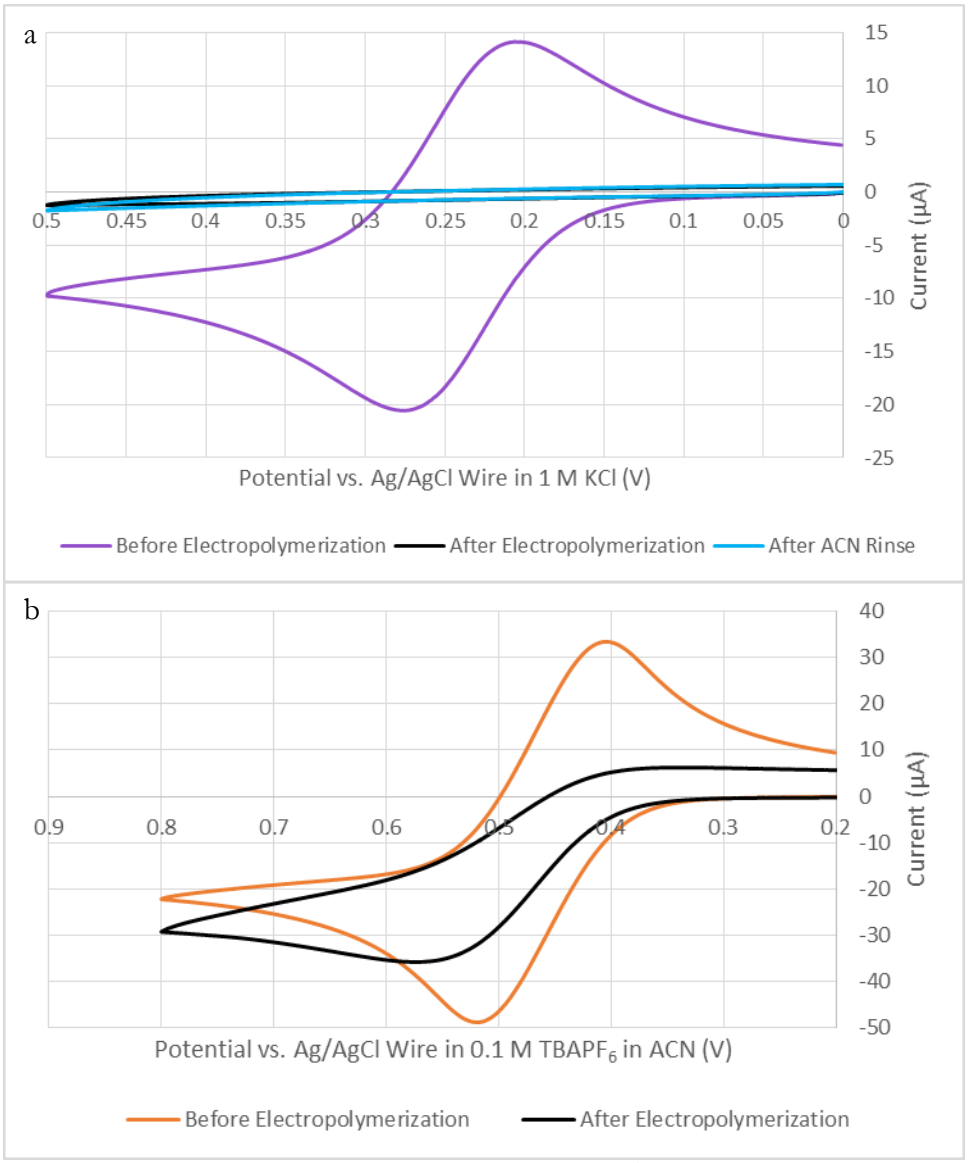

Figure 2.32: (a) Cyclic voltammogram of $Fe(CN)_6^{4-/3-}$ before and after oxidative electropolymerization of 4-vinylphenol in 0.1 M NaOH at a glassy carbon electrode. (b) Cyclic voltammogram of $Fc^{0/+}$ before and after oxidative electropolymerization of 4-vinylphenol in 0.1 M NaOH at a 1.5 mm glassy carbon electrode.

4-Vinylaniline

50 mM 4-vinylaniline in 0.1 M $TBAPF_6$ in DMF was reductively electropolymerized inside the glovebox. The electropolymerization cyclic voltammogram is shown in Figure 2.33. The voltammograms has two cathodic and two anodic peaks. The cathodic peaks occur at –1.755 V and –1.877 V vs. Ag/AgCl wire; the anodic peaks occur at ~ –1.669 V and ~ –0.646 V vs. Ag/AgCl reference wire. A background cyclic voltammogram had a cathodic peak at –1.755 V; this is most likely an impurity in the DMF solvent. Moreover, whatever impurity was reduced is not oxidized. Hence, products of the 4-vinylaniline electropolymerization most likely caused the oxidation peaks seen in the electropolymerization voltammogram. Unlike oxidative electropolymerization of other compounds, reductive electropolymerization of 4-vinylaniline does not result in passivation of the glassy carbon electrode. This is further validated by pinhole measurements in $Ru(NH_3)_6^{3+/2+}$ and $Fe(CN)_6^{4-/3-}$, both of whose cyclic voltammograms are shown in Figure 2.34. While both voltammograms show some passivation towards the two pinhole agents, the decrease in current is not the same as those with oxidatively electropolymerized films.

50 mM 4-vinylaniline in 0.1 M $TBAPF_6$ in ACN was reductively electropolymerized inside the glovebox. The electropolymerization cyclic voltammogram is shown in Figure 2.35. This voltammogram has three reductive peaks and two oxidative peaks in the first cycle.

Subsequent cycles show a disappearance of the first cathodic peak, while decrease in the peak currents are observed in the two most cathodic and anodic peaks. Like other reductive electropolymerizations, this cyclic voltammogram does not show complete passivation of the electrode. This is further confirmed by the cyclic voltammograms of the pinhole reagents. All cyclic voltammograms of the three pinhole reagents show modest decreases in peak

current after electropolymerization compared to before electropolymerization. This means either the film formed is thin, or the film does not uniformly cover the electrode. The cyclic voltammograms are shown in Figure 2.35b and 1.36.

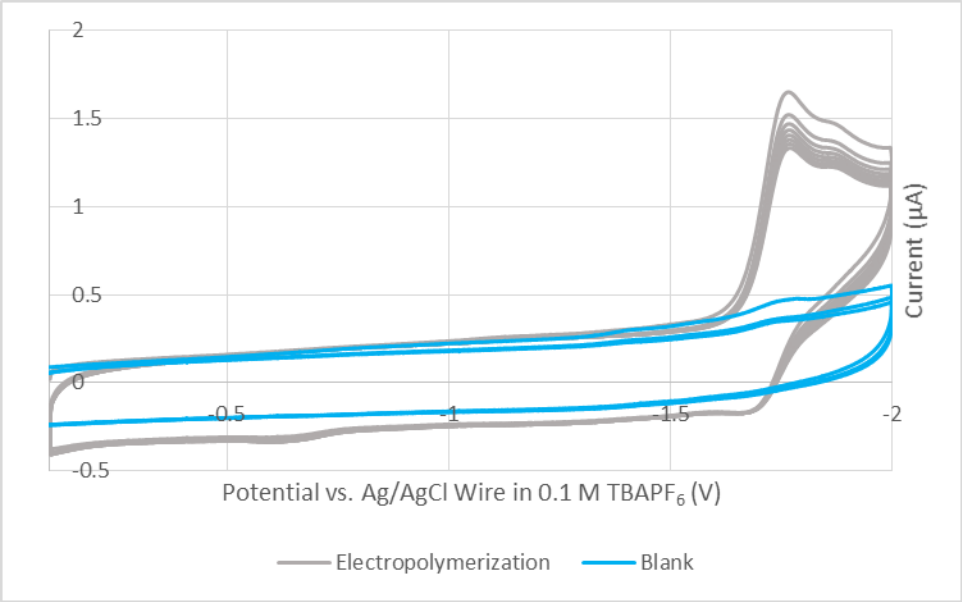

Figure 2.33: Cyclic voltammogram of 4-vinylaniline in 0.1 M $TBAPF_6$ in DMF at a glassy carbon electrode. This figure shows all 87 cycles. Three cycles were performed before this cyclic voltammogram was taken.

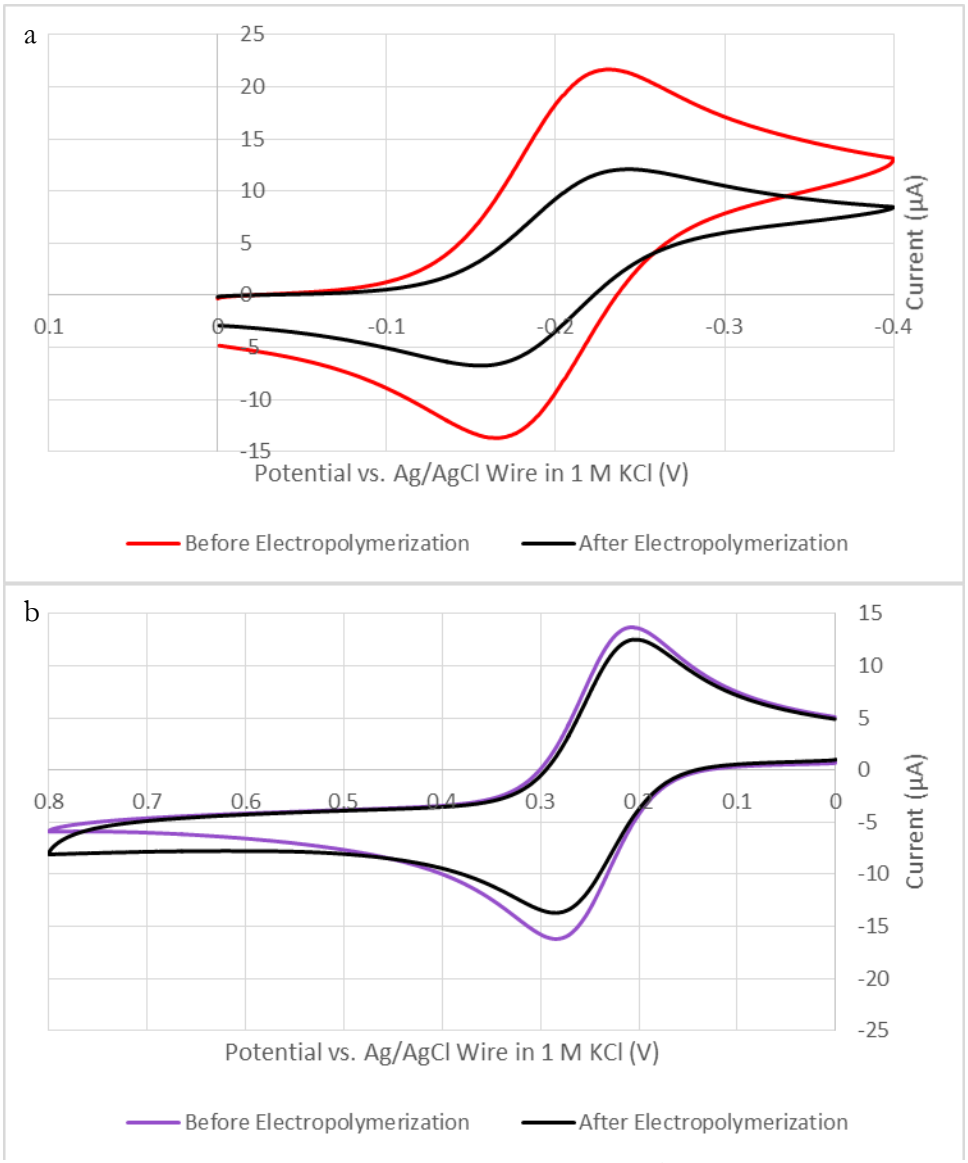

Figure 2.34: (a) Cyclic voltammogram of $Ru(NH_3)_6^{3+/2+}$ before and after reductive electropolymerization of 4-vinylaniline in 0.1 M $TBAPF_6$ in DMF at a 1.5 mm glassy carbon electrode. (b) Cyclic voltammogram of $Fe(CN)_6^{4-/3-}$ before and after reductive electropolymerization of 4-vinylaniline in 1 M KCl at a 1.5 mm glassy carbon electrode.

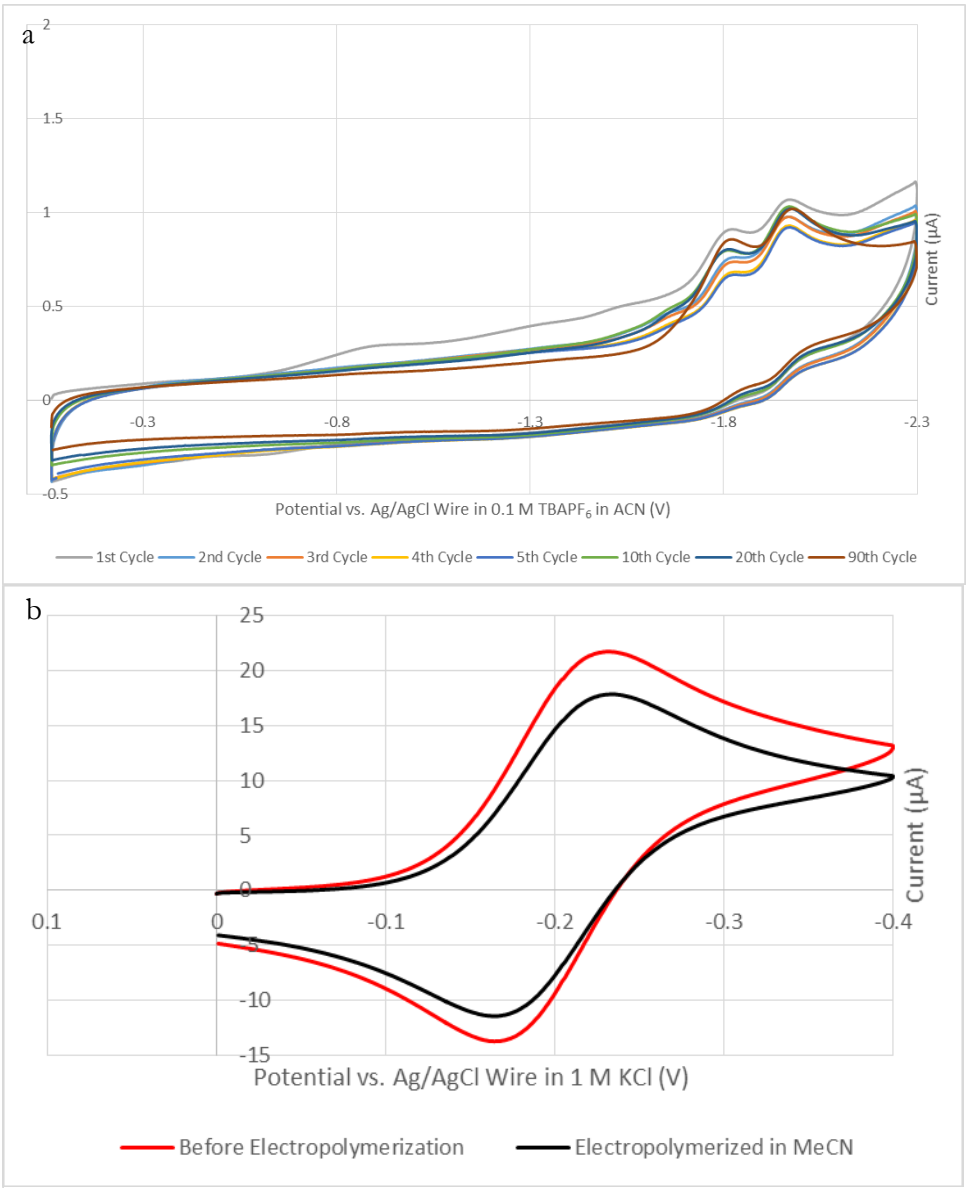

Figure 2.35: (a) Stepwise cyclic voltammogram of 4-vinylaniline in 0.1 M $TBAPF_6$ in ACN at a 1.5 mm glassy carbon electrode. This figure shows all 87 cycles. (b) Cyclic voltammogram of $Ru(NH_3)_6^{3+/2+}$ before and after oxidative electropolymerization of 4-vinylaniline in 0.1 M $TBAPF_6$ in ACN at a 1.5 mm glassy carbon electrode.

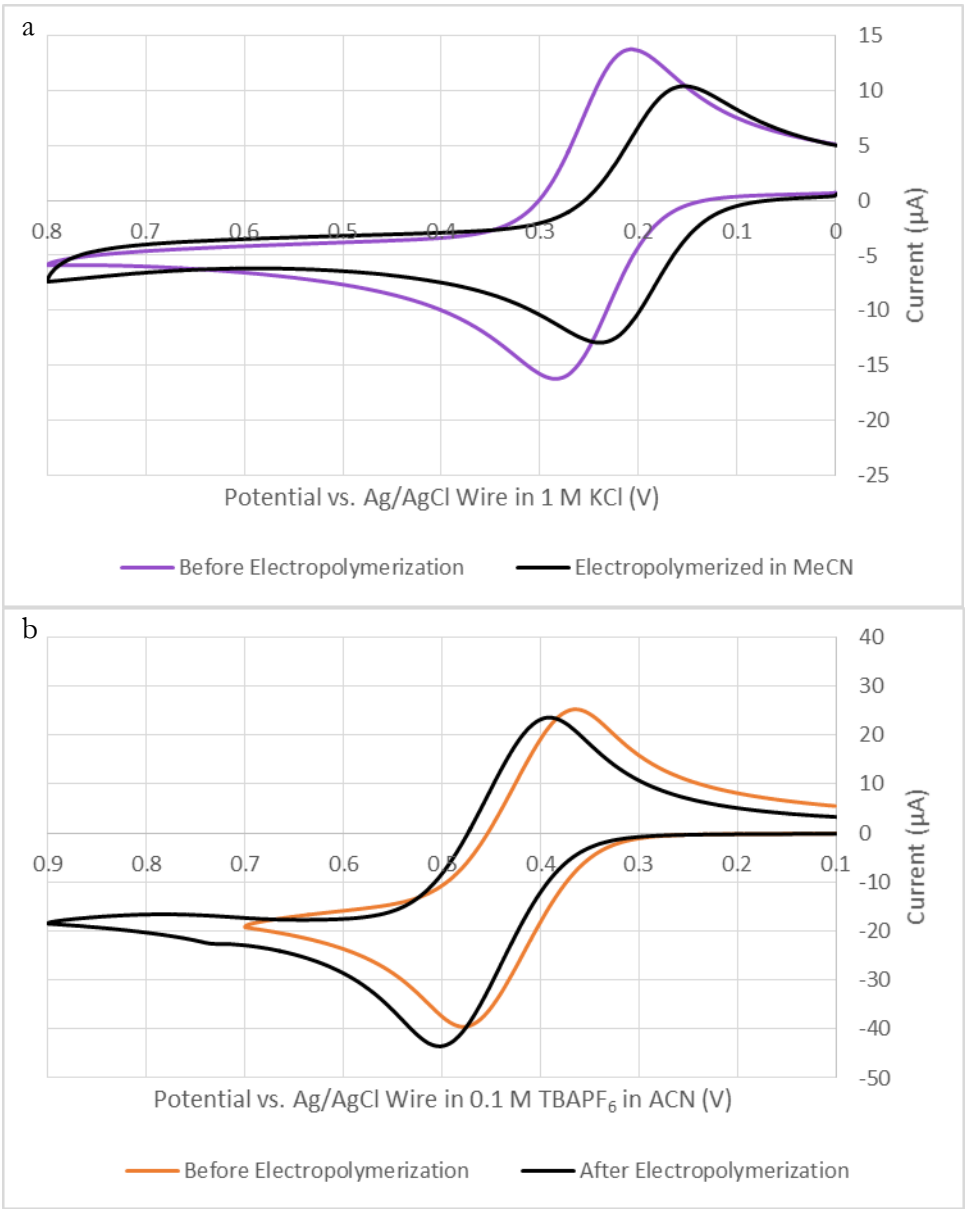

Figure 2.36: (a) Cyclic voltammogram of $Fe(CN)_6^{4-/3-}$ before and after oxidative electropolymerization of 4-vinylaniline in 0.1 M $TBAPF_6$ in ACN at a 1.5 mm glassy carbon electrode. (b) Cyclic voltammogram of $Fc^{0/+}$ before and after oxidative electropolymerization of 4-vinylphenol in 0.1 M in ACN at a 1.5 mm glassy carbon electrode.

Phloroglucinol

A wide variety of phloroglucinol solutions listed in Table 2.2 were prepared; however, the results shown herein will focus on the 50 mM phloroglucinol in 1 M KCl solution. The electropolymerization cyclic voltammogram, given in Figure 2.37, shows a sharp anodic peak at 0.807 V vs. Ag/AgCl reference wire. Like many other oxidative electropolymerizations, the second and subsequent cycles show near complete passivation of the electrode. Pinhole tests with $Fc^{0/+}$ and $Fe(CN)_6^{4-/3-}$ show complete passivation (a small > 1 μA cathodic current is seen past 0.2 V. This peak is shifted far positive). Cyclic voltammograms of these pinhole agents are shown in Figure 2.38. However, the $Ru(NH_3)_6^{3+/2+}$ cyclic voltammogram after electropolymerization, shown in Figure 2.37b appears the same as before electropolymerization. This information informed me that the phloroglucinol film may be acting as a cation exchange membrane.

I then prepared a 0.1 mM tris(2, 2'-bipyridyl)osmium(III) hexafluorophosphate in 0.1 M KCl solution ($Os(bpy)^{3+/2+}$). The cyclic voltammogram of $Os(bpy)^{3+/2+}$ at a bare glassy carbon electrode is shown in Figure 2.39; note the oxidation peak at 0.623 V and reduction peak at 0.536 V, both vs. Ag/AgCl reference wire. Figure 39 also shows the cyclic voltammogram of $Os(bpy)^{3+/2+}$ after phloroglucinol electropolymerization. At first, no peaks are visible. Then, the peaks shifted negative after the electropolymerized electrode soaked in the solution overnight: oxidation peak at 0.601 V and the reduction peak at 0.488 V, both vs. Ag/AgCl reference wire. Furthermore, soaking the electrode in 0.1 M KCl did not release the $Os(bpy)^{3+/2+}$ from the polymer film.

Figure 2.40a shows how the phloroglucinol film incorporates $Ru(NH_3)_6^{3+/2+}$ inside the film. At 100 mV/s, the $Ru(NH_3)_6^{3+/2+}$ cyclic voltammogram before and after electropolymerization appear the same. This result suggests $Ru(NH_3)_6^{3+/2+}$ exchanges quickly

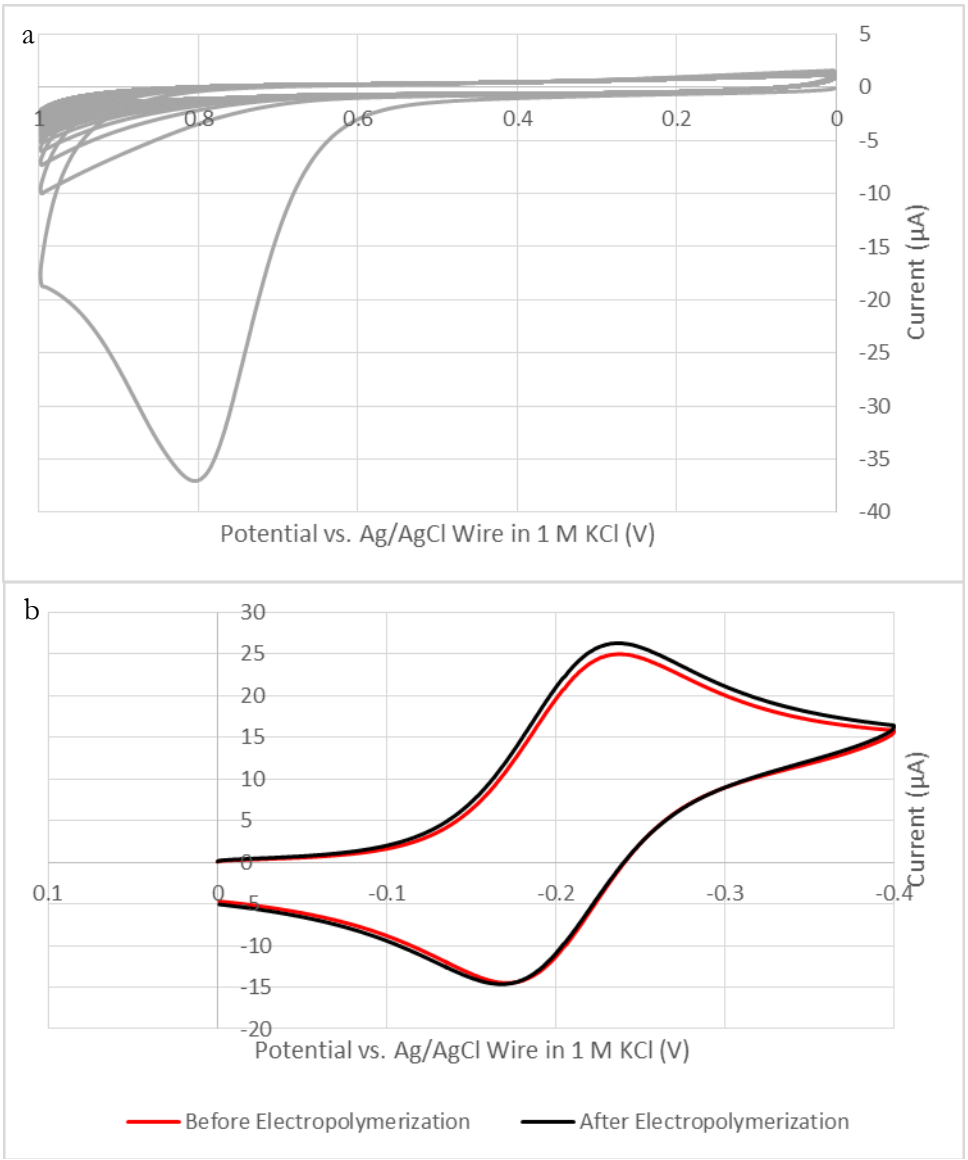

Figure 2.37: (a) Cyclic voltammogram of 50 mM phloroglucinol in 1 M KCl at a 1.5 mm glassy carbon electrode. (b) Cyclic voltammogram of $Ru(NH_3)_6^{3+/2+}$ before and after oxidative electropolymerization of phloroglucinol in 1 M KCl.

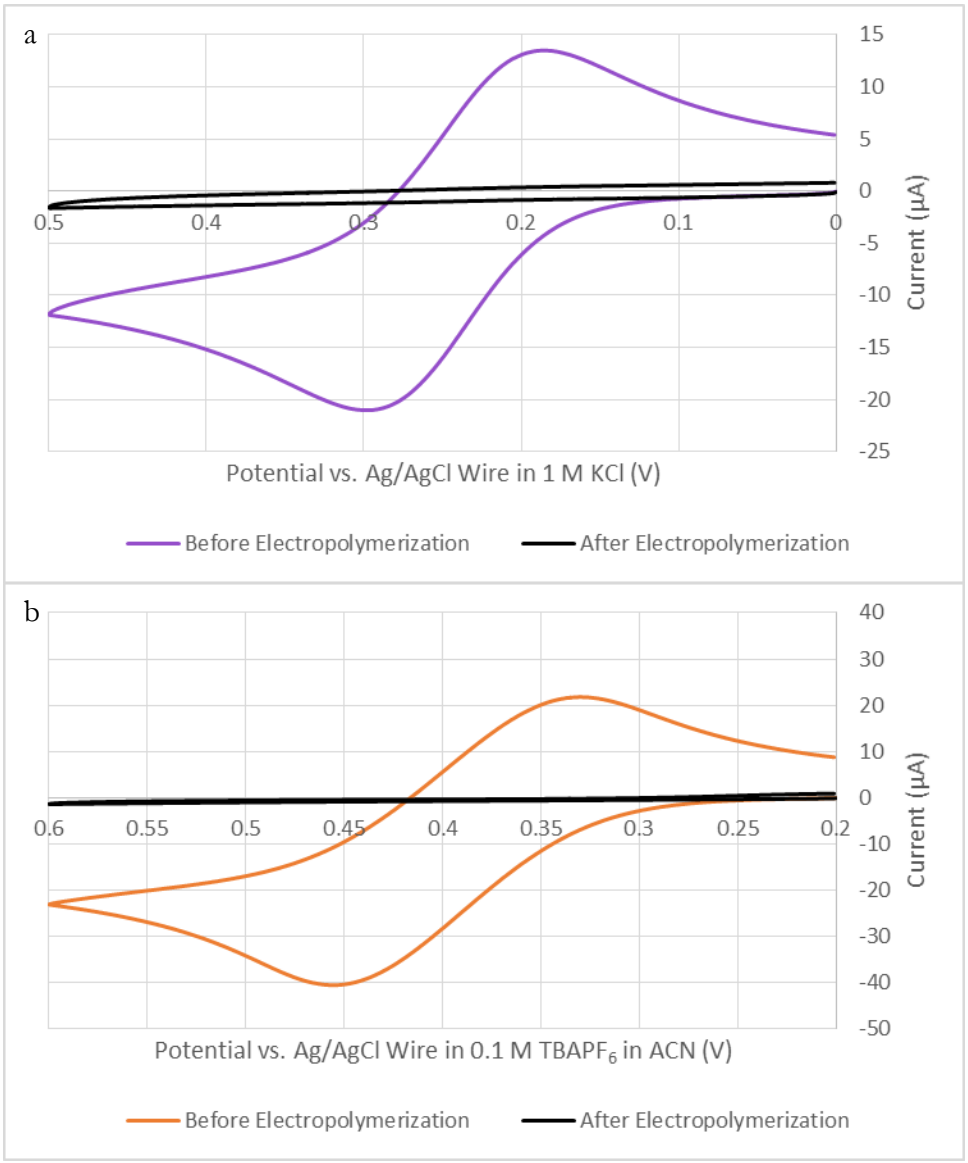

Figure 2.38: (a) Cyclic voltammogram of $Fe(CN)_6^{4-/3-}$ before and after oxidative electropolymerization of 50 mM phloroglucinol in 1 M KCl at a 1.5 mm glassy carbon electrode. (b) Cyclic voltammogram of $Fc^{0/+}$ before and after oxidative electropolymerization of 50 mM phloroglucinol 1 M KCl at a 1.5 mm glassy carbon electrode.

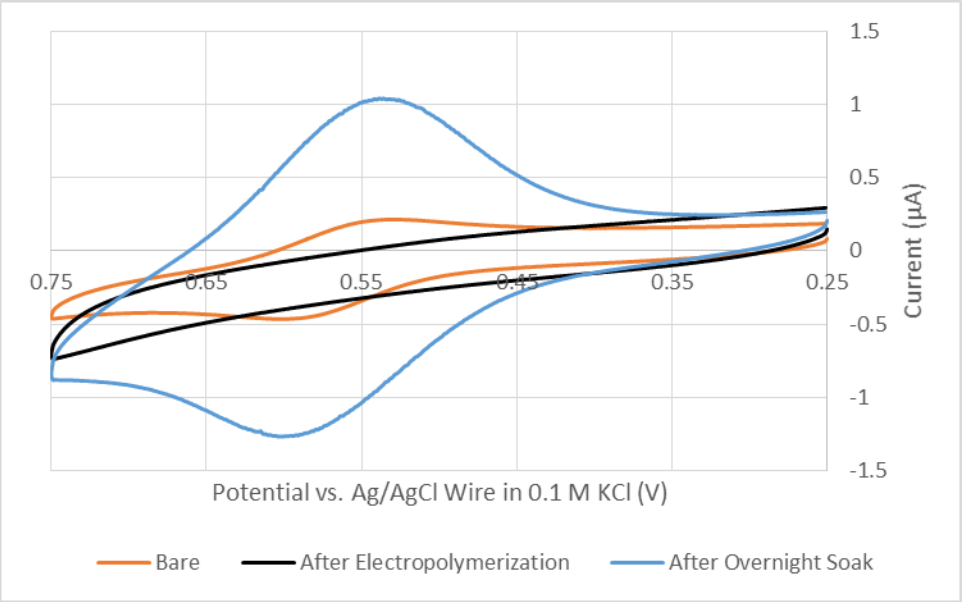

Figure 2.39: Cyclic voltammogram of $Os(bpy)^{3+/2+}$ before and after oxidative electropolymerization of 50 mM phloroglucinol in 0.1 M KCl at a 1.5 mm glassy carbon electrode. Immediately after electropolymerization, no current is observed at the electrode. However, after soaking the $Os(bpy)^{3+/2+}$ solution for about 24 hours, a massive current is observed.

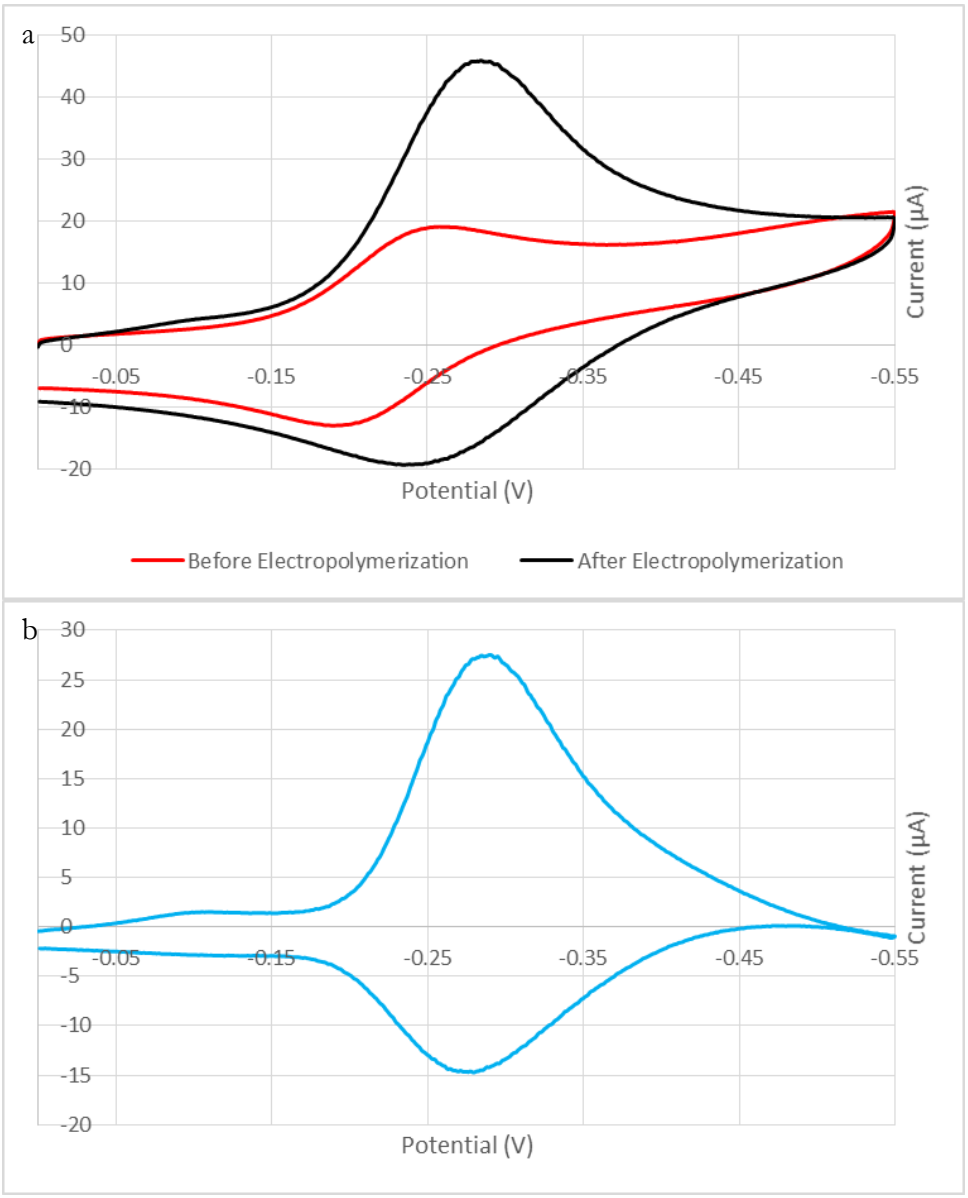

Figure 2.40: Cyclic voltammogram of $Ru(NH_3)_6^{3+/2+}$ before and after oxidative electropolymerization of phloroglucinol in 1 M KCl. The scan rate is 1 V/s. (b) Cyclic voltammogram of $Ru(NH_3)_6^{3+/2+}$ after subtraction of the above cyclic voltammograms. This is due to the $Ru(NH_3)_6^{3+/2+}$ inside the pores of the polymer. The anodic peak is smaller than the cathodic peak because of the fast diffusion of the $Ru(NH_3)_6^{3+/2+}$ into and out of the polymer film

between the phloroglucinol film and the solution. At 1000 mV/s, the effect of the film on $Ru(NH_3)_6^{3+/2+}$ can be seen. By subtracting the $Ru(NH_3)_6^{3+/2+}$ cyclic voltammogram before electropolymerization from the $Ru(NH_3)_6^{3+/2+}$ cyclic voltammogram after electropolymerization yields a surface wave, as shown in Figure 2.40b. This is possible because peak currents for an electroactive species adhered to the surface of an electrode increase linearly with scan rate, whereas peak currents for an electroactive species in solution increase with the square root of scan rate. This result shows $Ru(NH_3)_6^{3+/2+}$ spends a short amount of time incorporated in the polymer.

Figure 2.41a shows the massogram (the data collected from a quartz crystal microbalance) of an electropolymerization of 1 mM phloroglucinol in 1 M KCl at the surface of CVD graphene/Pt/Cr/AT-cut 5 MHz quartz crystal microbalance (QCM) electrode. The large shifts in frequency are due to the start and stop of the cyclic voltammogram. The saw tooth wave is indicative of the electropolymerization and adherence of the phloroglucinol film. Furthermore, the saw tooth wave reveals that not all electropolymerized phloroglucinol adheres to the surface of the CVD graphene.

The frequency shifts are related to the change in mass by the Sauerbrey equation,

$$\Delta f = -C_f \cdot \Delta m$$

where Δf is the observed frequency shift, Δm is the change in mass per unit area, and C_f is the sensitivity factor, taken as 56.6 $\frac{Hz \cdot cm^2}{\mu g}$ for a 5 MHz quartz crystal. The exposed area of the electrode is about 1.37 cm^2, whereas the area that oscillates is about 0.40 cm^2 on a 1 inch diameter by 331 μm thick quartz crystal.[66] From the area and assuming the density of the film is the density of phloroglucinol, which is 1.488 g / mL the thickness of the film was calculated to be 7.0 nm. On Cr/Pt fingers, 50 cycles of electropolymerization with a 1 mM phloroglucinol solution in 0.1 M KCl resulted in a thickness of 13.7 ± 1.1 nm.

The decrease in frequency corresponds to about 3.306 nmol, whereas integration of the cyclic voltammogram (Figure 2.41b) corresponds to about 420.4 nmol; the electropolymerization process has an efficiency of about 0.78 %. Do note that this is an underestimation, since the nonfaradaic background current was not subtracted from the cyclic voltammogram. The efficiency is likely to be higher with the background charging current subtracted.

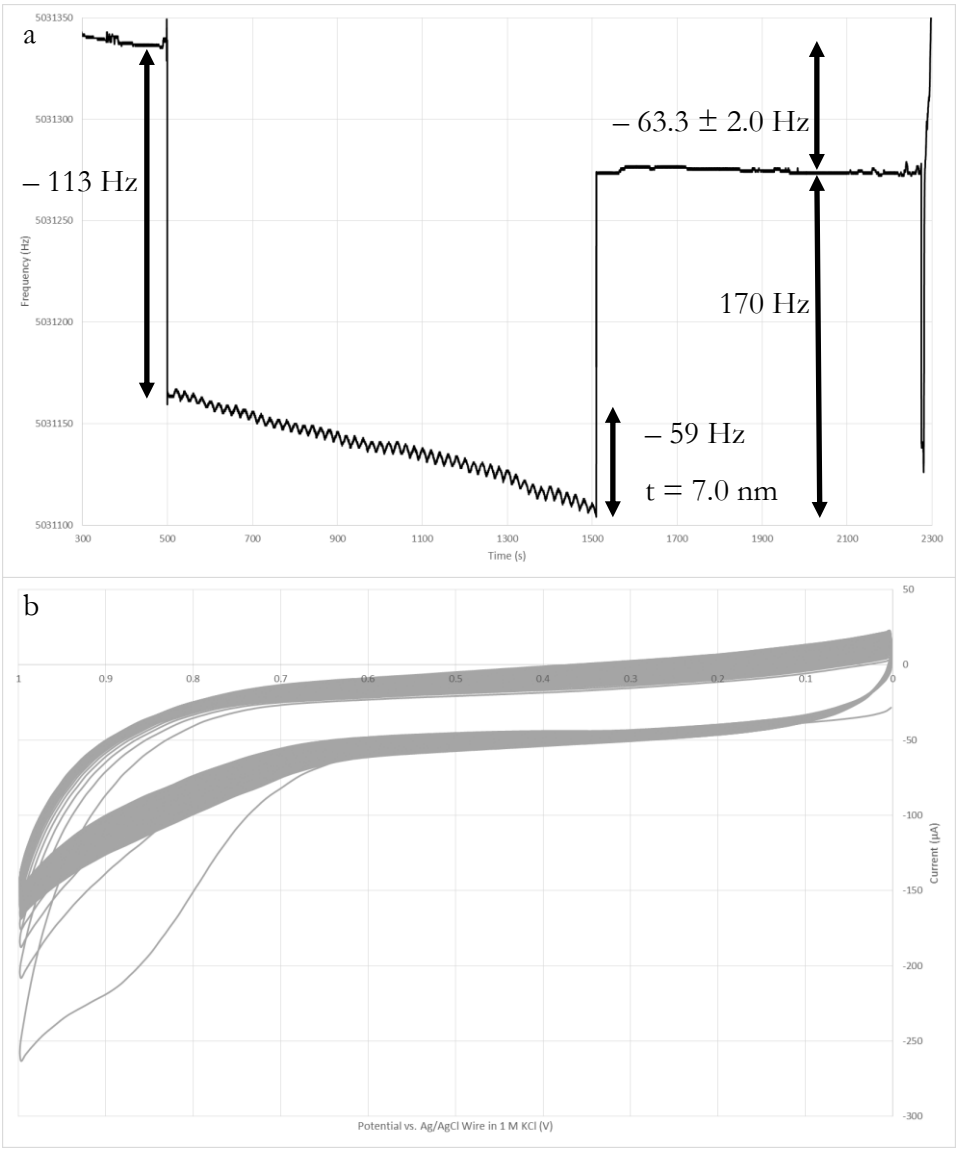

Figure 2.41: (a) Massogram of the electropolymerization of phloroglucinol. The saw tooth function represents the electropolymerization cycles of phloroglucinol on a CVD graphene/Pt/Cr/At-cut 5 MHz QCM. (b) Cyclic voltammogram of 1 mM phloroglucinol in 1 M KCl at of CVD graphene on Cr/Pt 5 MHz quartz crystal.

Conclusion

None of the polymers investigated passivate an electrodes better than the electropolymerization of phenol in sulfuric acid solution. Most of the electropolymerization were oxidative. However, this may not be useful if the substrates are easily oxidized. Reductive electropolymerization was investigated as a remedy. While electropolymerization was possible, the polymers formed were not pinhole-free. Finally, phloroglucinol polymer, and its structural analogue, pyrogallol polymer, exhibit interesting cation-exchange properties. In the phloroglucinol polymer, uptake of $Ru(NH_3)_6^{3+/2+}$ and $Os(bpy)^{3+/2+}$ and concentration of $Os(bpy)^{3+/2+}$ was demonstrated. Further experiments demonstrate the exchange of $Ru(NH_3)^{3+/2+}$ into and out of the polymer is very fast compared to the timescale of the experiment. At fast scan rates, incorporation of $Ru(NH_3)_6^{3+/2+}$ in the polymer film was observed. This cation-exchange property suggests the presence of oxide anions, which may be useful for initiating atomic layer deposition of aluminum oxide (Al_2O_3).

Table 2.2: Experimental Solutions	
4-Chlorophenol[36, 37, 38, 39]	0.5 M sodium sulfate, adjusted to pH 2 with dilute H_2SO_4
	1 M NaOH
	1 M KCl
4-Fluorophenol	0.1 M $TBAPF_6$ in DMF
	1 M KCl
	0.1 M NaOH
1-Naphthol[40, 41, 42, 43, 44]	0.1 M NaOH
8-Hydroxyquinoline[45]	0.08 M sodium chloride in 10% (v/v) ethanol
Tris(8-hydroxyquinoline) aluminum	0.1 M $TBAPF_6$ in ACN
Phenol[27, 43, 46, 50, 56, 57]	0.1 M $TBAClO_4$, 0.05 M TMAOH, 0.005 M $Fc^{0/+}$ in ACN
	1 M KCl
	0.1 M $TBAClO_4$ in ACN
	0.1 M $TBAClO_4$, 0.05 M TMAOH in ACN
	0.1 M $TBAPF_6$ in ACN
Furfural[47, 48]	0.1 M $TBAPF_6$ in ACN
Pyrogallol[49]	0.2 M phosphate buffer, pH 5.0
4-Vinylaniline	0.1 M $TBAPF_6$ in DMF
	0.1 M $TBAPF_6$ in ACN
4-Cyanophenol	0.1 M $TBAPF_6$ in ACN
	0.1 M $TBAPF_6$ and TMAOH in ACN
4-Vinylphenol[55, 57, 58]	0.1 M $TBAPF_6$ in ACN
	0.1 M $TBAPF_6$ in DMF
	1 M KCl
	0.1 M NaOH
Benzonitrile[53, 54]	0.1 M $TBAPF_6$ in itself
	0.1 M $TBAPF_6$ in tetrahydrofuran
3-Nitrophenol[55, 57, 58]	0.1 M NaOH
	0.1 M $TBAPF_6$ and 0.1 M TMAOH in ACN
	0.1 M $TBAPF_6$ in ACN
	1 M KCl
4-Nitrophenol[57, 58]	0.1 M NaOH
2-Aminophenol[59, 60, 61]	0.5 M H_2SO_4
	1 M KCl
	0.1 M NaOH
	0.1 M $TBAPF_6$ in ACN
	0.1 M $TBAPF_6$ and 0.1 M TMAOH in ACN
Salicylic Acid[62]	0.33 M formaldehyde in 0.25 M NaOH
Phloroglucinol[49, 63, 64, 65]	0.5 M H_2SO_4
	1 M KCl
	1 M NaOH
	0.2 M phosphate buffer, pH 5.0
	0.005 M $Fe(CN)_6^{4-/3-}$ in 0.2 M phosphate buffer, pH 5.0

CHAPTER 3: ELECTROPOLYMERIZATION ONTO GRAPHENE DEVICES

As discussed in the previous chapter, the polymer film derived from electropolymerizing phloroglucinol behaved as a cation-exchange film. From the experiments above, it was hypothesized that the phloroglucinol polymer has unreacted hydroxide groups. Below, it will be shown that the polymer does not affect the structure of graphene. Because of these two properties—strong noncovalent interaction between the polymer and graphene and free hydroxide groups on the polymer—I was able to demonstrate that the polymer can be used as a seed layer for metal oxide deposition.

Metal oxide deposition via atomic layer deposition (ALD) typically occurs via two steps.[67, 68, 69] First, the surface to upon which to be deposited is saturated with a monolayer of non-metal precursor, such as water (for the deposition described herein), ammonia, or hydrogen sulfide. After a purging interval to remove any excess non-metal precursor, the metal precursor is introduced; the metal precursor can be tetrakis(dimethylamino)hafnium (IV), tri(dimethylamino)aluminum (III) (for the deposition described herein), $AlCl_3$, or TiI_4. The metal precursor reacts completely with the non-metal precursor, resulting in a metal oxide and gaseous byproducts. The chemical equation for this reaction using the chemicals described above is: $2\ Al((CH_3)_2N)_3\ (g) + 3\ H_2O\ (adsorbed) \rightarrow Al_2O_3\ (s) + 6\ (CH_3)_2NH\ (g)$. The deposition chamber is purged again before reintroducing the non-metal precursor, and the cycle continues until the desired thickness is reached. Figure 3.1 illustrates this and the metal oxide deposition procedure at a CVD graphene device after electropolymerization of phloroglucinol. With the phloroglucinol polymer, the first step non-metal precursor step will be omitted, since the polymer is believed to contain unreacted hydroxyl groups.

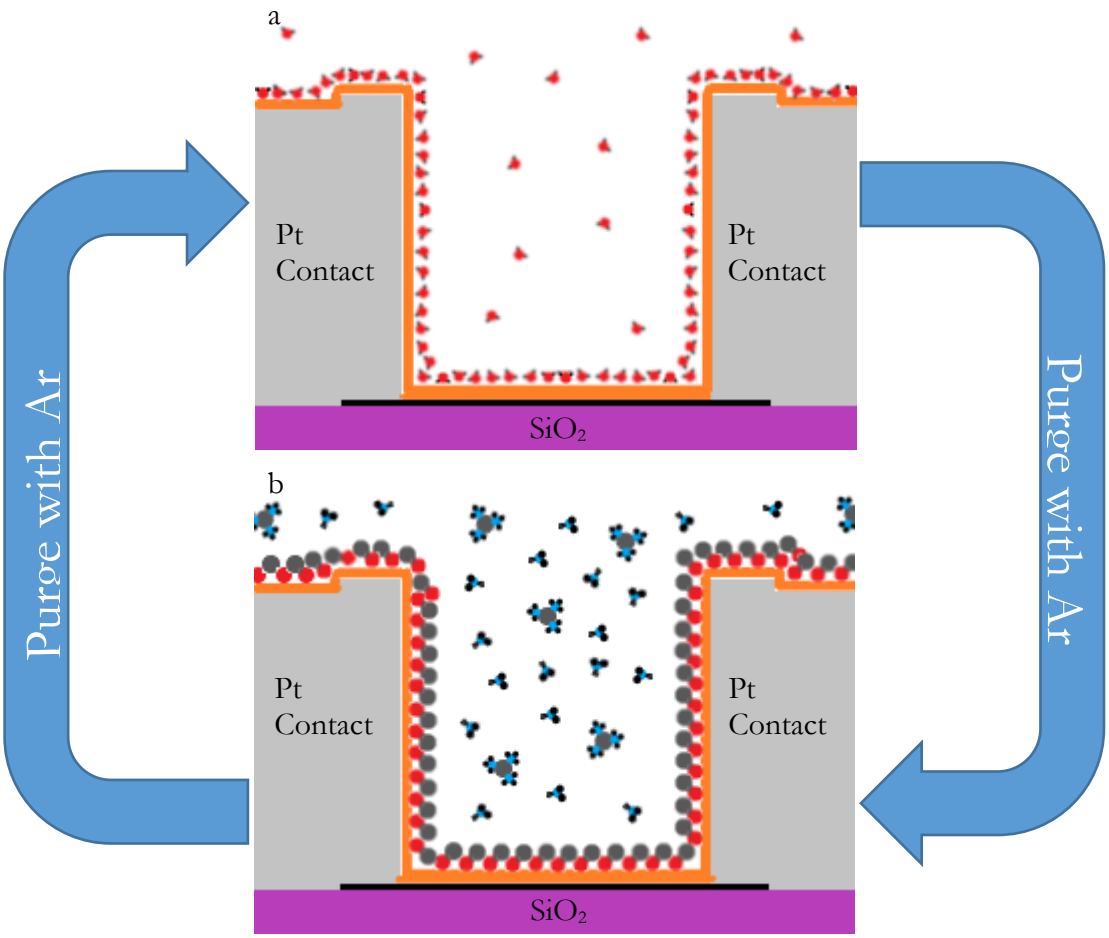

Figure 3.1: A cartoon describing the ALD process at a CVD graphene (black) device after electropolymerization in phloroglucinol (orange). A) Nonmetal precursor is injected into the ALD chamber, in this case water. The nonmetal precursor is allowed to fully saturate the surface. B) Metal precursor is injected into the chamber, in this case tri(dimethylamino)aluminum (III) , after a purge of Ar to remove excess water. The metal precursor reacts with the water to form Al_2O_3. The cycle repeats after another purge of Ar.

Experimental

Phloroglucinol and KCl were used as received without further purification. 0.5 mM phloroglucinol in 1 M KCl was prepared via dilution from 5 mM phloroglucinol in 1 M KCl. Experimental electrochemical parameters are given in Table 3.3. These parameters produced films that are about 1 nm thick as measured via AFM. The cell used is shown in Figure 3.2: the working electrodes were devices fabricated from either exfoliated or CVD graphene; the reference electrode was a homemade Ag/AgCl reference wire; and the counter electrode was a platinum wire or mesh. Devices ready for electropolymerization were ultrasonically welded to gold pads using a West Bond 7476E Manual Wedge Bonder with 1 μm diameter gold wire. The power used was between 275 and 450, and the time per weld was around between 450 and 550 ms. Because of the uneven surface of the gold pads, the power and time needed for a successful bond varied.

Fabrication of Exfoliated Graphene Devices

Mechanically exfoliated graphene was prepared by the Scotch tape method (shown in Figure 3.3) onto silicon wafers with and 300 nm thermally grown silicon dioxide. Markers (10 μm × 50 μm crosses), device electrodes, and top gates were patterned using a Zeiss Supra 40 Field-Emission Scanning Electron Microscope and a Raith Pattern Generator. Device patterns were generated using ELPHY Quantum software. General conditions are given in Table 3.4. The appendix contains useful information about operating the instrument. After exposure, the wafers were developed in 1:3 methylisobutyl ketone:isopropanol (MIBK) for 40 seconds, then rinsed in isopropanol (IPA), and dried with nitrogen gas.

Electron beam evaporation (EBE) and direct current magnetron sputtering were used to deposit metals. EBE was performed with an AJA E-beam Evaporator. Sputtering

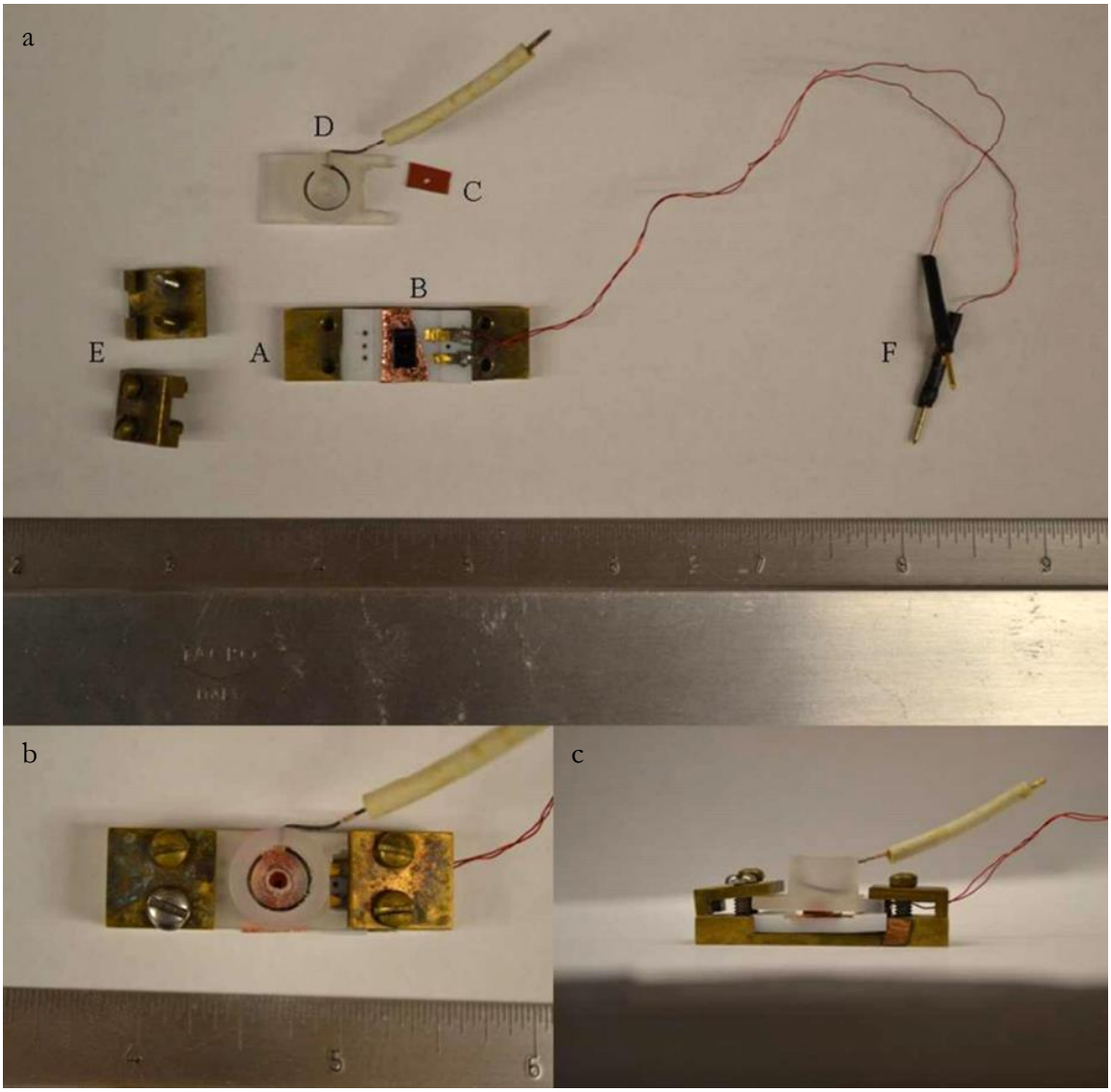

Figure 3.2: Electrochemical cell for electropolymerization of devices. A: Base of cell. B: Copper tape used to secure silicon wafer. C: Silicone gasket. D: Plastic top with integrated counter electrode (the integrated counter electrode was not used during any electropolymerization). E: Screw clamps. F: Leads from the gold pads. (b) Top view of assembled electrochemical cell (c) Side view of assembled electrochemical cell.

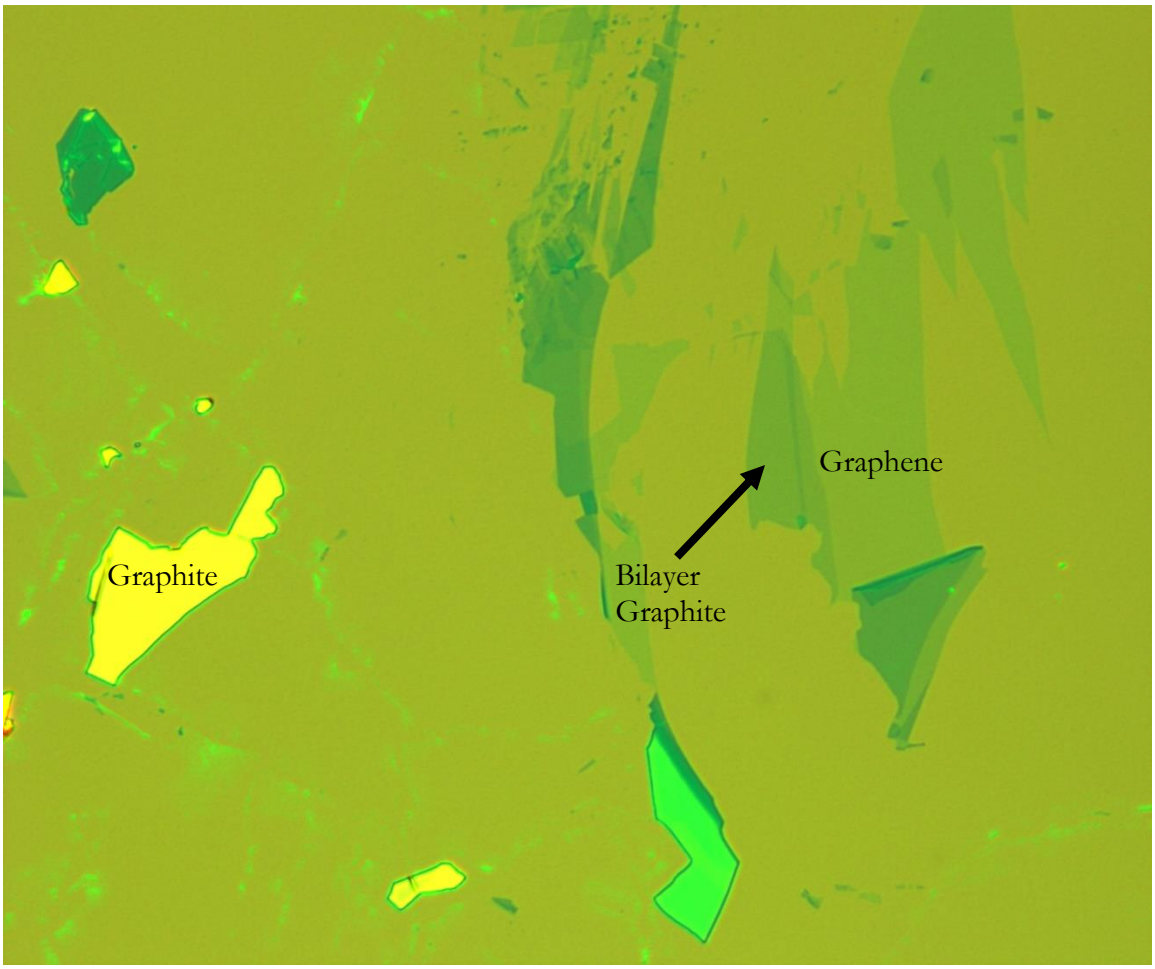

Figure 3.3: An optical image at 50X magnification. Graphene and multilayer graphite can be seen in the image. The green tint is due to the white balance setting in the microscope's software.

was performed with a Mantis Deposition Inc. Hex Deposition system. ~4.2 nm titanium (Ti) adhesion layer and ~14.8 nm Au were evaporated onto the developed wafers to make the crosses and top gates. ~4.2 nm Ti adhesion layer and ~14.8 nm Pt were evaporated onto the developed wafers to make the contact electrodes. Sometimes, ~5 nm chromium (Cr) adhesion layer and ~15 nm Pt were sputtered onto the developed wafers to make the contact electrodes. I deposited Pt instead of Au for contact, because prior experiments showed delamination of Au during phloroglucinol electropolymerization. Tables 3.5 and 3.6 list the parameters used for EBE and sputtering, respectively. No heating of the substrate was performed during both EBE and sputtering. The substrate holder was rotated at about 15 rpm.

Lift-off was performed after metal evaporation or sputtering by exposure to semiconductor grade acetone. Then the wafer was rinsed with isopropanol and dried with nitrogen gas. The steps for fabrication of these devices are listed below:

1. Locate single layer graphene using and optical microscope.
2. Spin coat PMMA-A4 (4% Poly(methylmethacrylate) (PMMA) in anisole) onto wafer at 3000 rpm for 45 seconds.
3. Bake on hot plate at 180 °C for 90 seconds.
4. Expose marker pattern via EBL.
5. Develop patterns using MIBK:IPA for 40 seconds, which removed exposed PMMA.
6. Evaporate Ti and Au onto wafer.
7. Lift off by using acetone to dissolve PMMA and remove deposited metals on top of PMMA.
8. Rinse with isopropanol, then dry using compressed nitrogen.

9. Map wafer to markers and locate single layer graphene using SEM.
10. Spin coat PMMA-A4 (4% PMMA in anisole) onto wafer at 3000 rpm for 45 seconds.
11. Bake on hot plate at 180 °C for 90 seconds.
12. Expose device patterns via EBL.
13. Develop patterns using MIBK:IPA for 40 seconds, which removed exposed PMMA.
14. Evaporate Ti and Pt or sputter Cr and Pt onto wafer.
15. Lift off by using acetone to dissolve PMMA and remove deposited metals on top of PMMA.
16. Rinse with isopropanol, then dry using compressed nitrogen.

Fabrication of CVD Graphene Devices

Preparing devices from exfoliated graphene was time consuming, so I switched to using CVD graphene. The CVD graphene was grown by Dr. Alexey Lipatov in Dr. Sinitskii's group as described in reference 70.

The device patterns, development, and metal deposition procedures are the same as for the fabrication of exfoliated graphene devices. Lift off was performed by exposing the wafer to acetone without sonication. Sonication was shown to delaminate Cr/Pt and Ti/Pt contacts deposited on graphene.

Reactive ion etching was performed in a Trion Minilock-Phantom III Reactive Ion Etching System. The etching gas was oxygen. The pressure was 50 mTorr. The flow rate of oxygen was 50 sccm. The inductively coupled plasma (ICP) power and RIE power was 100 W and 50 W, respectively.

The steps for fabrication of these devices are listed below:

1. Locate CVD graphene in optical microscope and SEM.
2. Spin coat PMMA-A4 (4% PMMA in anisole) onto wafer at 3000 rpm for 45 seconds.
3. Bake on hot plate at 180 ºC for 90 seconds.
4. Expose marker pattern via EBL.
5. Develop pattern with MIBK:IPA for 40 seconds, which removes exposed PMMA.
6. Evaporate Ti and Au onto wafer.
7. Lift off by using acetone to dissolve PMMA and remove deposited metals on top of PMMA.
8. Rinse with isopropanol, then dry using compressed nitrogen.

9. Map CVD graphene to fiduciary markers and locate CVD graphene using SEM.
10. Spin coat PMMA-A4 (4% PMMA in anisole) onto wafer at 3000 rpm for 45 seconds.
11. Bake on hot plate at 180 ºC for 90 seconds.
12. Expose etching pattern via EBL.
13. Develop pattern with MIBK:IPA for 40 seconds, which removes exposed PMMA.
14. Remove CVD graphene from exposed areas using RIE.
15. Lift off by using acetone to dissolve PMMA, leaving small rectangular patches of CVD graphene.
16. Rinse with isopropanol, then dry using compressed nitrogen.

17. Map rectangular patches of CVD graphene to fiduciary markers.
18. Spin coat PMMA-A4 (4% PMMA in anisole) onto wafer at 3000 rpm for 45 seconds.
19. Bake on hot plate at 180 °C for 90 seconds.
20. Expose PMMA to create device pattern via EBL.
21. Develop pattern with MIBK:IPA for 40 seconds, which removes exposed PMMA.
22. Evaporate Ti and Pt or sputter Cr and Pt onto wafer.
23. Lift off by using acetone to dissolve PMMA and remove deposited metals on top of PMMA.
24. Rinse with isopropanol, then dry using compressed nitrogen.

25. Map CVD graphene devices to fiduciary markers.
26. Spin coat PMMA-A4 (4% PMMA in anisole) onto wafer at 3000 rpm for 45 seconds.
27. Bake on hot plate at 180 °C for 90 seconds.
28. Expose portions of graphene and contacts for electropolymerization.
29. Develop pattern with MIBK:IPA for 40 seconds, which removes exposed PMMA.
30. Electropolymerize 5 mM phloroglucinol in 0.1 M KCl for 50 cycles.
31. Lift off by using acetone to dissolve PMMA and remove deposited metals on top of PMMA.
32. Rinse with isopropanol, then dry using compressed nitrogen.

Tetrakis(dimethylamino)hafnium and was used as received without further purification. ~3 nm HfO_2 was deposited by Dr. Peter Wilson, and Derek Sekora in Dr. Mathias Shubert's group. Then, tri(methylamino)aluminum (TMA) was used as received without further purification. Ufuk Kilic in Dr. Mathias Shubert's group deposited ~3 nm Al_2O_3 and later, ~7 nm. The conditions for depositing Al_2O_3 is given in Table 3.7, which is located at the end of the chapter. The instrument for ALD is the Cambridge Nanotech Fiji 100 with in situ J. A. Woollam Co., Inc. ellipsometer.

Ellipsometry was performed with a J. A. Woollam Co., Inc. M–2000S with an EC–400 main power supply at a beam angle of 6.9° and a spot size of 1.5 cm × 0.5 cm. The light source had a spectrum of 275.7 – 729.4 nm. Complete EASE is the software used for ellipsometric data collection and modeling. All models used for ALD deposition were empirically designed, except for the phloroglucinol layer, which was modelled as a Cauchy distribution with a thickness of about one (1) nm. Ellipsometry was not performed during the ALD of Al_2O_3 onto CVD devices, due to the devices being too small (note the beam size). Continued steps of fabrication are shown below:

33. ALD of Al_2O_3 onto wafer.
    a. 0.06 s H_2O pulse
    b. 15 s wait
    c. 0.06 s TMA pulse
    d. 15 s wait
    e. Repeat for 45 cycles (growth rate is about 0.07 nm per cycle)

Fabrication of a top gate involved exposing the top gate pattern, and evaporating Ti and Au. Continued steps of fabrication are shown below.

34. Map CVD graphene devices to fiduciary marks using SEM.
35. Spin coat PMMA-A4 (4% PMMA in anisole) onto wafer at 3000 rpm for 45 seconds.
36. Bake on hot plate at 180 °C for 90 seconds.
37. Expose pattern for top gate electrodes.
38. Develop pattern with MIBK:IPA for 40 seconds, which removes exposed PMMA.
39. Evaporate Ti and Au onto wafer.
40. Lift off by using acetone to dissolve PMMA and remove deposited metals on top of PMMA.
41. Rinse with isopropanol, then dry using compressed nitrogen.

Conductivity measurements were performed by Alexey and myself using a Lakeshore TTPX probe station with an Agilent 4155C Semiconductor Parameter Analyzer. The parameters for bottom gate measurements and top gate measurements are given in Table 8a and 8b.

Later, top gates were fabricated using a 1:1 vol solution of PEDOT:PSS (Poly(3,4-ethylenedioxythiophene):Polystyrene sulfonate) / IPA solution, typically prepared by mixing 10 drops of PEDOT:PSS with 10 drops of isopropanol. The PEDOT:PSS was branded as Clevios P from Heraeus. This procedure was modified from Ben Wymore's procedure, and an SOP from Tufts University.[71, 72] (The reference in the SOP is incorrect. The bibliography lists the correct reference).

Below is the procedure:

1. Spin coat PMMA-A4 (4% PMMA in anisole) onto wafer at 3000 rpm for 45 seconds.
2. Bake on hot plate at 180 °C for 90 seconds.
3. Repeat the above two steps. Experiments showed that single-layer lithography did not capture enough PEDOT:PSS.
4. Expose PMMA to create device pattern via EBL using the 60 μm aperture settings.
5. Develop pattern with MIBK:IPA for 40 seconds, which removes exposed PMMA.
6. Spin coat 1:1 vol solution of PEDOT:PSS / isopropanol at 5000 rpm for 45 seconds.
7. Bake on hot plate at 140 °C for five minutes.
8. Lift off by using acetone to dissolve PMMA, then sonicate in acetone for four seconds to remove excess PEDOT:PSS film.
9. Rinse with isopropanol, then dry using compressed nitrogen.

Removal of the PEDOT:PSS was achieved by sonicating the wafers in water for three seconds. However, some removal of the metal contacts were observed.

Device characteristics such as visible appearance, thickness, and conductivity and gateability were measured using the methods described below generally after each lift-off and electropolymerization step. These techniques were light microscopy, atomic force microscopy (AFM), and electrical measurements. To a lesser extent, measurements with a quartz crystal microbalance (QCM), and ellipsometry were also performed to understand the behavior of phloroglucinol on CVD graphene. The results of other techniques not shown

include electron dispersion spectroscopy (EDS), infrared spectroscopy (IR), and thermogravimetric analysis (TGA).

Investigation of how the ALD temperature influences the phloroglucinol polymer was performed on Ti/Pt QCM crystals. Measurement of the thickness of phloroglucinol polymer was gathered using ellipsometry, AFM, and QCM. Pinhole measurements with $Ru(NH_3)_6^{3+/2+}$ and $Fe(CN)_6^{4-/3-}$ were taken. QCM measurements were taken in air; the crystal was allowed to dry after being rinsed with ~18 MΩ·cm water. The crystal was isolated from air currents by being placed in a tall beaker with a cardboard cover. Ellipsometry was performed with a J. A. Woollam Co., Inc. ellipsometer. Data was collected at four different beam angles: 45°, 55°, 65°, and 75°. The data could not be modeled because of the thickness of the Ti/Pt. Thus, the raw data was used to draw conclusions. After each step—bare Ti/Pt QCM, electropolymerization of 5 mM phloroglucinol in 0.1 M KCl for 50 cycles, and annealing at 150 °C for 30 min (the normal time for ALD)—AFM, ellipsometry, and QCM measurements were taken.

Results

Figure 3.4 shows an image of the device constructed to test how the phloroglucinol polymer impacts graphene's chemical structure. A portion of CVD graphene was patterned and etched into a 200 μm square. The square was then surrounded by a 20 μm thick Ti/Pt ring, which itself was attached to a 300 μm Ti/Pt contact about 2000 μm away. The contact was connected to the Au pads on the electrochemical cell via ultrasonic wire bonding. After assembly into the electrochemical cell, I electropolymerized 0.5 mM phloroglucinol in 1 M KCl onto CVD graphene for 50 cycles. Raman spectra of the graphene before and after were recorded and are shown in Figure 3.5. Graphene's Raman spectrum[73] has four peaks

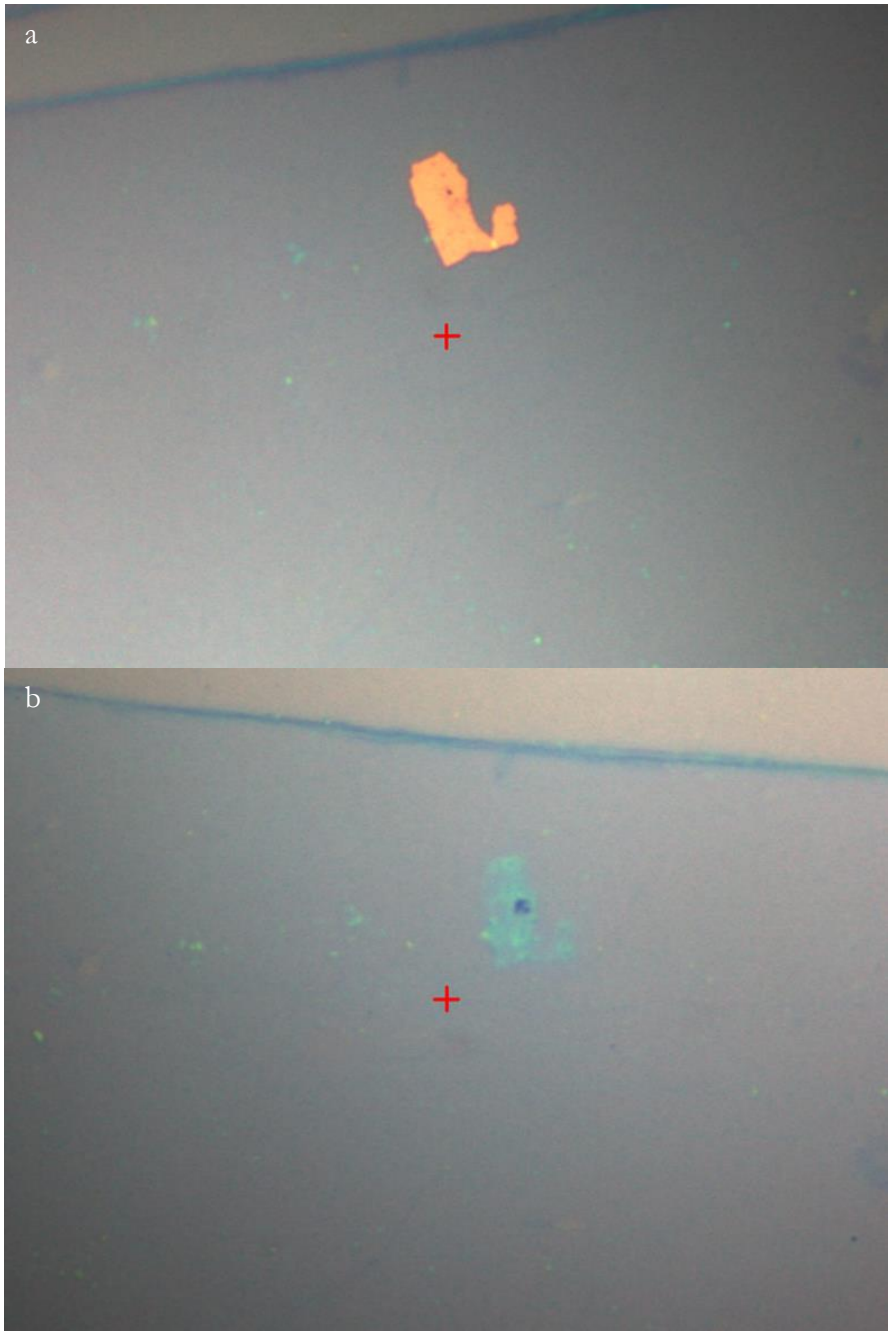

Figure 3.4: CVD graphene (a) before and (b) after electropolymerization of phloroglucinol at 10X.

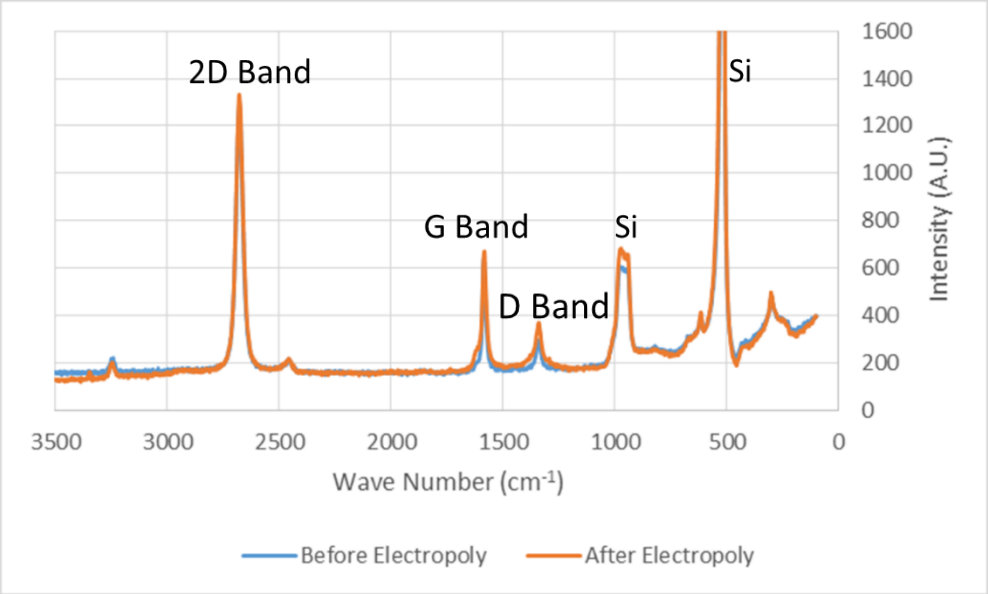

Figure 3.5: Raman spectra of CVD graphene before and after electropolymerization of phloroglucinol. As can be seen, the spectra are nearly identical, showing phloroglucinol electropolymerization does not affect the chemical structure of CVD graphene.

corresponding to various vibrational states: 1350 cm^{-1} (D band), 1580 cm^{-1} (G band), and 2680 cm^{-1} (2D band). The D band is related to disorder in the structure of graphene; this peak increases with chemical modification of graphene. First-order phonon resonance causes the G band, whereas second-order phonon resonance causes the 2D band. Graphene will inherently have disorder because of its edges, meaning a D band will always be present in the spectrum. A good rule of identifying pristine graphene is the 2D band should be at least twice the G band. As can be seen, electropolymerization of phloroglucinol onto graphene does not change the chemical structure of graphene, as seen by the near overlap of the two spectra; yet, the polymer passivates the graphene like in earlier cyclic voltammograms. Thus, the polymer adheres noncovalently to graphene, like the polymer derived from phenol.

The quality of the graphene was measured via Raman spectroscopy before lithography. The following results belong to two recent sets of devices fabricated in June and September 2018. The general dimensions of the pattern are given in Table 3.4. Figure 3.6 shows a 10X optical image of the devices. Figure 3.7 shows an example of the conductivity measurements. Most of the CVD graphene did not have Dirac points at 0 V, nor were the peaks sharp, as would be expected of exfoliated graphene. Sometimes, the devices had Dirac points outside of the gate voltage range measured, while others did not appear to have Dirac points at all[3]. Behavior of devices without Dirac points at all were ignored throughout the procedure. AFM images were collected of some devices throughout the procedure. Figure 3.8 shows typical AFM images of bare graphene devices immediately after metal deposition. The cleanliness of the surrounding area is dependent on the handling

[3] A device would not a Dirac point, if, for example, the graphene was damaged and could not make an electrical connection to the metal contacts.

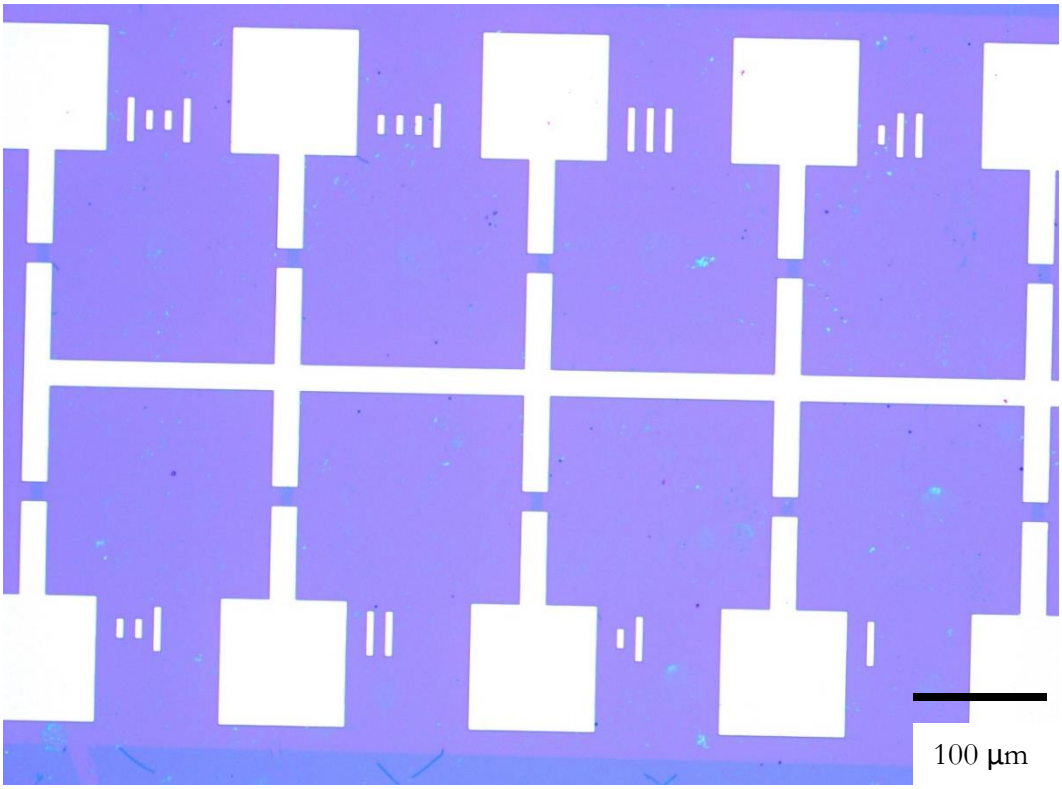

Figure 3.6: Optical image of devices created in June 2018 after lithography. Far to the right is the contact that will be ultrasonically wired bonded to the electrochemical cell's Au pads (not shown). The CVD graphene can barely be seen as the faint blue strip between the Pt fingers and surrounding the Pt contacts.

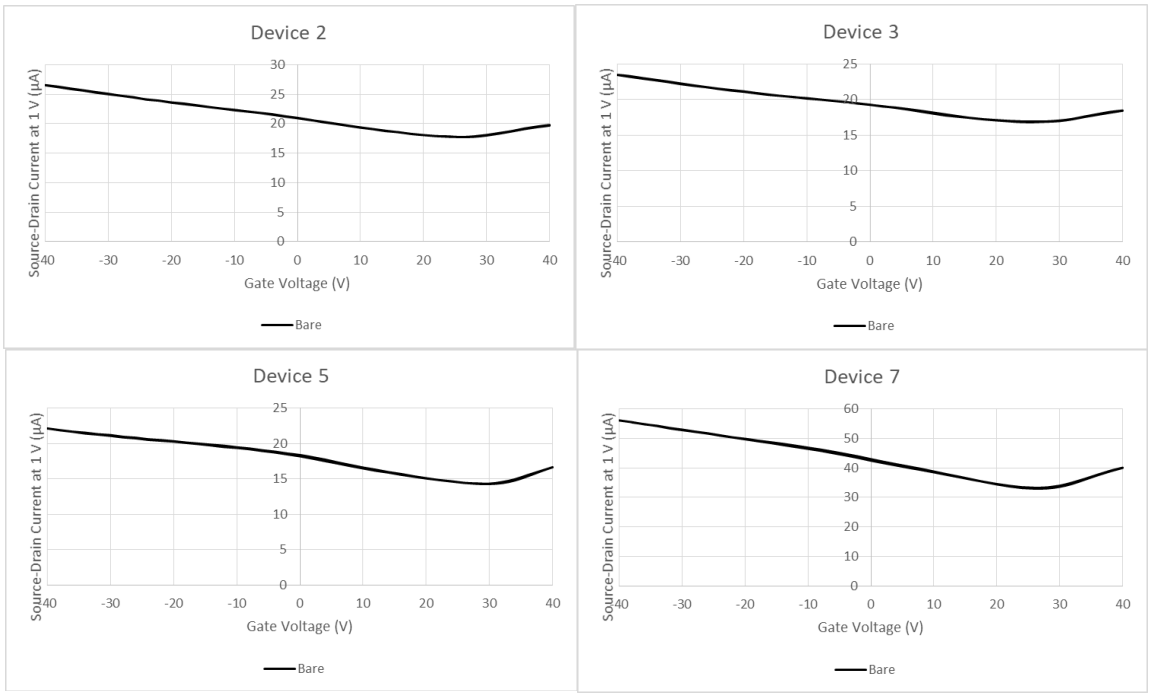

Figure 3.7: Conductivity measurements of Devices 2, 3, 5, and 7 created in June 2018. Note the different current scales.

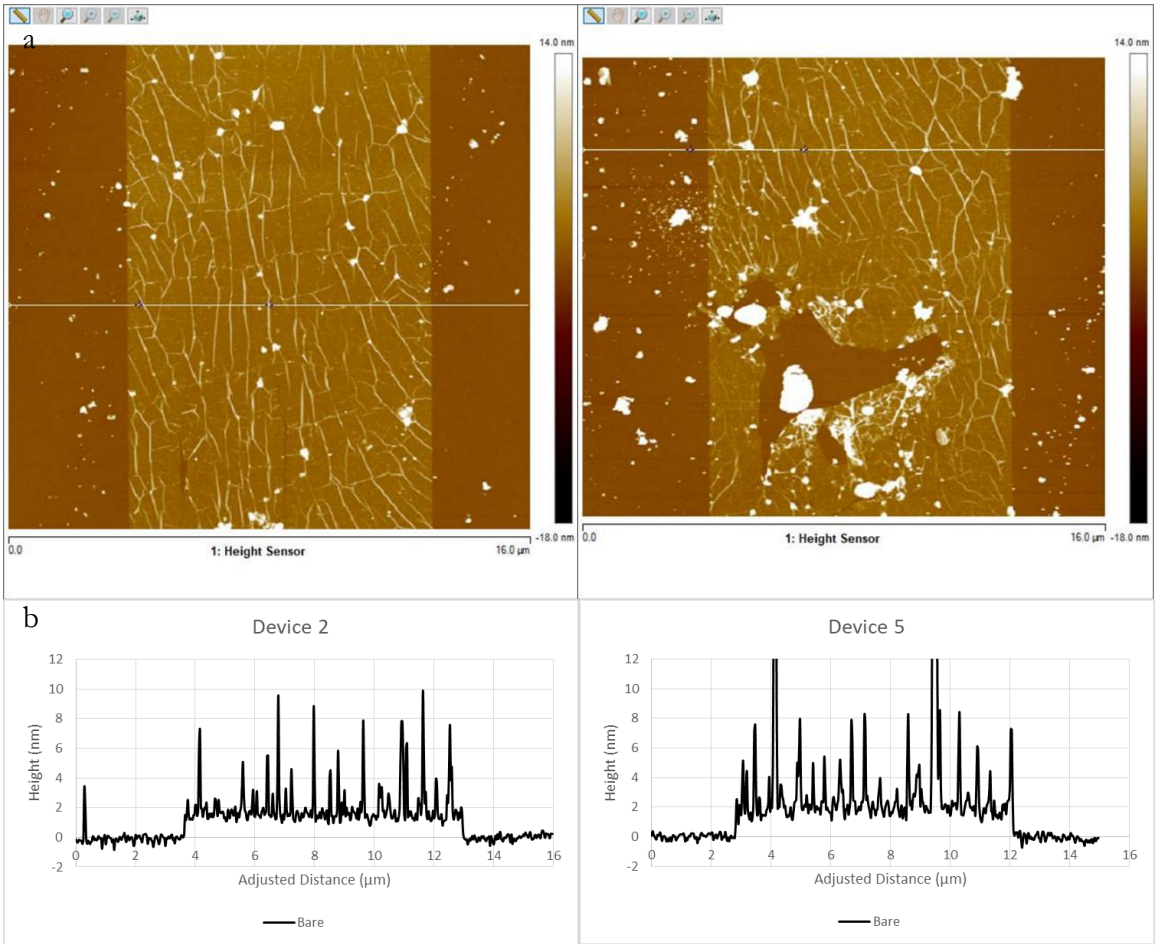

Figure 3.8: (a) An AFM image of Device 2, left, and Device 5, right, after fabrication in June 2018 (b) A line trace of the AFM image. The height of the graphene is 1.75 ± 0.44 nm, and 1.95 ± 0.51 nm, suggesting single layer graphene.

of the wafer during the long process of device fabrication. Debris cannot be typically removed, except by careful plasma etching[4]. Graphene, being a monolayer of graphene, ideally has a thickness of 0.8 nm.[74] However, good samples of graphene have thicknesses less than about 1.3 nm, as 1.6 nm would suggest bilayer graphene.

Before electropolymerization, lithography was performed to expose the graphene and Ti/Pt contacts. Previous devices showed some removal of Ti and Pt during electropolymerization. The Ti/Pt contacts also show warping after electropolymerization. An example of the lithography is shown in Figure 3.9a, with a close-up of one of Device 1 in Figure 3.9b. The green tint is from the PMMA. After fabrication of the devices, I electropolymerized filtered 5 mM phloroglucinol for 50 cycles onto the graphene. As expected, the current is low due the small amount of exposed area. Figure 3.10 shows two cyclic voltammograms of phloroglucinol electropolymerization: one for the June 2018 devices, and one for the September 2018 devices. Figure 3.10a shows a typical electropolymerization cyclic voltammogram. Figure 3.10b is atypical. The cause of the difference is the contact between the Au wire and the phloroglucinol solution. Proper exclusion of the Au wire from the phloroglucinol solution can prevent this. Despite the presence of Au, the phloroglucinol polymer passivates the Ti/Pt contacts and graphene.

[4] Repeated acetone rinses and acetone soaks did not help to remove debris and remaining PMMA. Sonication and heated acetone rinses tend to destroy graphene.

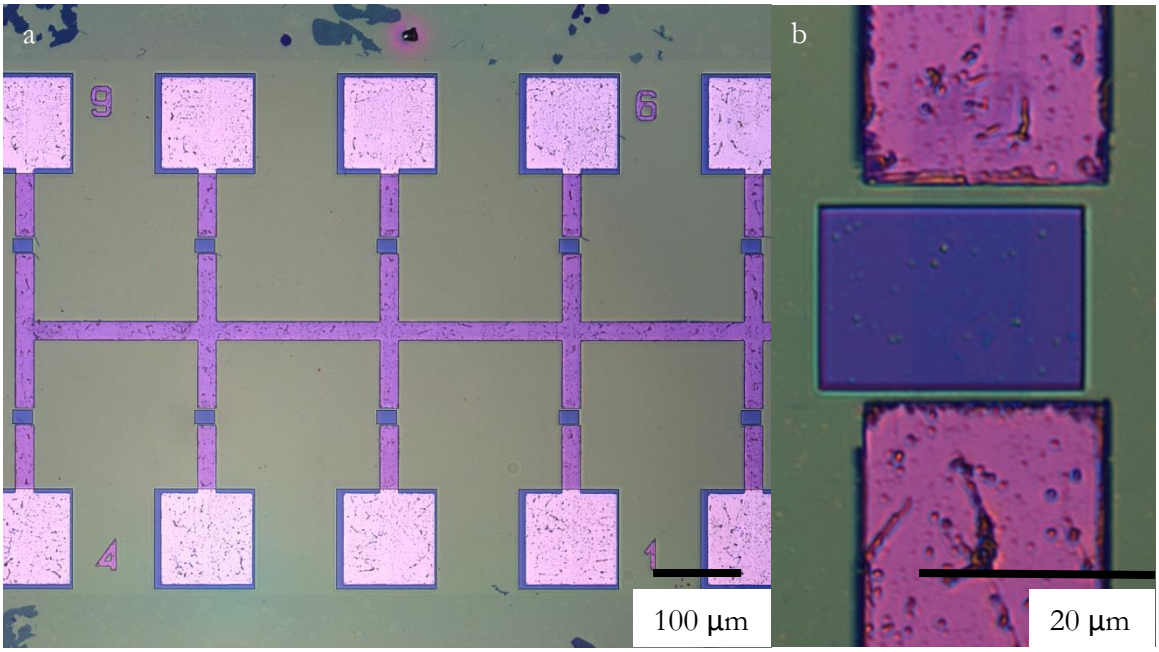

Figure 3.9: (a) 10X optical image of devices created in September 2018 before electropolymerization. Note that only the areas with CVD graphene and Ti/Pt contacts are exposed. The green tint is due to a layer of PMMA The faint blue is CVD graphene. (b) 100X optical image of Device 1. CVD graphene can barely be seen between the Pt fingers.

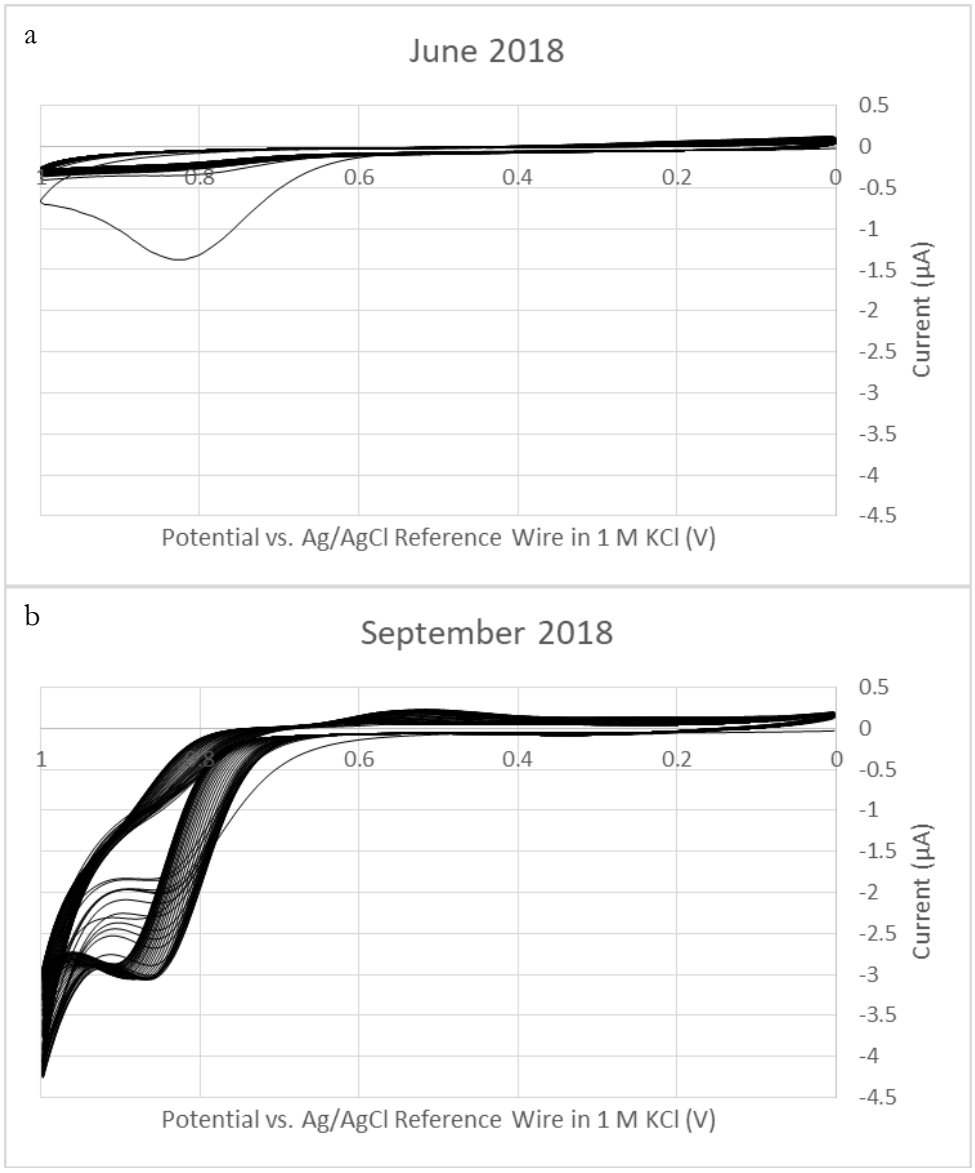

Figure 3.10: Cyclic voltammogram of phloroglucinol electropolymerization on graphene devices fabricated in (a) June 2018 and (b) September 2018. In (b), the high current and the reduction peak around 0.55 V are due to the oxidation of the Au wire, and the reduction of that gold.

Figure 3.11 shows the device set in Figure 3.9 after electropolymerization. I accidentally scratched the wafer with tweezers while picking up the wafer. Because of the phloroglucinol polymer, the location of the graphene is obvious. Note that Figure 3.11a shows the devices before lift off, and Figure 3.11b shows Device 1 after lift off. Figure 3.12a shows AFM of two of the June 2018 devices after electropolymerization. The cracks in the polymer made obtaining reliable heights difficult. However, the average total height is ~70 nm for both devices shown. Subtracting this from the height of the graphene equals the height of the phloroglucinol polymer: ~68 nm. Previous experiments were able to obtain less than 5 nm of polymer using 0.5 mM phloroglucinol and fewer cycles. However, those polymers did not completely passivate the electrode towards $Fe(CN)_6^{4-/3-}$, suggesting pinholes. Nevertheless, the AFM of these devices in Figure 53 show the cracks do not reach the graphene.

Figure 3.13 contains the conductivity data for the June 2018 set of devices that underwent electropolymerization. As can be seen, electropolymerization of phloroglucinol shifted the Dirac point positive. This positive shift in the Dirac point is common for all devices after electropolymerization. This may be due to scattering of the electrons by the polar groups on phloroglucinol. It is known that the conductivity of graphene is highly dependent on the materials above and below graphene.

Figure 3.14 shows in situ ellipsometry modelling data of the deposition of ~2 nm Al_2O_3 onto phloroglucinol polymer on CVD graphene on an oxide stripped Si wafer. The oscillations correspond the deposition cycles of Al_2O_3. The increase in measured thickness is due to the pulse of metal precursor, which in this case is tri(methylamino)aluminum. The decrease in measure thickness is due to the pulse of water, which reacts with the metal precursor and to form metal oxide, in this case, alumina, and free dimethylamine.

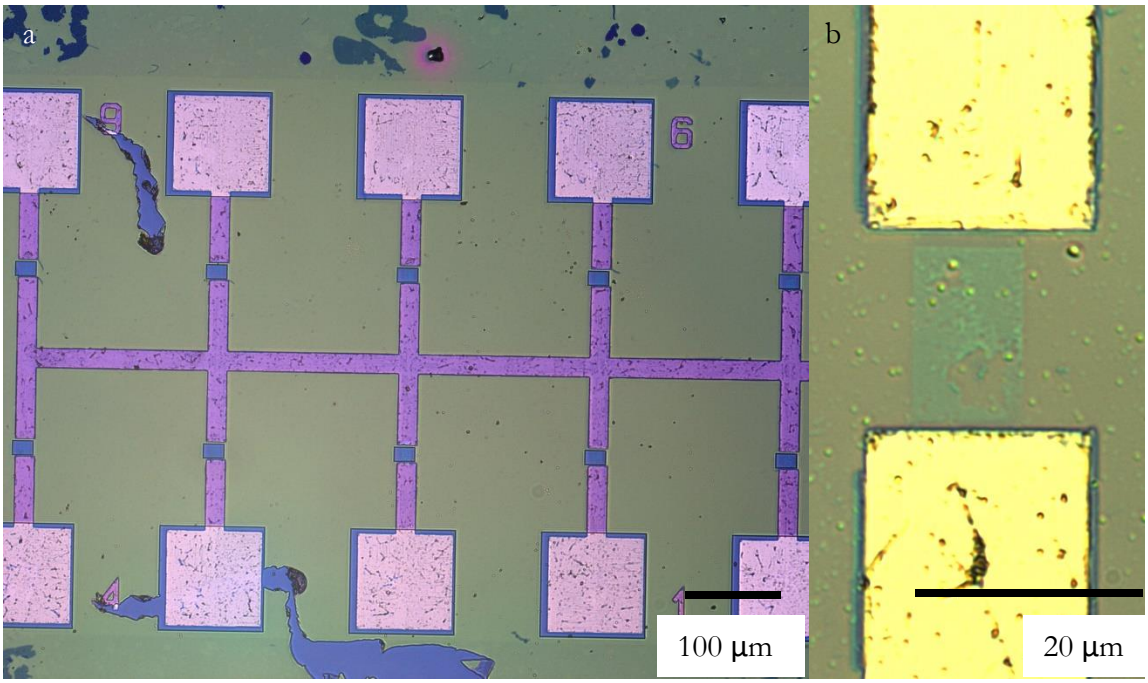

Figure 3.11: (a) 10X optical image of graphene devices crated in September 2018 after electropolymerization. (b) 100X optical image of Device 1 after electropolymerization. Due to the thickness of the polymer, the location of the graphene is more obvious. I accidentally scratched the surface with tweezers while picking up the wafer.

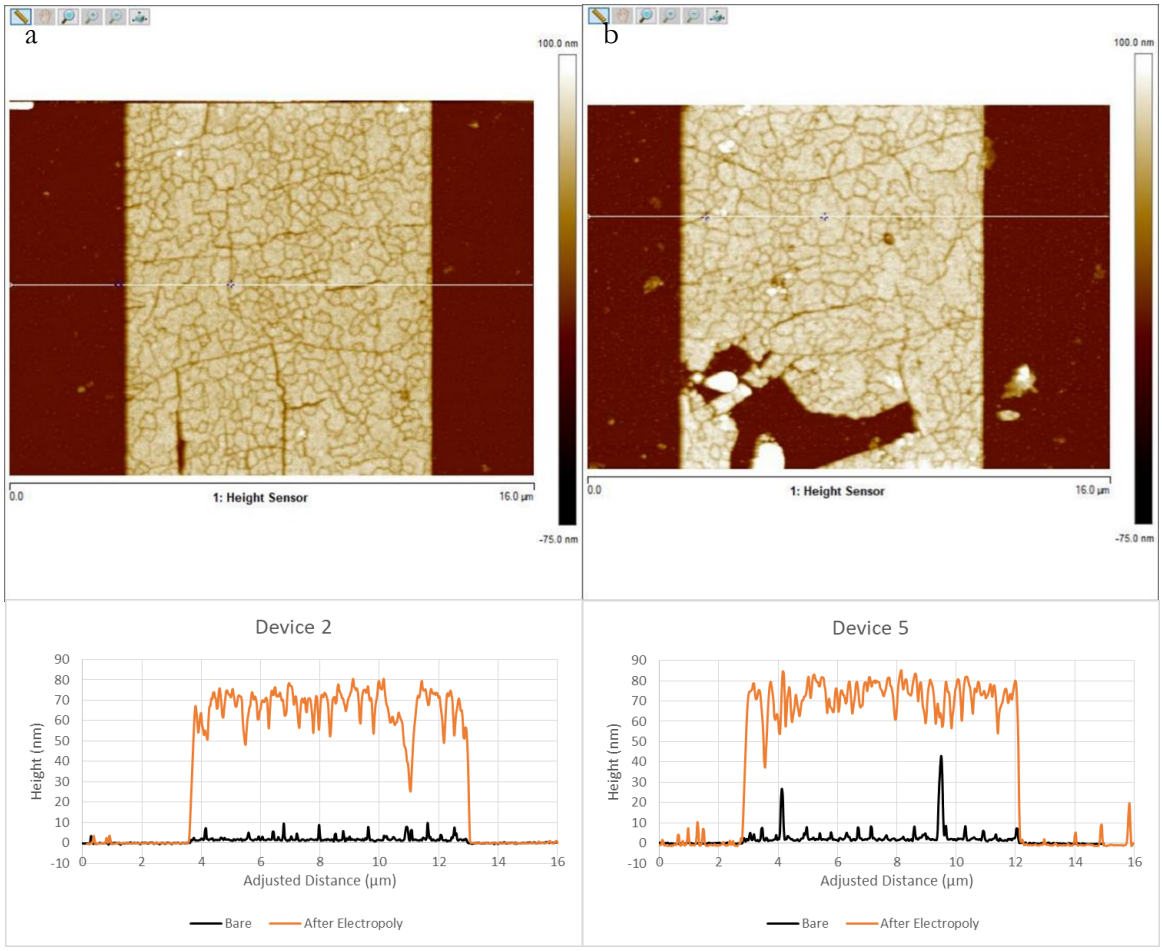

Figure 3.12: (a) AFM images of Devices 2 and 5 after electropolymerization. These devices were fabricated in June 2018 (b) A line trace of the AFM image. The total height is ~70 nm, suggesting ~68 nm of phloroglucinol polymer was deposited.

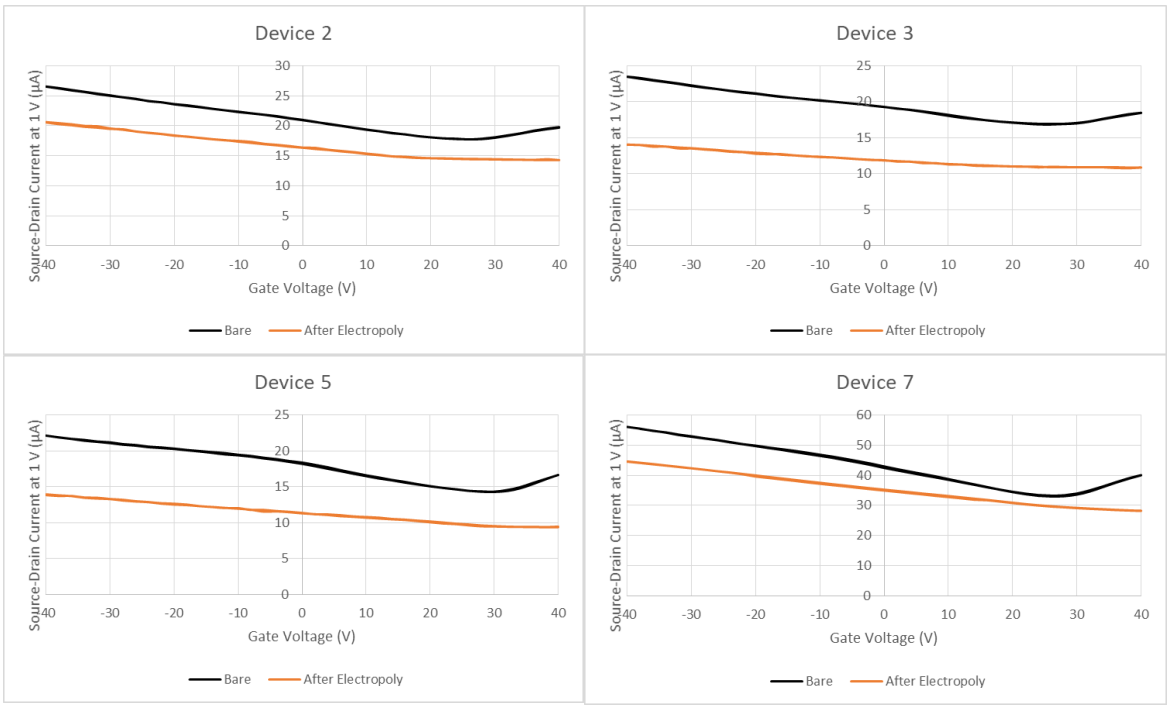

Figure 3.13: Conductivity measurements of Devices 2, 3, 5, and 7 after phloroglucinol electropolymerization. The devices were created in June 2018. Note the differences in current.

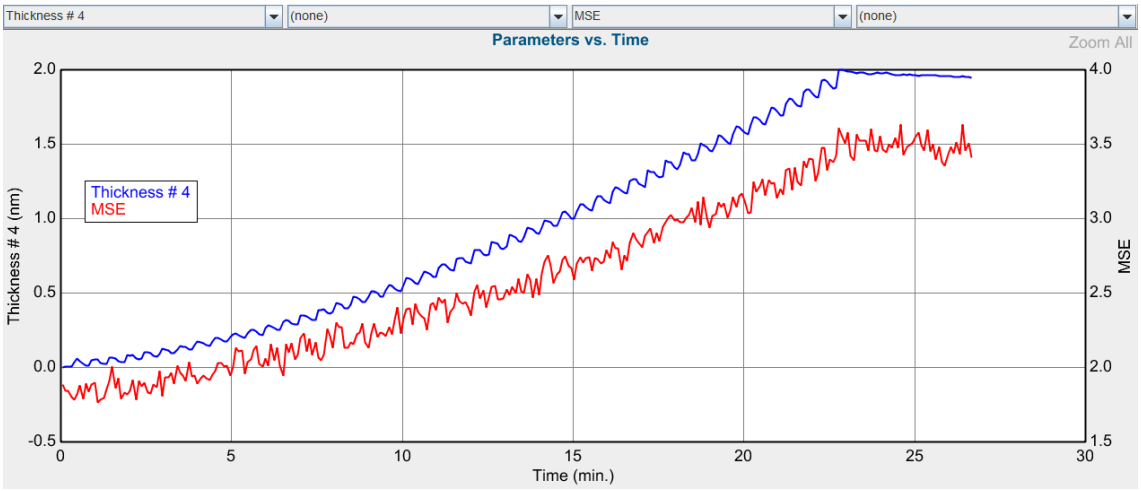

Figure 3.14: *In situ* ellipsometric data showing the growth of Al_2O_3 on a phloroglucinol film that was electropolymerized onto CVD graphene on an oxide stripped Si wafer. The nonlinearlity of the growth is due to approximated parameters for the phloroglucinol film. The oscillations of the cycles correspond to growth of Al_2O_3. MSE represents the mean squared error in nm^2, which measures the error between the model and experimental data.

After showing that ALD on phloroglucinol is possible, I performed ALD on the devices. Figure 3.15a shows an 10X optical image of the September 2018 devices after ALD, and Figure 3.15b shows an 100X optical image of Device 1. Note that the ALD was performed without the PMMA mask used in electropolymerization. Experiments with the June 2018 devices used such a mask: while ALD was possible with the mask, lift off was unsuccessful. Thus, for the September 2018 devices, the PMMA mask was removed before ALD. Figure 3.16a shows an AFM image of the devices after ALD. Because ALD is a conformal process, the Al_2O_3 grows everywhere that is exposed. Thus, the height of the graphene and phloroglucinol polymer appear the same before and after ALD. Ufuk and I chose conditions that should give ~7 nm Al_2O_3.

Conductivity of the devices after ALD is shown in Figure 3.17. Little shifts in the Dirac point is common for all devices. Sometimes, devices with poor or no conductivity spontaneously improved conductivity after ALD. The reason for this is unknown and was not investigated.

Finally, a Ti/Au top gate was deposited on the September 2018 devices. Au rather than Pt was used because previous devices had high leakage currents. It was thought that this was because the Pt was burning through the Al_2O_3 during the evaporation process (Pt evaporation occurs at a higher temperature than Au evaporation). Figure 3.18a shows a 10X optical image of the devices after the top gate deposition, and Figure 3.18b shows a 100X optical image of Device 1. As can be seen, the top gate aligns nicely over the graphene. No AFM image was taken.

Bottom-gate and top-gate conductivity measurements of the September 2018 devices were taken, as shown in Figure 3.19a and 3.19b. As usual, no Dirac points were observed in the

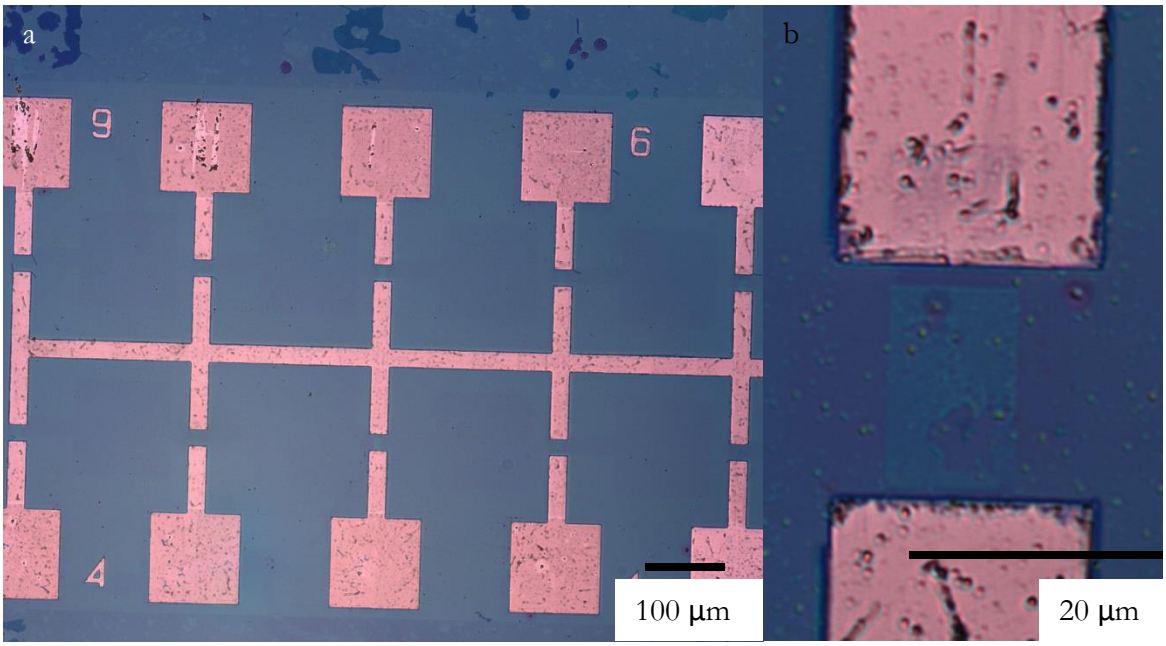

Figure 3.15: (a) 10X optical image of devices created September 2018 after ALD. (b) 100X optical image of Device 1. Notice how the ALD was restricted to only the exposed areas in the PMMA.

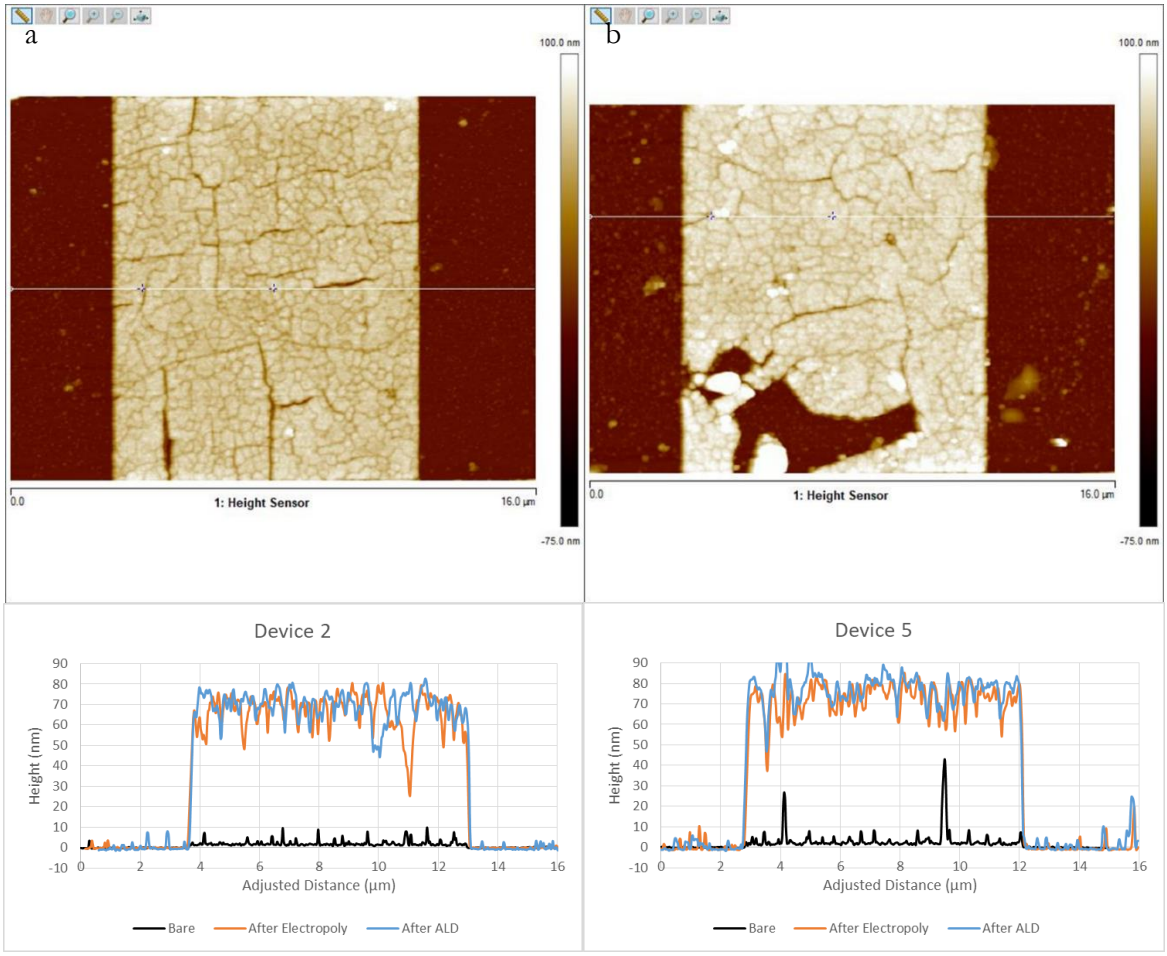

Figure 3.16: (a) An AFM image of Device 2 and 5 after ALD. The devices were fabricated in June 2018. (b) A line trace of the AFM image. Because ALD was performed over the entire area shown, a meaningful height of Al_2O_3 deposited cannot be calculated. The thickness of Al_2O_3 is assumed the same as the test run in Figure 54.

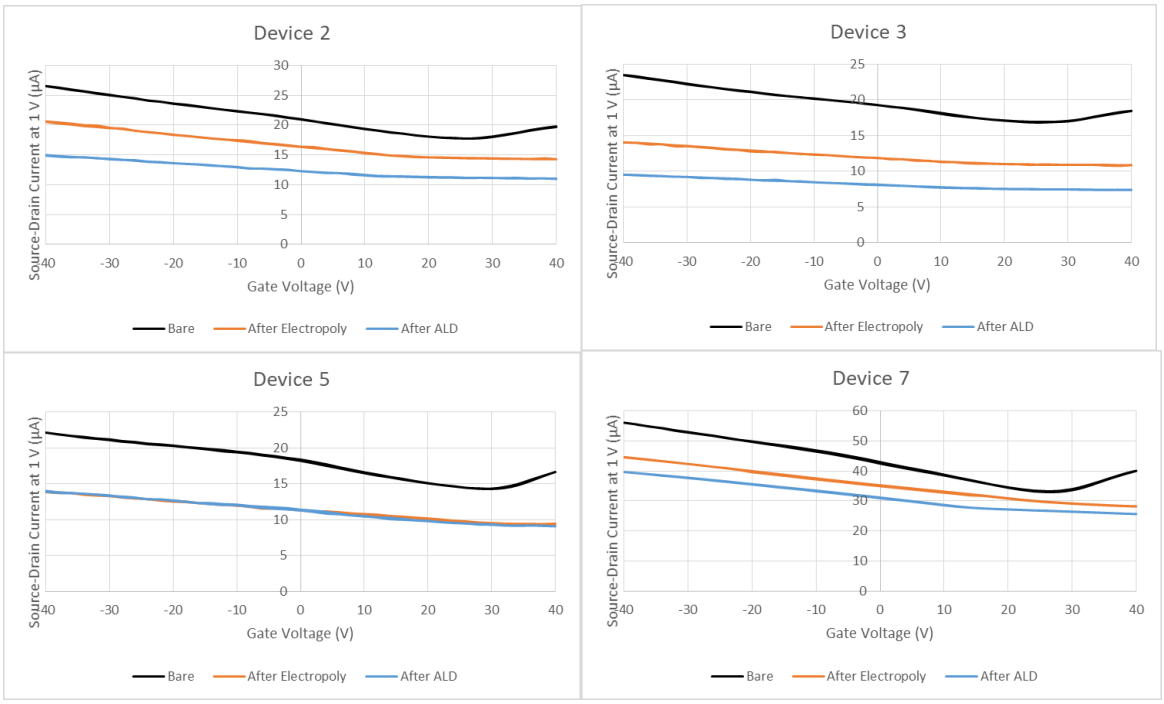

Figure 3.17: Conductivity measurements of Devices 2, 3, 5, and 7 after ALD. These devices were fabricated in June2018. Note the differences in the current scales.

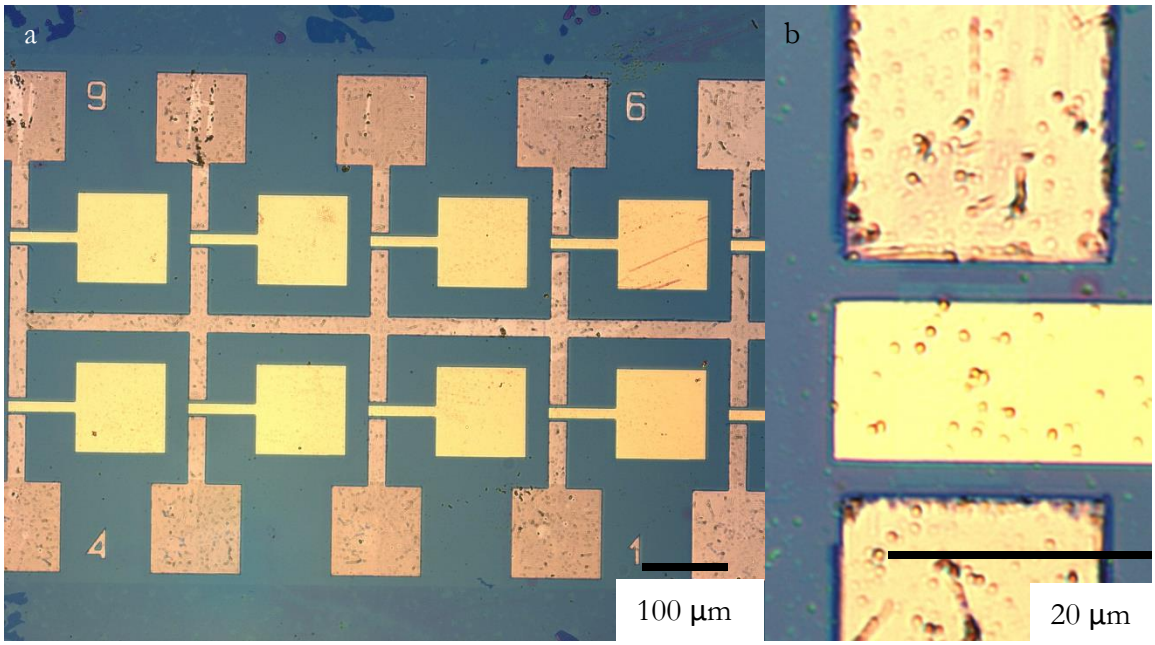

Figure 3.18: (a) 10X optical image of devices after top gate deposition. These devices were fabricated September 2018 (b) 100X optical image of Device 1.

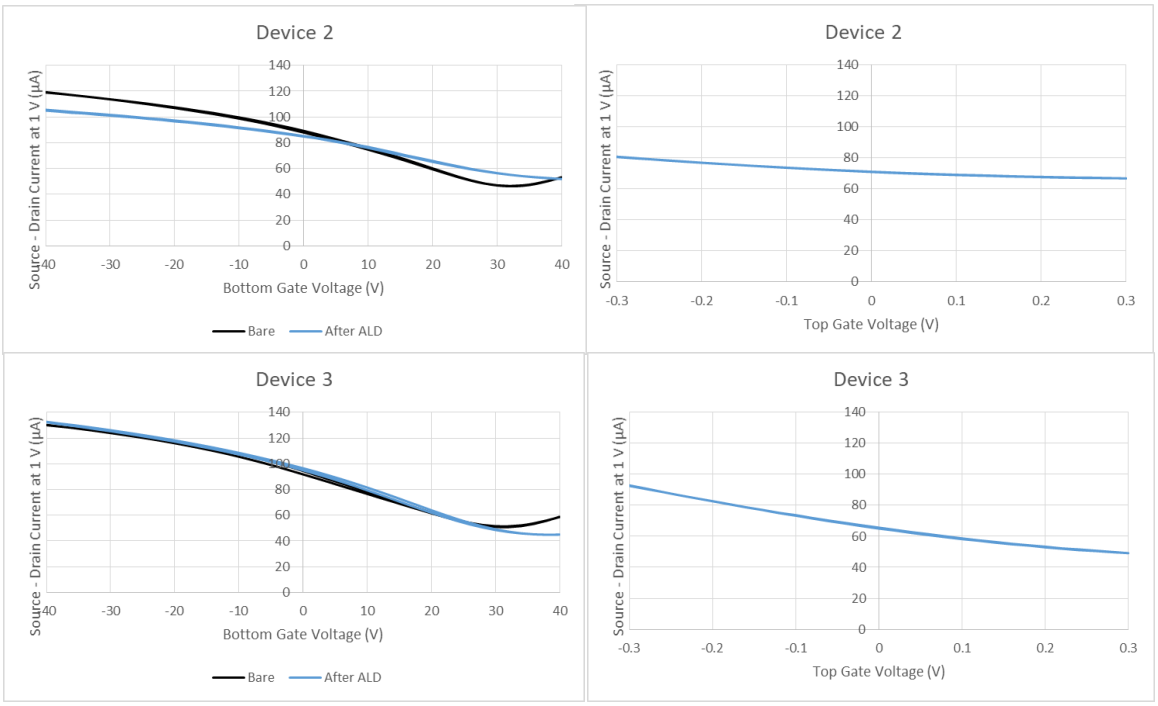

Figure 3.19: (a) Bottom-gate conductivity measurements of Devices 2 and 3. These devices were fabricated in September 2018 (b) Top-gate conductivity measurements of the same devices.

range of bottom gate voltages measured after ALD. This does not necessarily mean a Dirac point does not exist. In addition, no Dirac points were observed in the range of top gate voltages measured. Note that the range voltages for top and bottom gates are different due to the difference in the thickness of the dielectric. The bottom gate electrode has ~300 nm SiO_2 above it, while the top gate electrode has presumably about ~68 nm of phloroglucinol polymer and ~7 nm Al_2O_3 under it.

Unfortunately, all devices fabricated, including these ones, had high leakage currents, or current through the source and gate electrode. Leakage currents should be approximately nano- and picoampere scale. Top-gate leakage currents for all devices were around microampere scale, which is on par with current through source and drain electrodes. Figure 3.20 demonstrates this.

Several attempts to remedy this high leakage were made, such as using PEDOT:PSS instead of Au or Pt, not performing ALD, and electropolymerizing phenol onto the phloroglucinol polymer and using PEDOT:PSS as the top gate electrode. None of these prevented the high leakage currents. Close inspection of the devices show tears within the CVD graphene. It is possible that these tears allowed contact between the top gate and CVD graphene, thus making a short.

Investigation into the Cause of High Leakage Currents

I also started investigating how the temperature from the ALD process impacted the phloroglucinol polymer. Figure 3.21 shows the QCM results. Some of the data from the QCM, except for the bare and coated frequencies, should be interpreted cautiously. The experiment necessitated disassembling the holder after electropolymerization. It is known that disassembly and reassembly of the holder can cause irrecoverable frequency shifts. Nonetheless, the stable frequencies of each are given in Figure 3.22. The frequency shifts

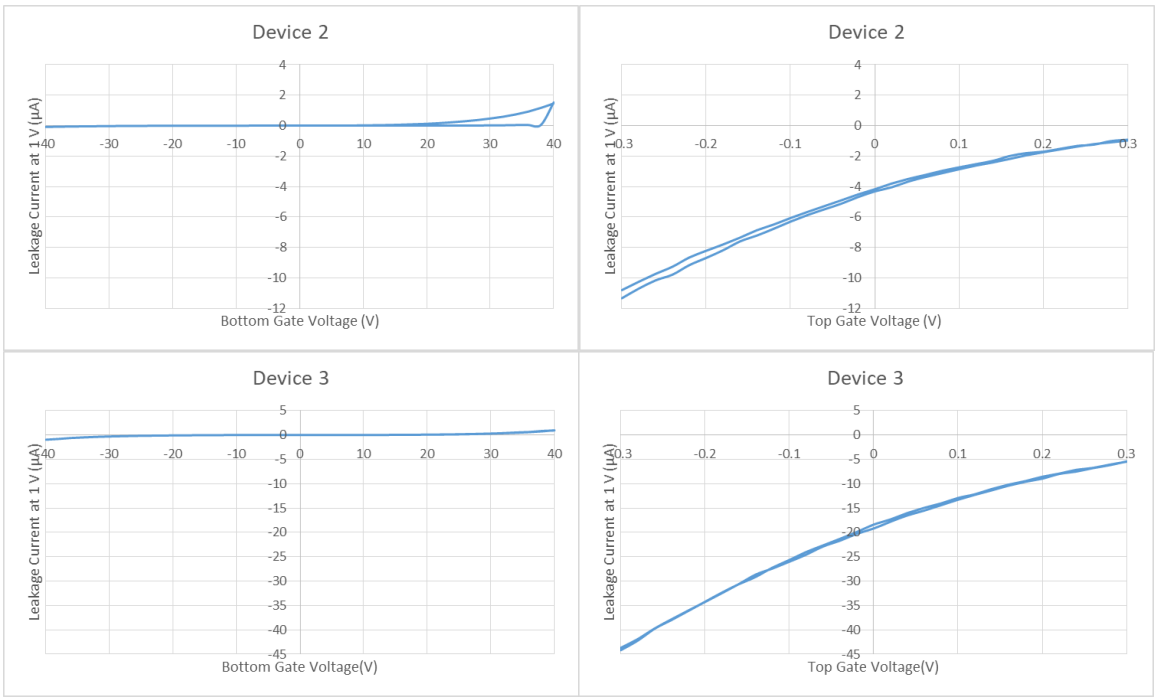

Figure 3.20: These devices were fabricated in September 2018. (a) Bottom gate leakage currents for Devices 2 and 3. Note the general hyperbolic sine character of the leakage current. (b) Top gate leakage current for Devices 2 and 3.

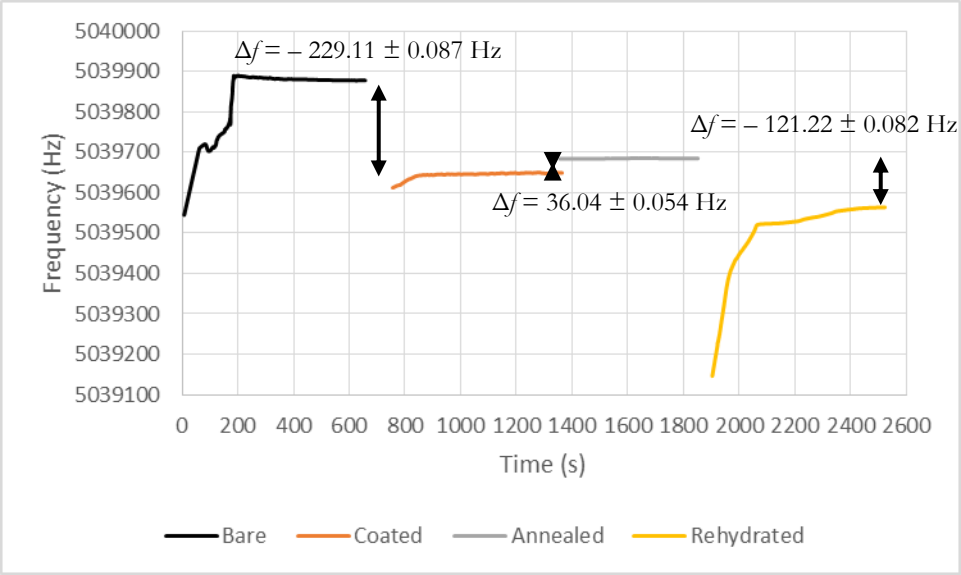

Figure 3.21: QCM results. The time axis is not representative of the actual time a particular experiment was performed, but as a measure of the duration of data collection.

and corresponding mass changes are given in Table 3.1. Mass changes were calculated from the Sauerbrey equation,

$$\Delta f = -C_f \cdot \Delta m$$

where Δf is the observed frequency shift, Δm is the change in mass per unit area, and C_f is the sensitivity factor, taken as 56.6 $\frac{Hz \cdot cm^2}{\mu g}$ for a 5 MHz quartz crystal. The exposed area of the electrode is about 1.37 cm^2, whereas the area that oscillates is about 0.40 cm^2 on a 1-inch diameter by 331 μm thick quartz crystal.[66]

AFM of the QCM before electropolymerization, after electropolymerization, and after annealing did not reveal much information. As can be seen in Figure 3.22, the images appear largely identical. Due to the lack of identifying features on the crystal, different areas with different orientations were scanned. The line scans of those images are in Figure 3.23.

Roughness measurements of a 2.00 by 2.00 μm area void of any large debris are shown in Table 3.2. They show changes in the film, since the roughness decreases after annealing and rehydrtion.

Ellipsometry[74] uses reflected elliptically polarized light to investigate the optical properties of thin materials. The electric field of elliptically polarized light can be deconvoluted into two linearly polarized waves: one in the x-z plane (called p polarized, since it is parallel to the plane of incidence), and the other in the y-z plane (called s polarized, since it is orthogonal to the plane of incidence). Interestingly, neither the absolute intensity of the light nor the absolute phases are important for measurement. Rather the amplitude

Table 3.1: QCM Analysis		
	Frequency Shifts (Hz)	Mass Changes (μg/cm^2)
Bare – Coated	– 229.11 ± 0.087	– 4.047
Annealed – Coated	36.04 ± 0.054	0.637
Rehydrated – Annealed	– 121.22 ± 0.082	– 2.142

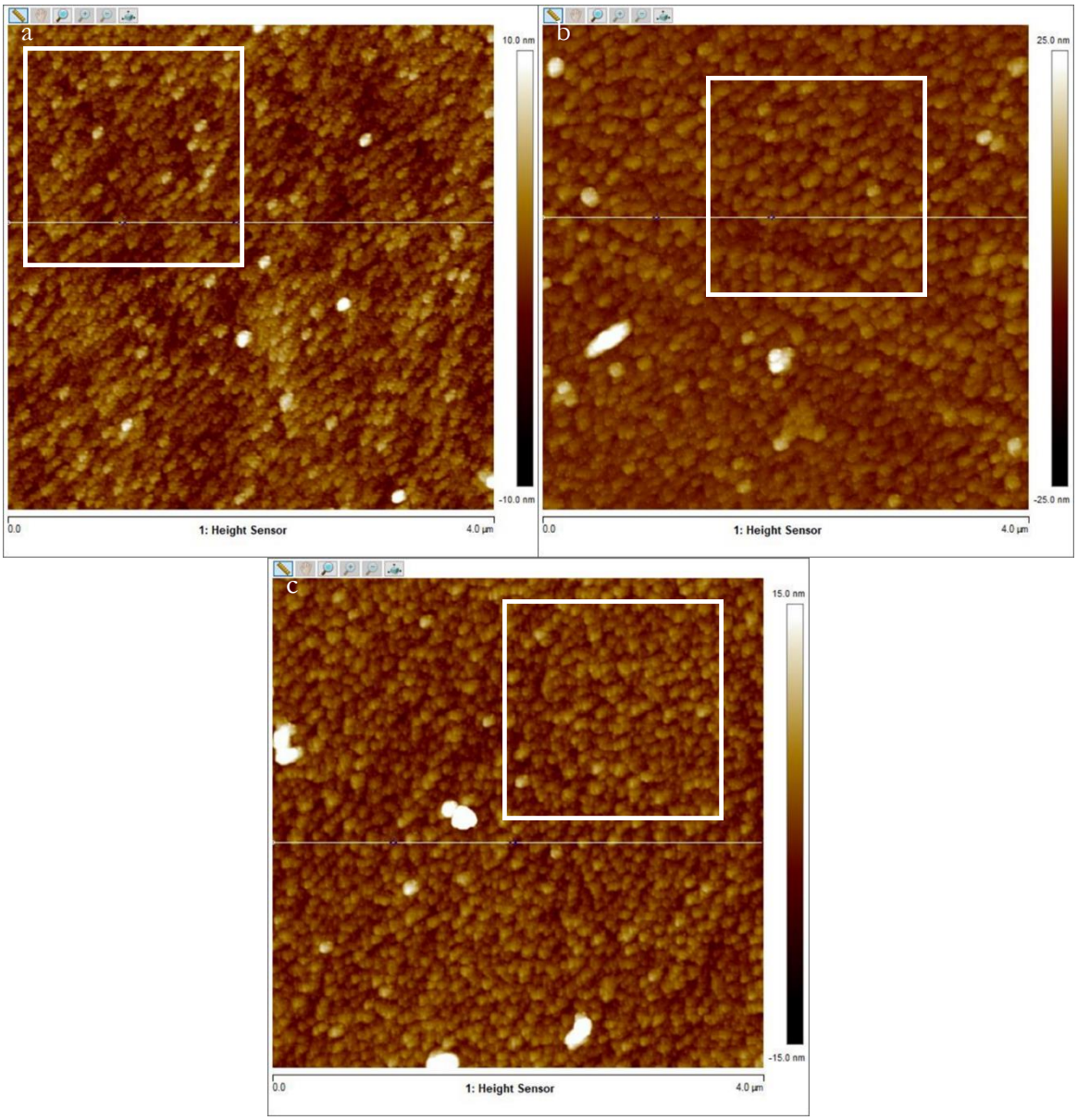

Figure 3.22: AFM images of QCM crystal (a) before electropolymerization, (b) after electropolymerization, and (c) after annealing and rehydration. The white squares represent the approximate areas used for calculating the roughness in Table 10.

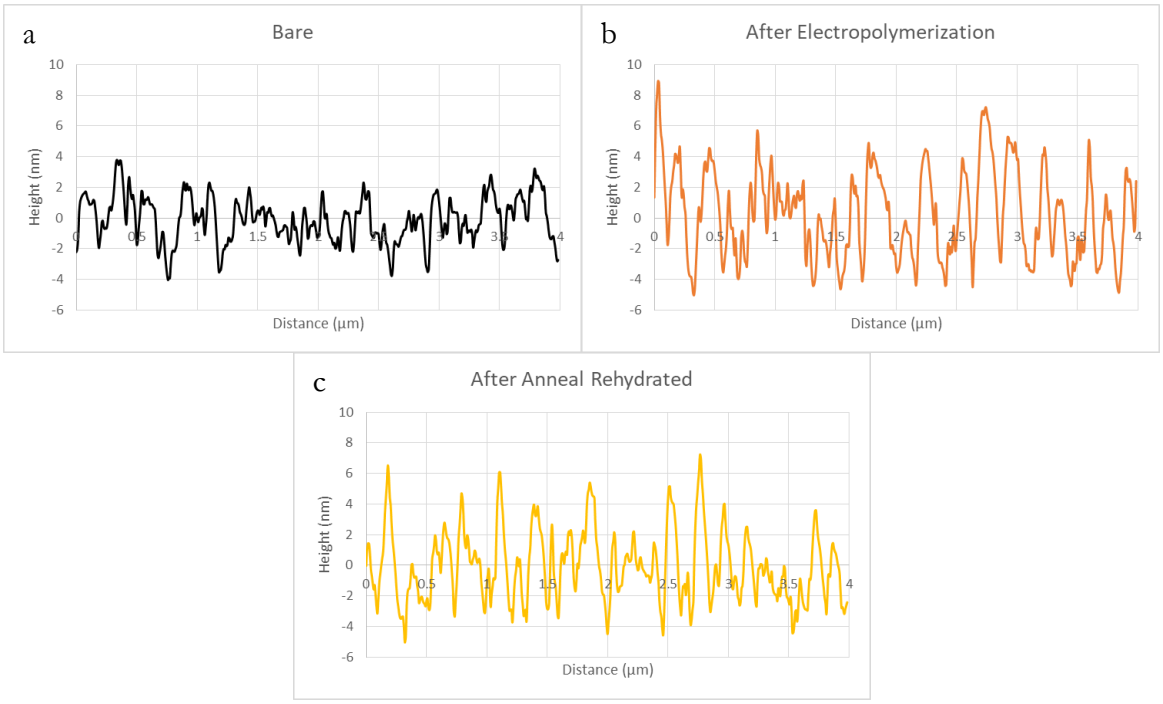

Figure 3.23: AFM traces of QCM crystal (a) before electropolymerization, (b) after electropolymerization, and (c) after annealing and rehydration.

Table 3.2: Roughness Measurements		
	R_a (nm)	R_q (nm)
Bare	1.31	1.65
After Electropolymerization	2.19	2.72
After Annealing and Rehydration	1.74	2.18

ratio, Ψ,

$$\tan \Psi = X / Y$$

, and the phase shift between the two linearly waves, Δ,

$$\Delta = \delta_x - \delta_y$$

of the reflected light carry all the information needed. In the equations, *X* and *Y* refer to the amplitude of the p and s polarized waves, respectively, and δ_x and δ_y refer to the phases of the p and s polarized waves, respectively. Hence Ψ and Δ are often measured in degrees. The ellipsometry performed herein was spectroscopic, meaning Ψ and Δ for several wavelengths were collected. This allowed more Ψ and Δ values to be used for modelling. However, the substrate (Pt electrode on quartz crystal) made the modelling too difficult and erroneous. Without a suitable model, almost no information of importance, including approximate optical constants[76], can be extracted. Thus, only qualitative observations are discussed.

Figure 3.24 and 3.25 shows the Ψ and Δ, respectively, of the QCM crystal at various angles. For all angles, the bare QCM did not have any peaks. After electropolymerization, a peak near 275 nm appeared at 45° and 65°, while a dip appeared at 55° and 65°. After annealing, the peak was reduced, suggesting a regression to the original substrate.

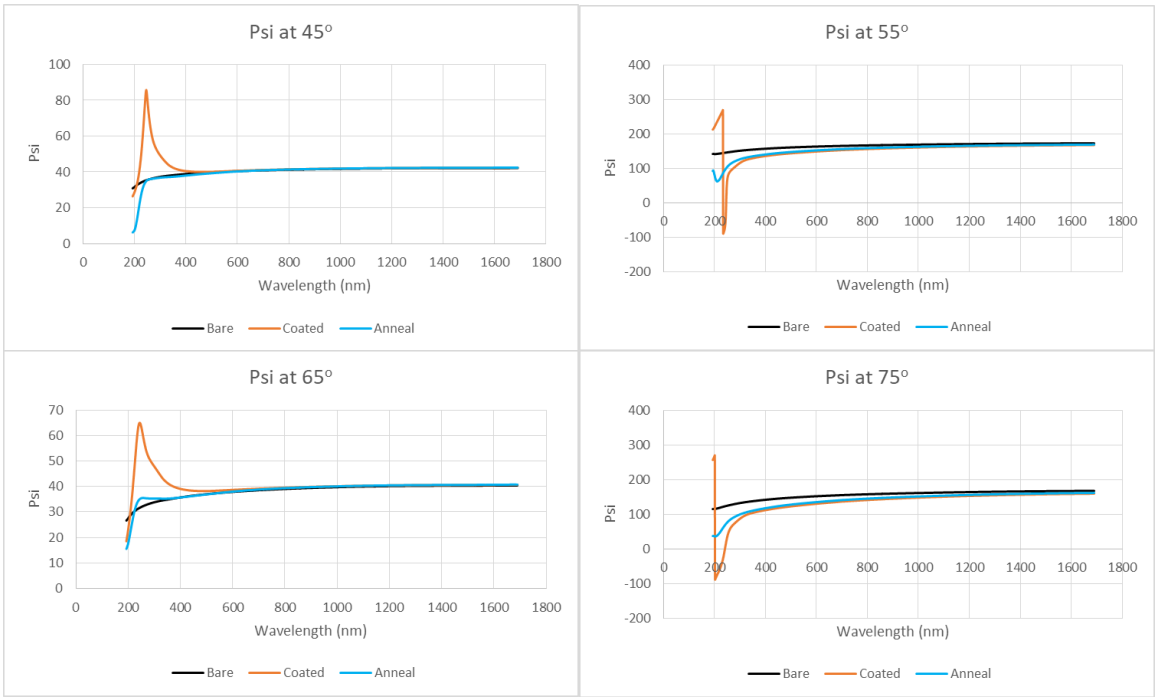

Figure 3.24: Amplitude ratio, Ψ, before electropolymerization, after electropolymerization, and after annealing at various angles of incidence. Note that after annealing, the return to near base measurements.

Similar results were seen with the phase ratio. After annealing, Δ did not return to its bare measurement. This suggests a change in the polymer after annealing. However, it is unknown if this change is due to water removal or decomposition of the polymer.

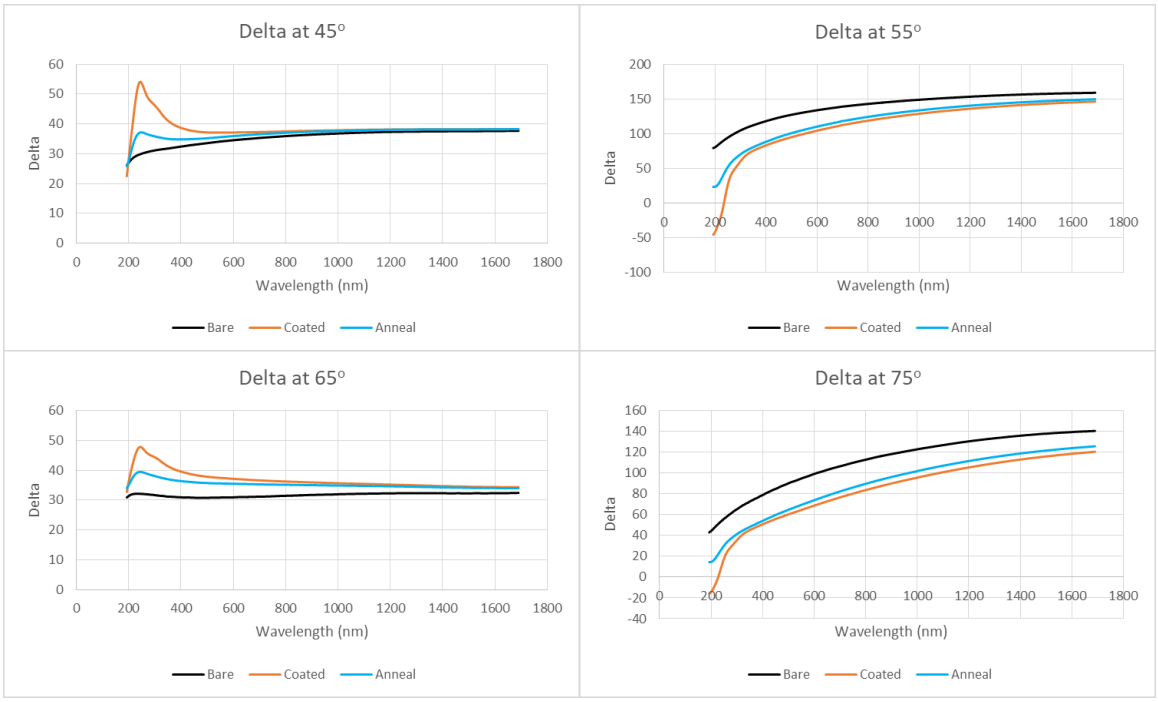

Figure 3.25: Phase ratio, Δ, before electropolymerization, after electropolymerization, and after annealing after various angles of incidence.

Conclusion

Using phloroglucinol as a seed layer for ALD devices was shown, but my research suggested the presence of problematic pinholes within the polymer. The processing and fabrication of the CVD graphene devices will need to be improved, i.e., ensuring the CVD graphene does not have tears. This can be remedied by not etching areas of damaged CVD graphene. Despite the lack of information from ellipsometry and from the roughness data of the AFM, the temperature of the ALD chamber does influence the polymer. I suggest that future experiments include electropolymerizing phloroglucinol onto a simpler substrate, such as bare Si, to allow modelling and extraction of optical constants. This information will help determine the optical thickness of the film. Then, the film can then be observed *in situ* during the heating process and information about how the film changes during annealing can be collected. Another is desiccating the film, which will help determine if the changes in signals from the phloroglucinol polymer are due to water loss.

Table 3.3: Experimental Parameters for Electropolymerization of 0.5 mM Phloroglucinol	
Initial Potential	0.0 V
High Potential	1.0 V
Low Potential	0.0 V
Initial Polarity	Positive
Scan Rate	0.100 V/s
Sweep Segments	10
Sample Interval	0.001
Quiet Time	10 s

Table 3.4: General Conditions of Pattern Generation		
Aperture (μm)	Dose Factor	Step Size (μm)
10 (for Crosses)	1.9	0.008 (length and width)
30 (for Crosses, smaller test devices)	3.9	0.08 (length and width)
60 (for Devices)	3.9	0.1752 (length and width)

Table 3.5: Electron Beam Deposition Parameters			
Element	Minimum Current (mA)	Rate (Å/s)	Voltage (kV)
Titanium (Ti)	45	0.2 – 0.4	7.01
Gold (Au)	70	0.2 – 0.4	7.01
Platinum (Pt)	165	0.2 – 0.4	7.01

Table 3.6: Dimensions of CVD Graphene Devices		
	Length (μm)	Width (μm)
Graphene (total)	30	10
Graphene (total uncovered)	16	10
Graphene (exposed to phloroglucinol solution)	12	10
Device Contacts	100	100
Device Fingers (connected to graphene)	75	20
Top Gate Contacts	100	100
Top Gate Fingers	80	7
Contact to Au Pads	300	300
Contact to Au Pads Finger	20	At least 2000

Table 3.7: Conditions for Al_2O_3 ALD	
Argon Carrier Flow	60 sccm
Argon Plasma Flow	200 sccm
Heater Temperature	150 °C
Automatic Pressure Control Unit	20% (0.18 – 0.20 torr)

Table 3.8: Parameters for Bottom Gate Conductivity Measurements			
Initial Source–Drain Voltage (V_i)	– 1.0 V	Initial Gate Voltage (V_i)	– 40.0 V
Final Source–Drain Voltage (V_f)	1.0 V	Final Gate Voltage (V_f)	40.0 V
Source–Drain Voltage Step ($V_{i,\ step}$)	0.2 V	Gate Voltage Step ($V_{i,\ step}$)	2.0 V

Table 3.9: Parameters for Top Gate Conductivity Measurements			
Initial Source–Drain Voltage (V_i)	– 1.0 V	Initial Gate Voltage (V_i)	– 0.3 V
Final Source–Drain Voltage (V_f)	1.0 V	Final Gate Voltage (V_f)	0.3 V
Source–Drain Voltage Step ($V_{i,\ step}$)	0.2 V	Gate Voltage Step ($V_{i,\ step}$)	0.02 V

Table 3.10: Sputtering Parameters									
Element	Pressure (mbar)	Argon Flow (sccm)	Shape Factor (%)	Power (W)	Set Voltage (V)/ Actual Voltage (V)	Set Current (mA)/ Actual Current (mA)	Rate (Å/s)	Density (g/cm^3)	Acoustic Impedence ($g/cm^2 \cdot s$)
Chromium (Cr)	$1.30 \cdot 10^{-3}$	20	300	16.03	630 / 319	50 / 51	0.25	7.2	$28.95 \cdot 10^5$
Platinum (Pt)				10.85	630 / 368.6	30 / 29	0.28	21.4	$36.04 \cdot 10^5$
Gold (Au)				4.48	630 / 339.2	13 / 13	0.28	19.3	$23.18 \cdot 10^5$

References

[1] Geim, A. K. *Science* **2009** *324* 1530
[2] Allen, M., Tung, V., and Kaner, R. *Chem. Rev.* **2010** *110* 132
[3] Cooper, D., D'Anjou, B., Ghattamaneni, N., Harack, B., Hilke, M., Horth, A., Majlis, N., Massicotte, M., Vandsburger, L., Whiteway, E., and Yu, V. *ISRN Condensed Matter Physics* **2012** *2012* 501686
[4] Tan, C., Cao, X., Wu, X.-J., He, Q., Yang, J., Zhang, X., Chen, J., Zhao, W., Han, S., Nam, G.-H., Sindoro, M., and Zhang, H. *Chem. Rev.* **2017** *117* 6225
[5] Akinwande, D., Brennan, C., Bunch, J., Egberts, P., Felts, J., Gao, H., Huang, R., Kim, J.-S., Li, T., Li, Y., Liechti, K., Lu, N., Park, H., Reed, E., Wang, P., Yakobson, B., Zhang, T., Zhang, Y.-W., Zhou, Y., and Zhu, Y. *Extreme Mechanics Letters* **2017** *13* 42
[6] Landau, L. D. *Phys. Z. Sowjetunion* **1937** *11* 26
[7] Peierls, R. E. *Ann. Inst. Henri Poincare* **1935** *5* 177
[8] Wallace, P. *Phys. Rev.* **1947** *71* 622
[9] Novoselov, K. S.; Geim, A. K.; Morozov, S. V.; Jiang, D.; Katsnelson, M. I.; Grigorieva, I. V.; Dubonos, S. V.; Firsov, A. A. *Nature* **2005** *438* 197
[10] Novoselov, K. S.; Geim, A. K.; Morozov, S. V.; Jiang, D.; Zhang, Y.; Dubonos, S. V.; Grigorieva, I. V.; Firsov, A. A., *Science* **2004** *306* 666
[11] Johanson, L. Radiation hard silicon microstrip detectors for use in ATLAS at CERN. Ph. D. Thesis, University of Bergen, Norway, 2005
[12] Schwierz, F. *Nature Nanotechnology* **2010** *5* 487
[13] Choi, W., Lahiri, I., Seelaboyina, R., and Kang, Y. *Critical Reviews in Solid State and Materials Sciences* **2010** *35* 52
[14] Zhang, Y., Zhang, L., Zhou, C. *Accounts of Chemical Research* **2013** *46* 2329
[15] Shams, S., Zhang, R., and Zhu, J. *Materials Science – Poland* **2015** *33* 566
[16] Munoz, R. and Gomez-Aleixandre, C. *Chem. Vap. Deposition* **2013** *19* 297
[17] Batzill, M. *Surface Science Reports* **2012** *67* 83
[18] Whitener, Jr., K. and Sheehan, P. *Diamond & Related Materials* **2014** *46* 25
[19] MOSFET Device Physics and Operation. In *Device Modeling for Analog and RF CMOS Circuit Design*; Ytterdal, T., Cheng, Y., and Fjeldly, T. A., Eds; John Wiley: San Fransisco; 2003; pp 1 – 47.
[20] Mattevi, C., Kim, H., and Chhowalla, M. *J. Mater. Chem.* **2011** *21* 3324
[21] Sun, D. – M., Liu, C., Ren, W. – C., Cheng, H. – M. *Small* **2013** *8* 1188
[22] Layek, R. and Nandi, A. *Polymer* **2013** *54* 5087
[23] Wang, X., Tabakman, S., and Dai, H. *J. Am. Chem. Soc.* **2008** *130* 8152
[24] Lee, B., Mordi, G., Kim, M., Chabal, Y., Vogel, E., Wallace, R., Cho, K., Colombo, L., and Kim, J. *Appl. Phys. Lett.* **2010** *97* 043107
[25] Cavanagh, A., Wilson, C., Weimer, A., and George, S. *Nanotechnology* **2009** *20* 255602
[26] Farmer, D. and Gordon, R. *Nano Lett.* **2006** *6* 699
[27] Finklea, H., Snider, D., and Fedyk, J. *Langmuir* **1990** *6* 371
[28] Bartlett, P. and Cooper, J. *J. Electroanal. Chem.* **1993** *362* 1
[29] Miao, Y., Chen, J., and Wu, X. *Trends in Biotechnology* **2004** *22* 227
[30] Ortega, J., Menolasina, S., Perez de Marquez, O., and Marquez, J. *Polymer* **1986** *27* 1304.
[31] Letheby, H. *J. Chem. Soc.* **1862** *15* 161
[32] Mohilner, D., Adams, R., and Argersinger, Jr., W. *J. Am. Chem. Soc.* **1962** *84* 3618
[33] Lipatov, A., Wymore, B. B., Fursina, A., Vo, T. H., Sinitskii, A., Redepenning, J. G. *Chem. Mater.* **2015** *27* 157

[34] Deheryan, S., Cott, D. J., Muller, R., Timmermans, M., Heyns, M., Vereecken, P. M. *Carbon* **2015** *88* 42.

[35] Sawyer, D. T. and Roberts, J. L. *Experimental Electrochemistry for Chemists* 1st ed. (1974) John Wiley & Sons.
[36] Duan, X., Tian, L., Liu, W., and Chang, L. *Electrochimica Acta.* **2013** *94* 192.
[37] Wang, X.-M., Hu, J.-M., Zhang, J.-Q, Cao, C.-N. *Electrochimica Acta* **2008** *53* 3386
[38] Ezerskis, Z., and Jusys, Z. *J. Appl. Electrochem.* **2002** *32* 755
[39] Rodgers, J., Jedral, W., and Bunce, N. *Environ. Sci. Technol.* **1999** *33* 1453
[40] Babai, M., Gottesfeld, S., and Gileadi, E. *Israel Journal of Chemistry* **1979** *18* 110
[41] Karabinas, P. *Can. J. Chem.* **1990** *68* 302
[42] Pham, M. C., Moslih, J., and Laczae, P.-C. *J. Electrochem. Soc.* **1991** *138* 449
[43] Richard, K., and Gewirth, A. *J. Electrochem. Soc.* **1996** *143* 2088
[44] Ciriello, R., Guerrieri, A., Pavese, F., and Salvi, A. M. *Anal Bioanal Chem.* **2008** *392* 913
[45] Pan, H., Liu, W., Li, X., Ren, Y., and Liu, S. *Adv. Mater. Res.* **2012** *503 – 504* 334
[46] Bejerano, T., Forgacs, C. H., and Gileadi, E. *J. Electroanal Chem.* **1970** *27* 69
[47] Lucho, A., Hallal, J., and Goncalves, R. *Journal of Macromolecular Science, Part A.* **2003** *40* 933
[48] Lucho, A., and Goncalves, R. *Journal of Macromolecular Science, Part A.* **2005** *42* 791
[49] Mu, S. and Chen, C. *J. Phys. Chem. B.* **2012** *116* 12567
[50] Bartlett, P., Tebbutt, P., and Tyrrell, C. *Anal. Chem.* **1992** *64* 138
[51] Correa, C., Santhiago, M., Castro e Silva, C., Formiga, A., and Kubota, L. *Electroanalysis* **2011** *23* 2562
[52] Hammann, M., Castillo, D., Anger, C., and Rieger, B. *J. Mater. Chem. A* **2014** *2* 16389
[53] Subramanian, R. and Garg, B. *Polymer Bulletin* **1979** *1* 421
[54] Tanaka, S. and Iso, T. *J. Chem. Soc. Chem. Commun.* **1994** 1071
[55] Scheller, F. and Heiduschka, P. *Biosensors and Bioelectronics* **1994** *9* 7
[56] Nakabayashi, Y., Wakuda, M., and Imia, H. *Anal. Sci.* **1998** *14* 1069
[57] Samet, Y., Kraiem, D., and Abdelhedi, R. *Progress in Organic Coatings* **2010** *69* 335
[58] Barham, A. *Int. J. Electrochem. Sci.* **2018** *13* 3660
[59] Taj, S., Ahmed, M., and Sankarapapavinasam, S. *Synthetic Materials* **1992** *52* 147
[60] Franco, D., Afonso, A., Vieira, S., Ferreira, L., Goncalves, R., Brito – Madurro, A., and Madurro, J. *Mat. Chem. Phys.* **2008** *107* 404
[61] Fung, Y.-S., Si, S.-H., and Zhu, D.-R. *Talanta* **2000** *51* 151
[62] Park, J. and Eun, C. *Electrochimica Acta* **2016** *194* 346
[63] Li, J., Kuang, D., Feng, Y., Liu, M., Zhang, F., and Deng, P. *J. Braz. Chem. Soc.* **2013** *24* 621
[64] Banait, J. and Pahil, P. *Polyhedron* **1986** *5* 1865
[65] Pekec, B., Misini, M., Sys, M., Samphao, A., Vytras, K., Ortner, A., Feketefoldi, B., Ribitsch, V., Arbneshi, T., and Kalcher, K. *Sensing in Electroanalysis* **2012** *7* 335
[66] Stanford Research Systems, Inc. QCM200 Manual. **2004**

[67] Leskelä, M., and Ritala, M. *Thin Solid Films.* **2002**, *409*, 138.
[68] Puurunen, R. L. *Journal of Applied Physics.* **2005**, *97*, 121301.
[69] George, S. M. *Chemical Reviews.* **2010**, *110*, 111.
[70] Lipatov, A., Varezhnikov, A., Augustin, M., Bruns, M., Sommer, M., Sysoev, V., Kolmakov, A., Sinitskii, A. *Appl. Phys. Lett.* **2014** *104* 013114.
[71] White, R. Spin-Coating Processing of PEDOT:PSS. (2015) http://engineering.tufts.edu/microfab/documents/SOP_spinCoatingPEDOTpss.pdf

[72] Khodagholy, D., Gurfinkel, M., Stavrinidou, E., Leleux, P., Herve, T., Sanaur, S., and Malliaras, G. *Appl. Phys. Lett.* **2011** *99* 163304
[73] Malard, L., Pimenta, M., Dresselhaus, G., and Dresselhaus, M. *Physics Reports* 473 (2009) 51
[74] Humlicek, J. Polarized Light and Ellipsometry. In *Handbook of Ellipsometry*; Tompkins, H. G. and Irene, E. A., Ed; William Andrew: Norwich; 2005; pp 3 – 91.
[75] Hilfiker, J. N.; Singh, N.; Tiwald, T.; Convey, D.; Smith, S. M.; Baker, J. H.; and Tompkins, H. G. *Thin Solid Films*. **2008**, *516*, 7979.

APPENDIX: TIPS, HINTS, AND GUIDES ON USING VARIOUS INSTRUMENTS IN THE NCMN (NEBRASKA CENTER FOR MATERIALS AND NANOSCIENCE)

Section I: Atomic Force Microscopy (Dimension 3100 and BrukerIcon)

1. A good image is the product of good sample preparation, good AFM technique, and good image processing. However, even the best technique and image processing cannot save a poorly prepared sample.
2. Ensure the slow scan axis is perpendicular to the feature you want to measure.
3. To gain optimal images, shift the tip resonance frequency to slightly lower frequencies. When determining the resonance, the instrument actually determines the free resonance frequency. By shifting to slightly lower frequencies, one avoids the instrument not detecting the opposite edge of a feature.
4. Artifacts:
    a. Repetitive triangles in the image indicate a broken tip
    b. Duplicate or subdued features indicate something is attached to the tip.
    c. Streaking is due to scanning too fast over features with drastic height differences.
    d. Other artifacts such as bow and uneven surfaces (common after AFM measurements) can be mathematically removed with software. It is useful to use different flattening (removes bow and S curves) and plane fitting (removes uneven surfaces) parameters with each image. Eventually, you will find a set of parameters that works for most images. Never use zero as a parameter for each. Note that flattening may be necessary in all cases.
5. Try using different software other than the one provided (NanoScope Analysis). Often, other programs such as Gwyddion or Imagemet, will automate tedious tasks, or offer functions not included in others. Please, however, use one software program, as the algorithms for flattening, plane fitting, and others are likely different between programs.
6. Thresholding for both flattening and plane fitting is a powerful convenience. In thresholding, the computer calculates the areas not to be included in the flattening and plane fitting calculations. This is useful for unfortunately dirty samples ☹. Moreover, this technique works best on flat samples; thus, a plane fit may be necessary before thresholding. Furthermore, a manual plane flit or flattening may be necessary for particularly dirty or warped samples.

Section II: Electron Beam Lithography (Zeiss Supra 40 Field-Emission Scanning Electron Microscope and a Raith Pattern Generator)

1. I found that burn dots are most visible away from the edges. The dots appear readily after about two (2) minutes with PMMA-A4. A good dot appears as a perfectly circular donut.
2. Expanding the write field alignment window may be useful in locating burn dots.
3. Burn dots located near "large" (> 2 μm) structures or debris are easier to locate than burn dots in an empty area.
4. I found that the distance between the fiduciary marks affects the accuracy of the placement of patterns. Specifically, patterns outside the fiduciary marks tend to have more error in their placement than patterns within the fiduciary marks.

5. Use layers to build complex structures. Ensure that all patterns in a layer have the appropriate dose factor.
6. Zoom errors during write field alignment can be fixed by adjusting the zoom.

Section III: Electron Beam Evaporation (AJA E-beam Evaporator)

1. This particular instrument used has a thickness monitor that reads in kÅ. Recall that 1 nm is 10 Å, which is 0.01 kÅ.
2. When using new metals, slowly melt the metal. This will prevent splattering and avalanching (a sudden increase in deposition rate).
3. The angle of viewing window makes the alignment of the prongs and the notches on the back of the platform difficult. I suggest allowing the prongs to lightly graze the back of the platform until a "click" is seen. The click indicates the prongs are in the openings of the back of the platform. Aligning the back of the platform such that one notch is in line with the transfer arm can help with this.

Section IV: Energy Dispersive Spectroscopy (Zeiss EVO MA10 with IXRF Systems, Inc. 550i Processsor)

1. Use a beam energy suitable for the elements suspected in the sample. The beam energy should be at least 5 kV higher than the largest characteristic X-ray.
2. Low beam energies help to elucidate lighter elements. High beam energies help to identify heavier elements.
3. Be aware that high beam energies can distort or destroy samples.
4. For unknown reasons, the first image obtained within the … software is distorted. Simply stop and retake the image.
5. Be aware of sum peaks. These occur at 3.48 eV (kV), 2.265 eV (kV), and 1.05 eV (kV) for measurements taken on SiO_2 wafers. They correspond to Si-Si, Si-O, and O-O, respectively.
6. Be consistent in the area exposed.
7. Best results are obtain from working distances around 10 mm. Be consistent with the working distance used.
8. The AutoPeakID feature is useful, but use multiple peaks to verify the presence or absence of an element.
9. The spectrum data is exported as an EMSA file, which can be opened in a spreadsheet program. The information in the file is in Notebook 1 page 95.

Section V: Index of Important Information in Notebooks